ELECTRONIC STRUCTURE STUDIES OF SOME TOPOLOGICAL INSULATORS AND NEW SUPERCONDUCTORS USING PHOTOELECTRON SPECTROSCOPY AND FIRST PRINCIPLES CALCULATIONS

By

Himanshu Lohani

PHYS07201004006

Institute of Physics, Bhubaneswar

A thesis submitted to the
Board of Studies in Physical Sciences

In partial fulfillment of requirements
For the Degree of

DOCTOR OF PHILOSOPHY
of
HOMI BHABHA NATIONAL INSTITUTE

April, 2017

STATEMENT BY AUTHOR

This dissertation has been submitted in partial fulfillment of requirements for an advanced degree at Homi Bhabha National Institute (HBNI) and is deposited in the Library to be made available to borrowers under rules of the HBNI.

Brief quotations from this dissertation are allowable without special permission, provided that accurate acknowledgment of source is made. Requests for permission for extended quotation from or reproduction of this manuscript in whole or in part may be granted by the Competent Authority of HBNI when in his or her judgment the proposed use of the material is in the interests of scholarship. In all other instances, however, permission must be obtained from the author.

Himanshu Lohani

DECLARATION

I, hereby declare that the investigation presented in the thesis has been carried out by me. The work is original and has not been submitted earlier as a whole or in part for a degree/diploma at this or any other Institution/University.

Himanshu Lohani

List of Publications arising from the thesis

Journal

1. Investigation of Correlation Effects in FeSe and FeTe by LDA + U Method, **H. Lohani**, P. Mishra and B. R. Sekhar, *Physica C*, **(2015)**, *512*, 54-60.

2. Valence Band Electronic Structure of Pd Based Ternary Chalcogenide Superconductors, **H. Lohani**, P. Mishra R. Goyal, V. P. S. Awana, and B. R. Sekhar, *Physica C*, **(2016)**, *531*, 98-102.

3. Valence Band Electronic Structure of $Nb2Pd_{1.2}Se_5$ and $Nb2Pd_{0.95}S_5$ Superconductors, **H. Lohani**, P. Mishra, R. Goyal, V. P. S. Awana, and B. R. Sekhar, *Physica B*, **(2017)**, *509*, 31-35.

4. Fermi Surface and Band Structure of BiPd from ARPES Studies, **H. Lohani**, P. Mishra, Anurag Gupta, V. P. S. Awana, and B. R. Sekhar, *Physica C*, **(2017)**, *534*, 13-18.

5. Band Structure of Topological Insulator $BiSbTe_{1.25}Se_{1.75}$, **H. Lohani**, P. Mishra, A. Banerjee, M. Unnikrishnan, D. Topwal, P. S. Anil Kumar, and B. R. Sekhar, *Scientific Reports*, **Under review**.

6. A comparative ARPES study on Bi_2Se_3 and BiSe topological insulators, **H. Lohani**, P. Mishra, K. Majhi, A. Banerjee, A. K. Yadav, R. Ganesan, P. S. Anil Kumar and B. R. Sekhar, **Manuscript under preparation**.

Conferences

1. ARPES study on Bi_2Se_3 and $BiSbTe_{1.25}Se_{1.75}$, **H. Lohani**, P. Mishra, K. Majhi, A. Banerjee, A. K. Yadav, R. Ganesan, P. S. Anil Kumar and B. R. Sekhar, DAE Solid State Physics Symposium(DAE-SSPS),**2016 (26 - 30 December)**, *KIIT University, Bhubaneswar*, *AIP Conference Proceedings* (**Accepted**).

2. Photoemisson study on high H_{c2} superconductors $Nb_2Pd(Se/S)_5$ **H. Lohani**, P. Mishra, V. P. S. Awana, and B. R. Sekhar, Emerging Trends in Advance Functional Materials(ETAFM), **2016 (18 - 21 January)**, *I.O.P, Bhubaneswar*.

3. Electronic structure study of Nb_2PdS_5 using first principles method, **H. Lohani**, P. Mishra, V. P. S. Awana, and B. R. Sekhar, Current Trends in Condensed Matter Physics(CTCMP), **2015 (19 - 22 February)**, *NISER, Bhubaneswar*.

Date: **Signature of Student**

To My Late Nana ji

Acknowledgement

My present thesis work could be accomplished only by the generous support I got from many people and I am pleased to acknowledge all of them.

First and foremost, I would like to express my deepest gratitude and appreciation to my supervisor Prof. B. R. Sekhar, who provided me the opportunity to work with him. He supported throughout my research journey on all aspects. Only because of his ineffable guidance I could imbibe the fundamentals of photoemission spectroscopy, data analysis and instrumental handling *etc*. Similarly, these are his personal endeavors which inculcated a perspective of true research into me. Apart from these, affection received from all his family members, respected mother, mother-in-law and wife Ranjana madam will always remain memorable to me. I can never forget those blissful moments seeing the very innocent smile of sweet little girl Kartyayani and her lisping to tell many things. These will remain treasures for me forever.

Next, I would like to acknowledge all my collaborators. I am thankful to Prof. P. S. Anil Kumar (IISc, Banglore) for providing samples of topological insulators. I learned quite a lot about topological insulators from him through various discussions and telephonic conversations. I thank Dr. V. P. S. Awana (NPL, New Delhi) for providing the superconducting compounds. I express my regards to Prof. S. R. Barman (UGC-DAE, Indore) and Prof. K. S. R. Menon (SINP, Kolkata) for giving me an opportunity to visit their group and performing experiments in their labs. Discussions with them during those visits were highly educative to me. I thank Prof T. S. Dasgupta (SNBOSE, Kolkata) and Prof. J. Bhattacharjee (NISER, Bhubaneswar) for their initial guidance in DFT calculations, and Prof. D. topwal (IOP, Bhubaneswar) for synchrotron measurements. I am grateful to all the instructors of the pre-doctoral course work, especially Prof. A. Khare, Prof S. M. Bhattacharjee, Prof. A. Srivastava and Prof. A. Basu for their excellent classes which not only imparted knowledge on physics but also enormously enriched my ability of thinking. I would also like to extend my sincere gratitude to all my Ph. D review committee members, Prof. S. Varma, Prof. T. Som and Prof. G. Tripathi for their critical evaluation of my research work annually which refined my thesis in many ways. Along the same line, I pay regards to the HBNI dean Prof. P. Agrawal, for his considerate help at various occasions, mainly at the time of sixth and seventh year extensions and thesis submission.

It is a pleasure to express my heartfelt gratitude to my senior Dr. P. Mishra under whose leadership I learned several aspects of instrument handling in a very amicable environment. I am also thankful to her for the various academic discussions we had frequently. I also pay my deep regards to my supersenior Dr. R. Kundu. Although the overlap between our Ph.D course works was small, it was quite worthwhile in terms of learning instrument-handling and academic discussions.

I am also thankful to Dr. M. Chakraborty who during his very short visit introduced me to LMTO code and motivated me to learn electronic structure calculations in detail. I also express my heartfelt respect to Dr. Y. Nohara for his elaborative mail replies which helped me to understand the basics of LMTO. I also acknowledge all the eminent scientists who developed Quantum espresso, LMTO and Wannier 90 codes of electronic structure calculations and made them accessible to all. These codes helped me a lot in the interpretation of the results of my experiments.

I am thankful to Mr. Santosh K. Choudhury for his technical help at various occasions. My sincere regards to Er. Arun K. Das for his timely help. I am also thankful to all the IBL staff, specially Mr. Anup Behera, Mr. Dinesh and Mr. K. C. Patra for their help by providing liquid nitrogen and other technical assistance at different times. The support provided by the workshop staff, Mr. Rabi N. Naik and Mr. S. Tripathy, especially during the modification of baking boxes was really thankworthy. In addition, I need to mention Mr. Manoj Maduali for his timely and effective service related to the intel cluster computing system of IOP.

I express my high gratitude to the institute for providing me several amenities, like computer centre, excellent library, hostel accommodation *etc*. I am thankful to all the institute staff, specially Mr. R. C. Hansdah, Mr. Duryodhen Sahoo, Mr. K. C. Jena, Mr. Rajesh Mohapatra, Mr. Aviram Sahoo, and Mr. Sanatan Jena for their support. I will be forever greatful to the hostel mess for its support during the entire course of my Ph.D life. I express my very heartfelt regards to all the mess staff, specially Mr. G. C. Dash, Mr. B. Swain and Mr. B. K. Das. They not only prepared meals even at very odd times but also joyfully shared their views on various things of everyday life overcoming the barrier of language.

I am fortunate enough to have batchmates like Shailesh, Shalik, Mohit, Arnab, Anjan, Subhadip, Sazim, Maink and Anwesha. The moments I spent with these loving friends will always remain memorable to me. Similarly, I will cherish the memories of scholar hall F-26, where I accomplished most of my research articles and thesis work in a friendly and enjoyable company of Shailesh, Soumyabrata and Bharat. I am also very much thankful to all my senior scholars, specially Jim Da, Trilochan Da, Sankhadeep Da, Sourabh Da, Jatis Da, Jaya Di, Tanmoy Basu Da, Raghavendra Da, Shubhashis Da, Partha Da, Tanmoy Da, and Rama Da and my junior scholars, specially Subrat, Puspendu, Sudipta, Priyo, Shreyansh, Ranveer, Mahesh, Pronoy, Arpan, Paramita, Debashis, Chandan and Ashis who made my stay at IOP homely. I am happy to mention my thanks to Ashish Kundu, Sukanta, Dr. Maniraj, Dr. Jayita nayak and Dr. Abhishek for their hospitality and cooperation during my academic visits to SINP Kolkata and UGC-DAE Indore. I also would like to remember that it is essentially the efforts and teaching of my past teachers from primary standard up to master's level which lead me to the current academic position. I will remain indebted to all of them forever.

I want to acknowledge my family members but it is beyond my capacity to frame my emotions into words for their affection, moral support, motivation. I can only express my obligations to them as a deep silence. I dedicate this thesis to my nanaji the late Badri Dutt Joshi, who unfortunately didn't stay in this world long enough to see this thesis completed.

Himanshu Lohani

Contents

Table of Contents x

Synopsis xi

List of Figures xix

1 Introduction 1

1.1 Topological Insulator 1

1.1.1 Properties of Bi based TIs 3

1.2 Superconductors 8

1.2.1 Noncentrosymmetric SC BiPd 10

1.2.2 Pd based ternary chalcogenide SCs 11

1.2.3 Fe based chalcogenide SCs 12

2 Experimental Methodology 19

2.1 Photoemission Spectroscopy 19

2.1.1 Basic principles of photoemission 20

2.1.2 Theory of photoemission 22

2.2 Photoemisson set-up 26

2.3 Experimental Operation 31

3 Details of Calculations 36

3.1 Density Functional Theory 36

3.2 Methods of band structure calculations 42

3.2.1 Linear muffin-tin method(LMTO) 42

3.2.2 Plain Wave method 46

4 A Comparative ARPES study on Bi_2Se_3 and BiSe topological insulators 51

4.1 Introduction 51

4.2 Experimental Details 52

4.3 Results and Discussion 53

4.4 Conclusion 58

5 Band Structure of Topological Insulator BiSbTe$_{1.25}$Se$_{1.75}$ 61

5.1 Introduction 61

5.2 Experimental and Calculation Details 62

5.3 Results and Discussion 63

5.4 Conclusion 75

6 Fermi Surface and Band Structure of BiPd from ARPES Studies 79

6.1 Introduction 79

6.2 Details of experiment and calculation 81

6.3 Results and discussion 81

6.4 Conclusion 89

7 Valence Band Electronic Structure of Pd Based Ternary Chalcogenide Superconductors 93

7.1 Introduction 93

7.2 Experimental and Calculation Details 94

7.3 Results and Discussion 95

7.4 Conclusion 104

8 Investigation of correlation effects in FeSe and FeTe by LDA+U method 107

8.1 Introduction 107

8.2 Details of Calculation 108

8.3 Results and Discussion 109

8.4 Conclusion 117

9 Summary 121

Synopsis

Physics of various states of solids, like crystalline, magnetic, superconducting *etc.* has always remained a highly attractive area of research in both theoretical and experimental condensed matter physics. Studies of these states are not only important from the fundamental point of view but for various technological applications as well. This field has been revolutionized by the discovery of quantum hall effect (QHE) in 1980 [3] and the recent discovery of topological insulators (TIs) [6] which are topologically distinct states in comparison to the previously known states of the matter. Photoemission spectroscopy (PES) has played a major role in the discovery and understanding of TIs. PES is one of the direct techniques capable of probing the electronic structure of materials which provides information on the dispersion of electronic energy states. In the recent past, this spectroscopy has gone through tremendous technological advances in terms of energy resolution and measurement modes of analyzers enabling studies of very low energy electron dynamics especially in a narrow window of a few k_BT near the Fermi level (E_f). In the present thesis work, we have utilized modern electron analysers to explore the electronic structure of some Bi and Pd based compounds belonging to two distinct states of matter, *i. e.* the TIs and superconductors (SCs). I have used angle resolved (integrated) photoemisson spectroscopy (AR(I)PES) in conjunction with density functional theory (DFT) based calculations. For the DFT calculations we used first principles method which are implemented in quantum espresso (QE) [20] and tight binding linear muffin tin orbitals (TBLMTO) [5] codes.

TI possesses metallic surface states (SSs) while its bulk is insulating. These SSs exhibit very peculiar nature like, spin non-degeneracy, spin-momentum locking, robustness to Anderson localization and immunity for backscattering from any nonmagnetic impurities [1, 2]. The current generated through these SSs is nearly dissipationless and expected to be ideal for various electronic transport devices [7]. Its strong spin filtered nature can provide an excellent ground for quantum computing [30]. Apart from this, many other exotic properties, like Dirac fermion [3], Majorana fermion [7] and magnetic monopole [4] are also expected from these SSs as per theoretical predictions. Therefore, the SSs in TIs are also defined as nontrivial, unlike trivial SSs in normal insulators and this nontrivial character of the SSs is totally governed by the topology of bulk band structure [1]. In past few years, several materials have been found to host topologically insulating states and among them Bi based TIs are the most studied materials owing to their simple structures, easy synthesis routes with appropriate stoichiometry and chemical manipulations [1, 2]. We investigated the electronic structure of Bi based TIs BiSe, Bi_2Se_3 and $BiSbTe_{1.25}Se_{1.75}$ using ARPES experiments and *ab initio* calculations. The results are presented in chapter 4 and 5 of the present thesis. The first three chapters of this thesis briefly describe TIs and SCs, experimental methodology and calculation methods.

Bi_2Se_3 is a prototypical example of three dimensional(3D) TIs and its primitive unit cell is a rhombohedral structure where Bi and Se atoms are arranged in a fashion, like a quintuple layer (QL). $BiSbTe_{1.25}Se_{1.75}$ is isostructural to Bi_2Se_3. In BiSe crystal a Bi bilayer resides between the two adjacent QL of Bi_2Se_3. In our comparative ARPES study on Bi_2Se_3 and BiSe we observe Dirac like linearly dispersive bands in the energy gap region of Bi_2Se_3 which originate from the SSs. These states gradually shift towards higher binding energy (BE) as a function of time after the cleaving which is due to band bending (BB) effects. The BB in TIs originate from accumulation of additional charges at the surface. These extra charges arise due to Se vacancies present in the bulk as well as those created at the surface in the process of surface cleaving [34]. The extra charges at the surface and its periodic rearrangement inside the bulk creates a Coulomb potential of long ranged order contributing to the BB effects [35]. Interestingly, the surface state bands (SSBs) in BiSe resemble the Rashba split(RS) states. The effects of BB are also seen in this system which drag the SSBs to higher BE. The RS states could be originated from the coupling between Bi bilayer and adjacent QL. This difference in the observed SSBs in BiSe and Bi_2Se_3 resulting from their weak and strong topological nature despite having the same elemental composition sheds light on the importance of structural geometry to decide the topological properties in Bi based binary compounds.

Recent breakthrough in the arena of Bi based TIs is the discovery of quaternary alloy $Bi_{2-x}Sb_xTe_{3-y}Se_y$ which provides an ideal platform to study the nature of topological SSs by tuning the Dirac node within the bulk energy gap by controlling the proportion of chalcogen/pnictogen atoms [14]. Our experimental studies using ARPES and first principles based band structure calculations confirmed the non-trivial topology of the SSBs in one of the member of quaternary alloy family *i. e.* $BiSbTe_{1.25}Se_{1.75}$. We found quite a prominent hexagonal warping of the Fermi surface (FS) in this compound and the estimated value of this warping strength lies between those reported in case of Bi_2Se_3 and Bi_2Te_3. Similarly the DP shifts by more than two times compared to the movement observed in Bi_2Se_3 to reach the saturation under the influence of BB effects indicating that the BB is stronger in $BiSbTe_{1.25}Se_{1.75}$ compared to that in Bi_2Se_3. Moreover, the charge distribution at the surface is also affected by adsorption of residual gases [11]. In order to confirm the role of adatoms in the BB effects, we studied this system as a function of temperature and different residual gas environment condition. These experiments reveal that the BB is highly sensitive to the exposure to various gas species. With the exposure to Ar and N_2 gases, bands bend towards lower BE which is opposite to the behavior seen in the dosing of O_2 gas. The difference in the BB strength between Bi_2Se_3 and $BiSbTe_{1.25}Se_{1.75}$ could be due to the different screening of the surface charges because of the difference in composition of the QLs of the two compounds. Our comprehensive study demonstrates that the presence of different pnictogen (Bi,Sb) and chalcogen (Se,Te) atoms drastically modifies the topological properties of the quaternary TI $BiSbTe_{1.25}Se_{1.75}$ in comparison to the binary TI Bi_2Se_3.

Superconductivity is another exotic state of the matter [38] whose main characteristic is disappearance of resistivity at certain temperature defined as superconducting transition temperature (T_c). Chapter 6 deals with FS and band structure mapping of BiPd which is a noncentrosymmetric(NCS) SC with a T_c is $\sim$ 3.7 K [17]. BiPd has brought a new excitation to the field of NCS SCs due to the strong spin-orbit coupling (SOC) and moderate electronic correlation arising from the presence of heavy elements Bi (Z = 83) and Pd (Z = 46). This unique combination offers an excellent opportunity for investigating the role of antisymmeteric SOC effects in the electronic structure of NCS SCs. BiPd shows a transition from orthorhombic (β-BiPd) to monoclinic(α-BiPd) structure at 210°C. In the crystal structure of α-BiPd Bi and Pd atoms are arranged in two adjacent double layers.

In our ARPES study of BiPd, we looked at the various bands crossings the E_f along both the Γ-X and Γ-T directions. The FS depicts high intensity distribution at various parts of the surface BZ resulting from various electron and hole like bands which are present in the vicinity of the E_f. These results are consistent with the high metallic nature of BiPd observed in resistivity measurements. One hole pocket around the Γ point and an electron pocket around the X point are also identified from the near E_f ARPES intensity plots. The ARPES results show a fairly good agreement with the calculated band structure, mainly in the higher BE region, though the bands are not very discernible as predicted in the calculations. Our orbital resolved DOS calculations reveal that the near E_f states are primarily composed of Bi-6p orbitals with a little admixture of Pd-4$d_{x^2-y^2/zy}$ while the states at higher BE ($\sim E_b$ = -1.2 eV) are dominated by Pd-4d orbital character. This near E_f region is significantly modified by the inclusion of SOC effects and various new hole and electron pockets arising from the spin-orbit split bands appear in comparison to the non-relativistic case. FS manifested by these bands consists of multi sheets of different dimensions, mainly three dimensions which disfavor the nesting conditions and weakens the possibility for any density wave instabilities in this system. Since, spin split bands in ASOC driven systems have different spin rotation restricting the spin-triplet pairing at specific parts of the FS, like in NCS SC LaPtSi, the pairing should mainly be of singlet nature mediated via phonons.

Discovery of Pd based ternary chalcogenides, like $Nb_2Pd_{0.95}S_5$ [6, 7], Nb_2PdSe_5 [8], Ta_2PdS_5 [9], $Ta_2Pd_{0.97}S_6$ [10], $Ta_2Pd_{0.97}Te_6$ [11] and $Ta_4Pd_3Te_{16}$ [12] is another advancement in the field of SCs. These layered compounds provide a fertile ground for the existence of unconventional superconducting state owing to their Quasi-2-dimensional (Q2D) character [13]. Interesting compounds in this low dimensional family, are $Nb_2Pd_{0.95}S_5$ and $Nb_2Pd_{1.2}Se_5$ which are isomorphic and have $T_c \sim 6$ K. $Nb_2Pd_{0.95}S_5$ shows a Fermi liquid behavior at low temperatures. Sommerfiled coefficients estimated for $Nb_2Pd_{1.2}Se_5$ and $Nb_2Pd_{0.95}S_5$ i.e 15.7 and 32 mJ/mol-K^2 respectively, indicate moderately and strongly coupled electronic interactions respectively in them. On the other hand, ternary compounds such as $Ta_2Pd_{0.97}S_6$

and $Ta_2Pd_{0.97}Te_6$ belonging to the same monoclinic structure ($C_{2/m}$) like $Nb_2Pd_{0.95}S_5$, show a different behavior. These compounds share a common structure composed of chains of Pd and Nb/Ta centred polyhedra with S/Te atoms. Changes in the structural geometry is a key factor determining the different physical behavior of these ternary SCs, In chapter 7 we present a comprehensive photoemisson study on some of these ternary SCs $Nb_2Pd_{0.95}S_5$, $Nb_2Pd_{1.2}Se_5$, $Ta_2Pd_{0.97}S_6$ and $Ta_2Pd_{0.97}Te_6$ in conjugation with DFT based calculations. We observe that the VB spectra of $Nb_2Pd_{0.95}S_5$, $Nb_2Pd_{1.2}Se_5$, and $Ta_2Pd_{0.97}S_6$ are qualitatively similar except some slight differences in the energy position of various features. On the other hand, the VB spectra of $Ta_2Pd_{0.97}Te_6$ is remarkably different, particularly in the near E_f region where a clear metallic edge is observed, unlike the other compounds. Our study also shows the existence of a temperature dependent pseudogap in $Nb_2Pd_{0.95}S_5$ while the near E_f states remain unchanged with the lowering of temperature to 77 K in $Nb_2Pd_{1.2}Se_5$, $Ta_2Pd_{0.97}S_6$ and $Ta_2Pd_{0.97}Te_6$. In our calculated DOS, states crossing the E_f are dominated by different Pd-4d and Nb-4d orbitals ensuring significant role for multiband effects in $Nb_2Pd_{1.2}Se_5$ and $Nb_2Pd_{0.95}S_5$ compounds. Our comprehensive study provides a deeper insight into the VB states of these Pd based ternary compounds in correlation with their different structural geometry.

Further covering the field of SCs, we have studied electronic structure of FeSe and FeTe members of $FeSe_{1-x}Te_x$ family of Fe-SCs which have gained much attention due to their strongly correlated nature, unlike other SCs. These results are presented in the last chapter of this thesis. Superconductivity in the $FeSe_{1-x}Te_x$ compounds was first reported by Hsu *et al.* [4] in the FeSe (x = 0) compound exhibiting a $T_c \sim 8$ K which rises up to 37 K under pressure (7GPa) [5]. Both FeSe and FeTe have tetragonal crystal structure consisting square planar sheet of Fe atoms which is tetrahedraly coordinated with anion (Se/Te) atoms. Our angle integrated valence band photoemission study on $FeSe_{1-x}Te_x$ [18] compounds revealed formation of a pseudogap in the near E_f region with Se doping and also a temperature dependent orbital selective spectral weight transfer in these compounds. Motivated by these observations we performed a detailed investigation of the effect of Coulomb interaction and Hund's coupling in the Fe-3d states in FeSe and FeTe using LDA+U method employed in TBLMTO. In both the compounds states around the E_f originate predominantly from Fe-3d orbitals having a pseudogap feature just above the E_f. The hybridized states between Fe-3d and chalcogen-p orbitals which lie at higher BE, depend heavily on the chalcogen height from the Fe plane and are weak in case of FeTe where the height of Te anion is higher in comparison to Se in FeSe. The Coulomb interaction localizes and shifts the Fe-3d states towards higher BE energy in both the compounds, however this interaction is strongly screened by the Te-p bands in FeTe. It is observed that this effect is significant in $d_{yz/xz}$ and $d_{x^2-y^2}$ states in case of FeSe. Electrons in these localized states again become itinerant under the influence of J and distinct orbital selective changes are seen in the electronic structure. Similar to U, Hund's coupling effect is also prominent in

FeSe in comparison to FeTe. The difference in the anion tetrahedra geometry results in different orbital selective behaviors of the correlation effect in both the compounds.

Bibliography

[1] von Klitzing, K., G. Dorda, and M. Pepper *Phys. Rev. Lett.* **45** (1980) 494.

[2] Bernevig, B. A., T. L. Hughes, and S. C. Zhang *Science* **314** (2006) 1757.

[3] Stefan H*ü*fner, Photoelectron Spectroscopy: Principles and Applications, **Springer**, (1996).

[4] Giannozzi P. et al. *http:/www.quantum-espresso.org*.

[5] R. W. Tank, O. Jepsen, A. Burkhardt and O. K. Andersen, *The Stuttgart TB-LMTO-ASA programe*,**Version 47**.

[6] M. Z. Hasan and C. L. Kane *Rev. Mod. Phys.* **82** (2010) 3045.

[7] Xiao-Liang Qi and Shou-cheng Zhang *Rev. Mod. Phys.* **83** (2011) 1057.

[8] Liang Fu and C. L. Kane *Phy. Rev. Lett.* **102** (2009) 216403.

[9] Joel Moore *Nat. Phy.* **5** (2009) 378.

[10] Y. Xia, D. Qian, D. Hsieh, L.Wray, A. Pal, H. Lin, A. Bansil, D. Grauer, Y. S. Hor, R. J. Cava and M. Z. Hasan *Nat. Phys.* **5** (2009) 398.

[11] Liang Fu and C. L. Kane *Phy. Rev. Lett.* **100** (2008) 096407.

[12] Xiao-Liang Qi, Rundong Li, Jiadong Zang, Shou-Cheng Zhang *Science* **323** (2009) 1184.

[13] Zhi Ren, A. A. Taskin, Satoshi Sasaki, Kouji Segawa, and Yoichi Ando *Phy. Rev. B.* **84** (2011) 165311.

[14] P Rakyta, B Ujfalussy and L Szunyogh *New. J. Phys.* **17** (2015) 123011.

[15] T. Forster, P. Kruger and M. Rohlfing *Phy. Rev. B.* **91** (2015) 035313.

[16] Hadj M. Benia, Chengtian Lin, Klaus Kern, and Christian R. Ast *Phy. Rev. Lett.* **107** (2011) 177602.

[17] Manfred Sigrist *AIP Conf. Proc.* **789** (2005) 165.

[18] Bhanu Joshi, A. Thamizhavel and S. Ramakrishnan, *Phys. Rev. B.* **84** (2011) 064518.

[19] R. Jha, B. Tiwari, P. Rani, H. Kishan and V. P. S. Awana *J. Appl. Phys.* **115** (2014) 213903.

[20] Q. Zhang, G. Li, D. Rhodes, A. Kiswandhi, T. Besara, B. Zeng, J. Sun, Siegrist, M. D. Johannes and L. Balicas *Scientific Reports* **3** (2013) 1446.

[21] Seunghyun Khim, Bumsung Lee, Ki-Young Choi1, Byung-Gu Jeon, Dong Hyun Jang, Deepak Patil, Seema Patil, Rokyeon Kim, Eun Sang Choi, Seongsu Lee, Jaejun Yu and Kee Hoon Kim *New J. Phys.* **15** (2013) 123031.

[22] Y. F. Lu, T. Takayama, A. F. Bangura, Y. katsura, D. Hashizume and H. Takag *J. Phys. Soc. Japan* **83** (2014) 023702.

[23] B. Tiwari, B. B. Prasad, R. Jha, D. K. Singh and V. P.S. Awana *J. of Super. Nov. Magn.* **27** (2014) 2181.

[24] R. Goyal, B. Tiwari, R. Jha, and V. P.S. Awana *J. of Super. Novel. Magn.* **28** (2015) 119.

[25] Wen-Hu Jiao, Zhang-T Tang, Yun-Lei Sun, Y. Liu, Q. Tao, Chun-Mu Feng, Yue-Wu Zeng, Zhu-An Xu and Guang-Han Cao *J. of Am. Chem. Soc.* **136** (2014) 1284.

[26] J. Pan, W. H. Jiao, X. C. Hong, Z. Zhnag, L. P. He, P. L. Cai, G. H. Cao and S. Y. Li *Phys. Rev. B* **13** (1976) 3284.

[27] B. S. Chandrasekhar *Appl. Phys. Lett.* **1** (1962) 7.

[28] A.M. Clogston *Phys. Rev. Lett.* **9** (1962) 266.

[29] David J. Singh *Phys. Rev. B* **88** (2013) 174508.

[30] Masahiro Takahashi, Takeshi Mizushima and Kazushige Machida *Phys. Rev. B* **89** (2014) 064505.

[31] D.A. Zocco, K. Grube, F. Eilers, T. Wolf and H.v. Lohneysen *Phys. Rev. Lett.* **111** (2013) 057007.

[32] F.C.Hsu, J.-Y.Luo,K. W.Yeh, T. K. Chen, T. W. Hung, P. M. Wu, Y. C. Lee, Y. L. Huang, Y. Y. Chu, D. C. Yan and M. K. Wu *Natl. Acad. Sci. U.S.A.* **105** (2008) 14262.

[33] S. Margadonna, Y. Takabayashi, Y. Ohishi, Y. Mizuguchi, Y. Takano, T. Kagayama, T. Nakagawa, M. Takata, and K. Prassides *Phys. Rev. B* **80** (2009) 064506.

[34] P. Mishra, H. Lohani, R. A. Zargar, V. P. S. Awana and B. R. Sekhar *J. Phys. Condens Matter* **26** (2014) 425501.

List of Figures

1.1 Sphere (a) and ellipsoid (b) belong to same topological class but they differ from torus (c) topologically. The surface of torus is topologically equivalent to cylinder (d) but not to the object (e) which has more number of surfaces. 2

1.2 (a) and (b) Primitive and hexagonal unit cell structure of Bi_2Se_3 respectively. The basic building block of this system is called quintuple layer (QL) which is marked as a rectangular box in the unit cell (b). 4

1.3 Example of trvial (a) and nontrivial (b) surface states in insulator [1]. 5

1.4 (a) BZ of Bi_2Se_3 with parity eigen value at different TRIM points. (b) A schematic picture of band inversion induced by SOC effects [11]. 6

1.5 (a) Linear Dirac like dispersion of SSBs and (b) their spin helicity observed in Bi_2Se_3 [1]. 7

1.6 (a) A pictorial presentation of quasiparticle spectrum where solid line depicts the spectrum of an energy gap 2Δ and dashed line shows spectrum for $\Delta = 0$ with the same quasiparticle occupation. (b) A schematic of energy dependence of renormalized Coulomb interaction under electron-phonon coupling where it is attractive for energies $\leq |\varepsilon_D|$ and repulsive otherwise [38]. 9

1.7 Crystal structure of BiPd. 11

1.8 Crystal structure of $Nb_2Pd(Se/S)_5$. 12

1.9 Crystal structure of FeSe. 13

2.1 (a) A schematic picture of photoemission experiment where the characteristics of photoelectron are defined by its kinetic energy (E_{KE}) and momentum (**p**). The value of momentum is determined from the polar angles(θ and ϕ) of emission. (b) An intuitive representation to describe the energy level profile inside the solid and resulting photoemission spectra. (c) A rough sketch of photoelectron detection in our experimental set-up. In this geometry, photoelectron emitting in the angular range $\pm\phi$ at fix θ value which represents different values of $K_{\|}$ along the x-axis can be measured simultaneously. By varying the value of θ different parts of the Brillouin zone can be covered. 21

2.2 Schematics of three (a) and one (b) step model to elucidate the process of photoemission (taken from Ref. [19]). 23

2.3 Energy level diagram to demonstrate the dependency of the matrix element($M_{f,i}$) on photon energy in the PE process. The low (high) energy final states mainly overlap with low (high) angular momentum initial states and different final states can be accessed by just varying the photon energy (taken from Ref. [19]). 24

2.4 Image of photoemission system in our laboratory. Important parts of the system are labeled in the image. 26

2.5 Image of the system at different angle in order to provide a clear view of the preparation chamber. 27

2.6 (a) Image shows the working principle of modern electron spectrometer of Scienta. Photoelectrons emanating from the sample in a certain angular range can be collected from the lens system which pass through the analyzer and then detected by the multi channel multiplier and simultaneously a 2D intensity image of energy vs momentum is obtained from the CCD camera. (b) Example of the intensity plot where the vertical and horizontal scales correspond to binding energy (BE) and parallel component of the momentum of photoelectrons and cuts (red and green) along the same directions are used to extract energy density curves (EDC) (c) and momentum density curves (MDC) (d) respectively. 28

2.7 Picture of the UV lamp head attached to the system where individual parts are marked for clarity. 30

2.8 A simplified presentation to illustrate the low energy electron diffraction (LEED) system. 31

2.9 Plot of an universal curve describing electron escape depth(λ) as a function of the KE of electron for various metals. 32

3.1 M$\ddot{u}$ffin-tin potential with atomic sphere approximation (ASA). 43

3.2 Graphical representation of pseudowavefunction and pseudopotential scheme. . . 47

4.1 (a) and (b) Primitive and hexagonal unit cell structure of Bi_2Se_3. (c) Crystal structure of BiSe. (d) LEED image of Bi_2Se_3 where high symmetry k-points Γ, K and M are marked. Blue arrow denotes Γ-K' direction along which bands are mapped and it is offset from Γ-K direction by 15° 53

4.2 (a) and (b) ARPES intensity plots of Bi_2Se_3 taken along the Γ-K' direction of the surface BZ using He-I(21.2 eV) and He-II(40.8 eV) photon energy respectively. . 54

4.3 (a) and (b) ARPES intensity plots of Bi_2Se_3 in the near E_f region taken ∼ 0:30 hr. and 11:00 hr. after the sample cleaving using He-I photon energy respectively. (c) and (d) EDC plots extracted from the images(a) and (b) respectively. 55

4.4 (a) ARPES intensity map taken along Γ-M direction of the surface BZ of BiSe. (b) and (c) are the same images taken along Γ-M' and Γ-M" directions which are 8° and 15° offset from the Γ-M direction respectively. (d) - (e) EDC plots obtained from the images(a) - (c) respectively. 57

5.1 (a) and (b) show the primitive and hexagonal unit cells of $BiSbTeSe_2$ respectively. The dotted box encloses the structure of five atomic layers which is called quintuple layer (QL). (c) Brillouin zone of the primitive unit cell where high symmetry k-points are marked. (e) LEED spots depict the hexagonal symmetry of the surface BZ of BSTS where the high symmetry k-directions Γ-K and Γ-M are marked. 64

5.2 (a) and (b) show bulk band structure plots of $BiSbTeSe_2$ without and with inclusion of SOC effects respectively. (c) and (d) show ARPES images of BSTS along the Γ-M and Γ-K directions of the surface BZ respectively. (e) and (f) show the bulk bands of (b) along the Γ-F and Γ-L directions respectively. 65

5.3 (a), (c), (e) and (g) correspond to the near E_f ARPES images taken at photon energy 35, 33, 31 and 28 eV respectively. (b), (d), (f) and (h) show EDC spectra corresponding to the images in (a), (c), (e) and (g) respectively. Intensity map using s and p-polarized photon energy of 31 eV are shown in (i) and (k) respectively. EDC spectra of these images are shown in (j) and (l) respectively. 67

5.4 (a) correspond to near E_f ARPES images taken at photon energy 31 eV. In (b) and (d) constant energy contour (CEC) are presented at binding energy E_f and E_d respectively, while (c) corresponds to CEC plotted at mid point energy(E_m) between the E_f and E_d taken at 31 eV photon energy. 67

5.5 (a) and (c) show calculated bands of Se1 and Te terminated face of 6QL slab geometry of $BiSbTeSe_2$ respectively. (b) Weight of atomic orbitals mainly contributing to the 'V' shaped band (enclosed in the black box) at the Γ point in Se terminated plain with respect to their distances from the surface. (d) Similar contribution to V shaped band at the Γ point(I^{st}) and slightly away from the Γ point(II^{nd}) in Te terminated face. 68

5.6 (a) and (b) depict the ARPES intensity plots taken at 31 eV photon energy along the Γ-K direction taken $\sim$ 10 and 27 hrs. after the sample cleaving. (c) and (d) show same images along Γ-M direction collected at different time intervals from the cleaving. (e)-(h) show MDC spectra extracted from the images (a)-(d). The dispersion relation between E and k estimated from the MDC plots are fitted to the calculated values obtained from the model Hamiltonian [32] along the Γ-K (i) and the Γ-M (j) directions. 69

5.7 (a)-(c) ARPES intensity plots around Γ point at different time periods after the cleaving. (d)-(f) ARPES images of thermal cycling 300 K-77 K-300 K. In (g) and (h) EDC spectra are plotted extracted in a small window around the Γ point from the ARPES images collected at different time scale after the cleaving. Similar EDC plots obtained from the ARPES images of thermal cycling like (d)-(f) are presented in (i). The inset of Fig.5.7 (h) and Fig.5.7 (i) show the spectral weight evolution of the near E_f states.Different colours (black → red → green → blue → magenta) of the EDC spectra represent various stages (300 K → 77 K → 300 K → 77 K → 300 K) of thermal cycling respectively. 71

5.8 (a), (b) and (c) ARPES images taken at 300 K-77 K-300 K respectively just after the cleaving(Ist thermal cycle) in Ar environment. (d)-(f) and (g)-(i) display ARPES images of the Ist thermal cycle performed under constant dosing of N_2 and O_2 gases respectively. (j), (k) and (l) correspond to EDC(taken around the Γ point) plots of thermal cycling under the exposure of Ar, N_2 and O_2 gases respectively, where the inset of each plots show the enlarged view of the near E_f region. Different colours (black → red → green → blue → magenta) of the EDC spectra represent various stages (300 K → 77 K → 300 K → 77 K → 300 K) of thermal cycling respectively. 73

6.1 (a) Crystal structure of α-BiPd. (b) The coordination environment of Bi(Pd). (c) The 2D surface Brillouin zone of BiPd where Γ, Z, X and T are the high symmetry k-points and blue arrows denote the k-directions of band mapping. 82

6.2 (a) and (e) ARPES intensity map of FS on Γ-Z and Γ-T plane respectively. (b)-(d) ARPES images of energy dispersion along different cuts #1 to #3 and (f)-(i) same images taken along cuts #4 to #7 respectively. (j) Comparison of angle integrated valence band spectra of BiPd collected at He-I(black) and He-II(red) photon energy. 83

6.3 (a)-(e) show near E_f region of ARPES intensity plot along cut#1, #3, #4, #6 and #7 and corresponding renormalized images(dividing by angular integrated spectrum) are shown in (f)-(j) respectively. (k)-(o) are plots of energy density curves(EDC) extracted from the images (a)-(e). 85

6.4 (a) Band structure plot of BiPd obtained from non relativistic calculation. In this plot different bands, which cross the E_f are coloured, while bands residing in deeper BE are shown by dashed coloured lines. (b) and (c) DOS of individual Bi-6p and Pd-4d orbitals respectively, obtained by integrating the DOS of these orbitals to all the Bi and Pd atoms in BiPd. 86

6.5 (a) Band structure plot of BiPd with including the SOC effects. Different bands crossing the E_f are coloured while bands residing in deeper BE are shown by dashed coloured lines. (b) composite FS of BiPd. (c)-(f) Individual sheet of FS corresponding to calculated bands turquoise, indigo, blue and violet of the Fig. (a) respectively. 87

7.1 (a), (b) and (c) are crystal structure of $Nb_2PdS(Se)_5$, Ta_2PdS_6 and $Ta_4Pd_3Te_{16}$ respectively. Different nearest neighbours of Pd atom at inequivalent sites and bond lengths are marked in each structure. 96

7.2 (a) and (b) valence band spectra of $Nb_2Pd_{1.2}Se_5$(Green) $Nb_2Pd_{0.95}S_5$(Black), $Ta_2Pd_{0.97}S_6$(Red) and $Ta_2Pd_{0.97}Te_6$(Blue) obtained by using HeI and HeII excitation energy respectively taken at 300 K. (c) and (d) are an enlarge view of near E_f region of the (a) and the (b) respectively. 97

7.3 (a), (b), (c) and (d) show total calculated DOS with different atomic contributions of Nb_2PdSe_5, Nb_2PdS_5, Ta_2PdS_6 and $Ta_4Pd_3Te_{16}$ respectively. 98

7.4 DOS originated from different orbitals of Pd-4d at sites Pd1 and Pd2 are shown in (a) and (b) respectively for Nb_2PdSe_5. (c) and (d) show the DOS at Pd1 and Pd2 site respectively for Nb_2PdS_5. Inset of each plot shows coordination environment of each Pd atom in respective compound where cartesian axis are set in same orientation as shown in crystal structure image(Fig.7.1). Red, blue and green colour balls represent Pd, Nb, and S(Se) atoms respectively. 100

7.5 DOS originated from different orbitals of Nb-4d at site Nb1 and Nb2 are shown in (a) and (b) respectively for Nb_2PdSe_5. (c) and (d) show same DOS at Nb1 and Nb2 site respectively for Nb_2PdS_5. 101

7.6 (a) Pd_{4d} DOS in Ta_2PdS_6. (b) and (c) Pd_{4d} DOS at site Pd1 and Pd2 in $Ta_4Pd_3Te_{16}$ respectively. Inset of each plot shows coordination environment of each Pd atom in respective compound where cartesian axis are set in same orientation as shown in crystal structure images(Fig.7.1). Red, green, magenta and yellow colour balls represent Pd, S, Ta and Te atoms respectively. 102

7.7 Near E_f VB spectra of $Nb_2Pd_{1.2}Se_5$ and $Nb_2Pd_{0.95}S_5$ (a), $Ta_2Pd_{0.97}S_6$ (b) and $Ta_2Pd_{0.97}Te_6$ (c) collected at 300 K(Black) and 77 K(Red) with HeI energy. Same spectra collected at HeII energy are shown in (d), (e) and (f) respectively. Blue dots represent difference between the normalized spectra taken at 300 K and 77 K. Here, we have adopted the scheme of symmetrization to the spectra with respect to E_F in order to remove contribution arising from Fermi-Dirac distribution function. 103

8.1 Total and partial DOS plotted for FeSe in (a) and for FeTe in (b). In (c) and (d) total and partial DOS calculated with Se-p and Te-p valence orbitals downfolded in FeSe and FeTe respectively. Inset of (c) and (d) shows the anion tetrahedra in FeSe and FeTe. Fe, Se and Te atoms are denoted by red, green and blue colours respectively. 110

8.2 Changes in the Fe-3d states for different values of *U* are shown for FeSe (a) and FeTe (b). Values of *U* is shown in red colour in each plot. 111

8.3 Changes in the Fe-3d states for different values of *J* are shown for FeSe (a) and FeTe (b). Values of *J* is shown in red colour in each plot. *U* is fixed at 4.0 and 3.5 eV for FeSe and FeTe respectively. 112

8.4 Changes in the DOS of different d orbitals of Fe atom at different values of *U* and *J* are plotted for FeSe (a) and FeTe (b). Values of *U* and *J* are marked by green, black, red and blue colours in the Figure. 113

8.5 (a) and (b) show band structure plot of FeSe at $U = 0.0$ and $U = 4.0$ eV respectively. (c) and (d) show band structure plot of FeTe at $U = 0.0$ and $U = 3.5$ eV respectively. (e), (f), (g) and (h) show fatness of bands which originate from d$_{xy}$, d$_{yz/xz}$, d$_{x^2-y^2}$ and d$_{3z^2-r^2}$ orbitals respectively for FeSe at *U* and *J* = 0.0 eV. 114

8.6 Panel (a) and (b) shows band structure plot for FeSe and FeTe at different values of *J* = 0.0, 0.1, 0.8 and 1.2 eV from left to right. The value of *U* is set to 4.0 and 3.5 eV respectively in all FeSe and FeTe plots. 115

Chapter 1

Introduction

The present thesis is based on photoemission studies of some topological insulators (TIs) and superconductors (SCs) in conjugation with first principles band structure calculations. In this chapter, we describe some important features of these materials which are needed to understand the significance of our work in the context of recent activities in these fields. The chapter is divided into two parts which provide a brief introduction to the vast field of TIs and SCs.

1.1 Topological Insulator

The term "**Topology**" refers to one of the branch of mathematics that deals with quantities which remain invariant under a continuous transformation defined as topological invariance [1, 2]. This concept of topological invariance classifies the geometrical objects into broad categories as depicted in Fig.1.1. The surface of a sphere (Fig.1.1(a)) is topologically equivalent to the surface of an ellipsoid (Fig.1.1(b)) due to the former surface can be smoothly transformed to the later surface without any tearing of the surface. However, these surfaces can not be continuously deformed to surface of torus (Fig.1.1(c)) without creating a hole in them. Thus the torus, composed of two surfaces, belongs to a different topological class akin to cylinder (Fig.1.1(d)) topologically. Similarly, object Fig.1.1(e) is topologically distinct from the torus as it contains more number of surfaces. Here, integrals over local curvature of the surface is defined as topological invariants to characterize the surfaces because they depend solely on the global topology of the surface rather than the value of this integrand value.

It is interesting to note how this abstract idea of mathematics enters in the field of condensed matter physics. Before the advent of **quantum hall(QH)** effect in 1980 [3], the known states of the matter were defined under the framework of spontaneously broken symmetries. For example, the **crystalline state** destroys translational and rotational symmetry of space. Similarly, time reversal

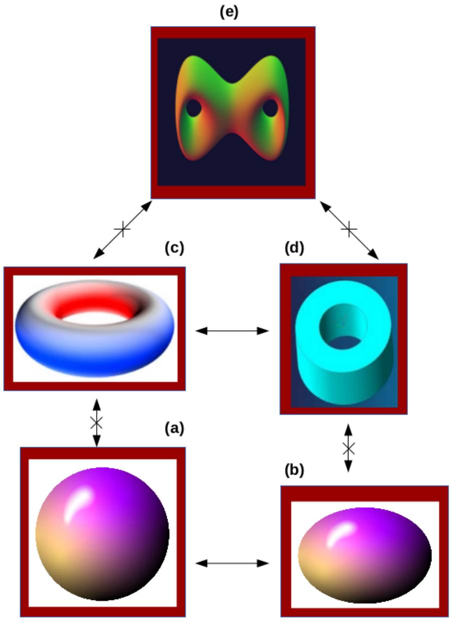

Figure 1.1: Sphere (a) and ellipsoid (b) belong to same topological class but they differ from torus (c) topologically. The surface of torus is topologically equivalent to cylinder (d) but not to the object (e) which has more number of surfaces.

symmetry (**TRS**) and rotational symmetry of spin space are broken by the **magnetic state**, while the **superconducting state** is associated with the breaking of gauge symmetry. However, the observation of precisely quantized Hall conductance in two dimensional (2D) materials can not be interpreted using this paradigm of symmetry breaking. The integer value of the Hall conductivity in units of e^2/h is defined as the first **Chern number**, a topological invariant [4, 5]. It signifies the presence of a nontrivial ground state which is the signature of a quantum state that is topologically distinct from the previously known states of the matter. This was the first example which unveiled the obvious connection between topology and physics *i. e.* a mapping of topological classes from the Brillouin zone(BZ) to the space of Bloch Hamiltonian. In physical systems, the operation of smooth deformation represents transformation amongst the different Hamiltonian describing insulating systems of energy gap of different sizes and shapes but all are considered to be in the same topological class. Likewise, integrals of the topological invariants are defined in ω-k space where integrand are physical quantities of quantized character. These invariants uniquely determine the nature of the quantum state and remain intact under the change, like varying the crystal lattice, changing coupling strengths and adding potentials to the Hamiltonian [1, 2].

The QH state mentioned above is driven by external magnetic fields which explicitly break the TRS in the system. Recently, a new electronic state of distinct topological nature *i.e* **quantum spin hall(QSH)** or **topological insulator(TI)** has been recognized in which compounds are insulating in the bulk but possess robust metallic states at surface [1, 2]. This quantum state emerges from the strong **spin-orbit coupling(SOC)** effects in combination with TRS which was first predicted theoretically in 2006 [6] and subsequently verified experimentally in quantum well structure of HgTe/CdTe in 2007 [7]. Similar to the Chern number in QH state, a topological invariant **$\mathbf{Z}_2$ = 1(0)** has been proposed to distinguish the topologically nontrivial (trivial) states [8]. The edge states in 2D QSH systems are composed of oppositely moving spin-up and spin-down electrons which could be considered as half of a quantum wire. Origin of these states lies on the spin and momentum dependent force induced by the SOC, analogous to a magnetic field which develops two independent quantum Hall states associated to electrons of opposite (up and down) spins. Soon after, Fu and Kane in 2007 [9] theoretically anticipated the existence of QSH state in 3D structure $Bi_{1-x}Sb_x$ alloy which was confirmed by Hseh *et al.* in 2008 [10] using angle resolved photoemission spectroscopy (ARPES) measurements. Subsequently, Zhang *et al.* [11], very soon predicted a more simpler 3D materials $Bi_2(Se/Te)_3$ and Sb_2Te_3 hosting nontrivial insulating states which were again experimentally realized using ARPES measurements shortly after the prediction in 2009 [12, 13]. These observations brought a great excitement to the field of TIs and established it to the front row amongst the research activities of condensed matter physics. This excitement created a flood of research articles, exploring several aspect of this novel state from both theoretical and experimental sides, in the recent past few years. Theoretically many materials have been proposed to be 3D TIs, particularly α-Sn [9], Sb [9], binary alloys $Bi_{1-x}Sb_x$ [14], Bi chalcogenides [11], HgTe [9], InSb [15], Bi ternary chalcogenides [13, 14], half Heusler alloys [18], Thallium based chalcogenides [19] and quaternary compounds [20] which host various exotic properties like, Dirac fermion [3], magnetic monopole [4], Majorana fermion [7, 8] at the proximity with SC. Veracity of the nontrivial topological character of some of the above mentioned compounds have been proofed experimentally. However, the Bi based binary TIs are the most studied materials due to their simple structures, possibility of easy synthesis with appropriate stoichiometry. In the following subsection we briefly describe the electronic properties of these materials which are relevant to our work.

1.1.1 Properties of Bi based TIs

The prototypical examples of Bi based 3D TIs are Bi_2Se_3 and Bi_2Te_3. Fig.1.2(a) shows primitive unit cell of Bi_2Se_3 which has a rhombohedral structure where layers of Bi(red) and Se(green) atoms are arranged in an order Se1-Bi-Se-Bi1-Se2. This arrangement holds a center of inversion at the Se atom site that makes Se1 and Bi atoms equivalent to Se2 and Bi1 atoms respectively. This

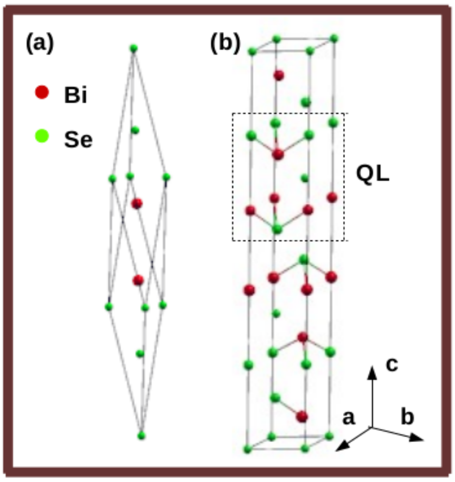

Figure 1.2: (a) and (b) Primitive and hexagonal unit cell structure of Bi_2Se_3 respectively. The basic building block of this system is called quintuple layer (QL) which is marked as a rectangular box in the unit cell (b).

peculiar arrangement is defined as a **quintuple layer(QL)** [11]. The more clear picture of this layered structure is apparent in a hexagonal unit cell as depicted in Fig.1.2(b). Bonding between the adjacent QLs is relatively weak and van der Wall in nature compared to the bonding within the QL. This bonding characteristic provides an easy cleaving which makes a mirror like 2D surface for ARPES measurements. The surface has its own characteristics different from those of bulk. This is because the Hamiltonian of bulk system, though remains unaffected in the direction parallel to the surface gets modified along the orthogonal direction due to the lack of symmetry along this direction. This leads to various interesting electronic energy states residing only at the surface known as **surface states(SSs)** [25]. However, these SSs are usually very fragile with respect to any change in the Hamiltonian except the newly discovered sturdy SSs in TIs. In the following we describe some of the basic facts that give rise to a topological protection to the SSs in TIs.

Inside the solid electrons of various wave vectors and spins are connected by the following relation under a time reversal symmetry and inversion symmetry of space

$$\begin{aligned} E(\mathbf{k},\uparrow) &= E(-\mathbf{k},\downarrow) \qquad \textbf{Time reversal symmetry} \\ E(\mathbf{k},\uparrow) &= E(-\mathbf{k},\uparrow) \qquad \textbf{Inversion symmetry} \end{aligned} \tag{1.1}$$

Thus electrons are spin degenerate inside the bulk until both the symmetries are preserved in the system. However, at the surface, the inversion symmetry is broken along the orthogonal direction to the surface that lifts translational symmetry and consequently the spin degeneracy. This splitting is significant in case of a strong **spin-orbit interaction(SOI)**, like in the Bi_2Se_3 due to presence of heavy element Bi(Z = 83). However, spin split states are forced to be degenerate at special k-points called **time reversal invariant momentum(TRIM)** due to combination of TRS and crystal

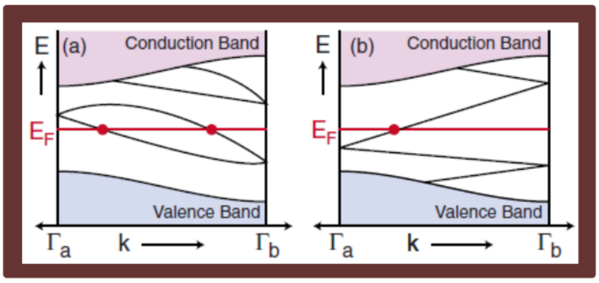

Figure 1.3: Example of trvial (a) and nontrivial (b) surface states in insulator [1].

symmetry [1]. Four and eight TRIM points exist in 2D and 3D systems respectively besides Γ point. They satisfy following relation

$$-\Lambda_i = \Lambda_i + G \qquad \text{where G is reciprocal lattice vector.}$$

Now, one possibility is that the spin degenerate states at one of the TRIM point become degenerate to the same spin partners at the adjacent TRIM point. In this case spin states cross the E_f even number of times between these two TRIM points(Fig.1.3(a)) and it can be feasible to shift these states on either side of the E_f by some impurity disorder or correlation effects. Thus, the metallic SSs are not robust and considered as a trivial SSs [1]. On the other side, if one of the spin degenerate state switches their partner at the other TRIM point then it crosses the E_f odd number of times(Fig.1.3(b)) between them which can not be eliminated by any small perturbations, like non magnetic impurities *etc*. This is called nontrivial nature of SSs which is one of the key element of TIs [1]. In this situation, metallic character of the surface persists all the way till the system remains gaped in the bulk. This odd/even number of crossing is decided only by the topology of the bulk band structure which is defined by four Z_2 topological invariants $\boldsymbol{\nu_0}$;($\boldsymbol{\nu_1, \nu_2, \nu_3}$) [9]. In case $\nu_0 \neq 0$ then system is classified as **strong topological insulator(STI)** while $\nu_0 = \nu_1 = \nu_2 = \nu_3$ = 0 indicates state of **normal insulator(NI)**. However, there is one more class *i. e.* **weak topological insulator(WTI)** where ν_0 = 0 and except any one of ν_1, ν_2, ν_3 rest all are 0. To calculate these topological invariants two recipes have been introduced one for centrosymmetric compounds based on parity criterion by Fu and Kane [9] and second for noncentrosymmetric systems formed on determination of Bloch functions(BFs) by Fukui and Hatsugai [26]. Below we illustrate the scheme of Fu and Kane on Bi_2Se_3 TI. The vlue of four independent invariants can be obtained

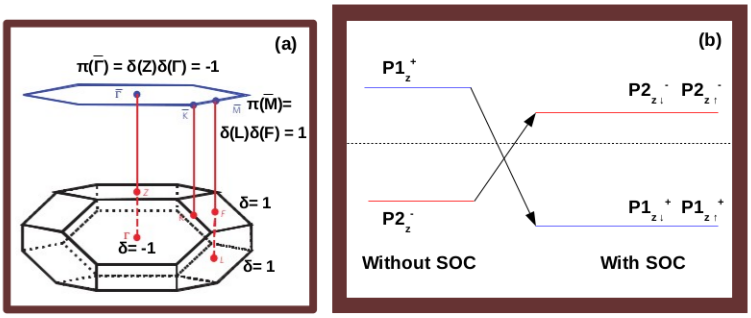

Figure 1.4: (a) BZ of Bi_2Se_3 with parity eigen value at different TRIM points. (b) A schematic picture of band inversion induced by SOC effects [11].

from the following relations.

$$\begin{aligned} (-1)^{\nu_0} &= \prod_{i=1}^{8} \delta_i \\ (-1)^{\nu_k} &= \prod_{n_k=1, n_j=0,1}^{8} \delta_i = (n_1, n_2, n_3) \end{aligned} \tag{1.2}$$

where δ_i can be obtained from parity analysis
$\delta_i = \prod_{m=1}^{Nocc} \xi_{2m}(\Gamma_i)$
Here $\xi_{2m}(\Gamma_i) = < \Psi_{2m,\Gamma_i} | \hat{P} | \Psi_{2m,\Gamma_i} >$ is the eigenvalue of parity operator $\hat{P}$ at the 2mth occupied band and Γ_i corresponds to eight different TRIMs. The $\xi_{2m}(\Gamma_i)$ can take either 1 or -1 value representing to even or odd parity of the BFs. In the (111) surface of Bi_2Se_3 the δ = -1 at the Γ point, whereas it is +1 at all the other TRIMs(F, L and Z) as depicted in Fig.1.4(a) [11]. This negative value at the Γ point originates from the inversion between bands of opposite parities *i. e.* conduction band edge($|P1_z^+ >$) and valence band edge ($|P2_z^- >$) due to strong SOC effects (Fig.1.4(b)) [11]. This contrast of parity eigen value also reflects at surface TRIM $\bar{\Gamma}$ and $\bar{M}$ points which provides a nontrivial character to the SSs in Bi_2Se_3.

These nontrivial SSs exhibit an interesting Dirac like linear energy dispersion in the bulk region of energy band gap around the Γ point. These SSs possess an unique property of spin-momentum locking that means each momentum along the surface has only a single spin state at the E_f. Further, the spin direction rotates as the momentum changes and encircles the TRIM by an odd number of times. In Bi_2Se_3 a clear Dirac like dispersion of the SSs has been observed in ARPES measurements(Fig.1.5(a)) and their spin helicity(Fig.1.5(b)) also been confirmed by spin resolved photoemission study [12]. Other features associated with these peculiar SSs are their robustness to Anderson localization and backscattering from nonmagnetic impurities. The origin of these features are rooted in TRS which causes a destructive interference between the two backscattering

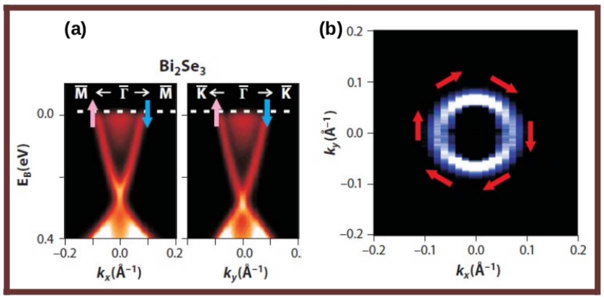

Figure 1.5: (a) Linear Dirac like dispersion of SSBs and (b) their spin helicity observed in Bi_2Se_3 [1].

paths around the impurity center and leads to perfect transmission [2]. These dissipationless SSs have tremendous scope to be utilized in transport applications [7, 8]. Similarly, the spin filtered nature of these states are thought to provide an avenue for the realization of fault-tolerant quantum computing. Apart from these, another fascinating behaviour has been observed in some of the TIs, like Bi_2Se_3 and Bi_2Te_3 that the **Dirac point**(meeting point of two linearly dispersive SSs) shifts towards higher binding energy(BE) as time elapses after the cleaving [9, 12]. This shifting is caused due to **band bending(BB)** effects originating from accumulation of additional charges at the surface. These extra charges arise due to Se vacancies present in the bulk as well as those created at the surface in the process of surface cleaving [35]. However, recent studies on Bi_2Se_3 have shown that not only the extra charges at the surface but also its periodic rearrangement inside the bulk creates a Coulomb potential of long range order contributing to the BB effects [35]. This unique property is inherent to the layered structure of Bi_2Se_3 where charge is accumulated and depleted at both the ends of each QLs. Similarly, chemical doping and adsorbtion of different gases are the other tools for influencing the surface charge density and thereby controlling the temporal evolution of DP. These results have also been noticed experimentally by several groups [10, 11] and have enormous possibility to fabricate excellent gas sensing devices [20].

However, the experimental realization of these interesting SSs properties are marred by significant contributions arising from the bulk states in the known Bi/Sb based binary TIs. Current breakthrough in this field is the discovery of tetradymite Bi_2Te_2Se TI [13] which is isostructural to known TIs, $Bi_2(Se/Te)_3$ but shows relatively large bulk resistivity [13]. It can be further optimized to the quaternary alloy $Bi_{2-x}Sb_xTe_{3-y}Se_y$ (BSTS) by changing the ratio of the pnictogen (Bi and Sb) and chalcogen (Se and Te) atoms without disturbing its crystallinity [14]. Thus, BSTS provides an ideal platform to study the nature of topological surface states by tuning the Dirac node within the bulk energy gap by controlling the proportion of chalcogen/pnictogen atoms. In addition to the stoichiometry, the role of structural geometry are quite decisive in the formation of topological character as clear from the current theoretical study on BiSe compound [35]. BiSe is also a layered material, like Bi_2Se_3 where a Bi bilayer sandwitched between two Bi_2Se_3 type QLs. However in this case interlayer coupling between the Bi bilayer and QL generates a weak topological insulating phase in this system contrary to the strong phase of topologically insulating character in Bi_2Se_3 [18].

We performed electronic structure study on Bi based TIs BiSe, Bi_2Se_3 and $BiSbTe_{1.25}Se_{1.75}$ using ARPES and *ab initio* calculations and our comprehensive study reveals the vital role of stoichiometry and structural geometry in deciding the topological properties in Bi based compounds.

1.2 Superconductors

Superconductivity is another beautiful state of the matter originating from spontaneous breaking of subtle gauge(U1) symmetry [38]. The main characteristic of this state is the sudden disappearance in resistivity at certain temperature defined as **superconducting transition temperature (T_c)** below which system behaves like a perfect conductor, *i. e.* "**super-conductor**". It was Kamerlingh Onnes who first succeeded to liquefy helium and thereby discovered the superconducting state in 1911 [39] on Mercury metal which showed a $T_c \sim 4$ K. In 1933, Meissner and Ochsenfeld [40] found SCs are also perfect diamagnets which further validated that it is a true thermodynamical state. Similarly, specific heat shows a discontinuous jump at T_c and then drops exponentially to low temperature, unlike its linear dependency on temperature seen in metals. Initially, phenomenological theories to explain the superconducting state were proposed by London brothers [41] in 1935, and also by Ginzburg and Landau. The more general microscopic theory came in 1957 from Bardeen, Cooper and Schrieffer [42] which is well known as **BCS** theory of superconductivity. Later Eliashberg extended the idea of weak **electron-phonon(e^-- ph)** coupling of BCS theory to strong e^-- ph coupling regime. The BCS theory describes that in the superconducting state an interesting phenomena occurs, where electrons despite their repulsive Coulombic interaction are paired known as **Cooper pairs**. These Cooper pairs obey Bose statistics contrary to the fermion character of electrons. The energy gain of the superconducting state with respect to normal state comes from the condensation energy of the electron pairs merging into a quantum state of macroscopic nature. This also leads to an energy gap for electrons excitation into single particle state as shown in Fig.1.6(a). In the weak coupling limit, the gap value can be estimated from the expression $\Delta(T = 0) = 1.764 k_B T_c$ and the condensation energy determined using relation $E_{cond} \equiv -1/2\ N_0|\Delta|^2$, where N_0 is the DOS at Fermi surface(FS) [38]. According to the BCS theory e^-- ph interaction overcomes the Coulomb repulsion through retardation effect and phonons

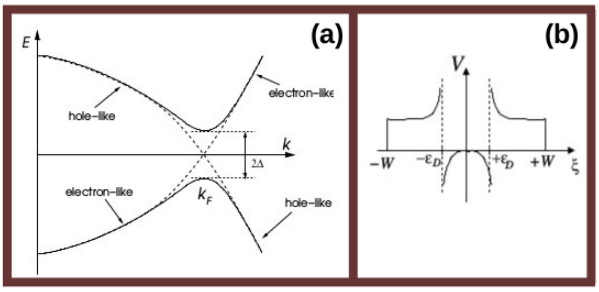

Figure 1.6: (a) A pictorial presentation of quasiparticle spectrum where solid line depicts the spectrum of an energy gap 2Δ and dashed line shows spectrum for Δ = 0 with the same quasiparticle occupation. (b) A schematic of energy dependence of renormalized Coulomb interaction under electron-phonon coupling where it is attractive for energies $\leq |\varepsilon_D|$ and repulsive otherwise [38].

act as a gluing agent between the pairing electrons. The energy range of the attractive interaction is limited to **Debye energy**($\hbar\omega_D$) around the E_f(Fig.1.6(b)). The wave function of Cooper pairs is defined as follows

$$\Psi(\vec{r}, s, \vec{r'}, s') = f(|\vec{r} - \vec{r'}|)\chi(s, s') \tag{1.3}$$

where first and second parts correspond to orbital and spin terms respectively.

Under the exchange of two pairing electrons, following two antisymmetric wavefunctions are possible

$$\begin{gathered}\Psi(\vec{r'}, s', \vec{r}, s) = -\Psi(\vec{r}, s, \vec{r'}, s') = f(-\{\vec{r} - \vec{r'}\})\chi(s, s') \\ \Rightarrow \begin{cases} f(-\vec{r}) = f(\vec{r}), & \chi_{s,s'} = -\chi_{s',s} \quad l = 0, 2, 4.... \ S = 0 \\ f(-\vec{r}) = -f(\vec{r}), & \chi_{s,s'} = \chi_{s',s} \quad l = 1, 3, 5.... \ S = 1 \end{cases}\end{gathered} \tag{1.4}$$

where S is the composite spin of pairing electrons. Here, wavefunctions with l = even(even parity) correspond to spin singlet pairing. while l= odd (odd parity) represents wavefunctions of spin triplet pairing. In general, SCs of l = 0 Copper pairs, which is the most symmetric pairing state, are called conventional SCs. On the other hand, SCs, where pairing state is l $>$ 0 are defined as unconventional SCs [38].

The BCS theory based on e^-- ph coupling explains satisfactorily different properties of superconducting state in metals, like Aluminum, Lead, Tin where e^-- ph coupling is dominant. However, various series of SCs have been discovered subsequently. Some of them are A15 compounds, example Nb_3Ga [43], V_3Al [44] *etc.*; heavy fermion SCs, example $CeCu_2Si_2$ [45], CePtSi [46] *etc.*; organic SCs, example $(TMTSF)_2ClO_4$ [47], (BEDT-TTF)$_2$Cu[N(CN)$_2$]Br [48] *etc.*; cuprate high temperature SCs, example $Bi_2Sr_2Ca_2Cu_3O_{10}$ [49], $YBa_2Cu_3O_7$ [50] *etc.*; Iron based SCs, example LaFeAsO [33], $BaFe_2As_2$ [52], FeSe [53] *etc.*; Pd based SCs, example BiPd [17], $Nb_2Pd_{0.95}S_5$ [6] *etc.* and hydrogen sulphide [56] which exhibits $T_c \sim$ 203 K. In many of these SCs, superconducting properties deviate from the prediction of BCS theory. For example, The value of T_c is significantly high from the estimation of McMillan's formula which indicates pairing mechanism must be different from e^--ph coupling. Similarly, the superconducting gap is not isotropic, like conventional s-wave SC but shows d-wave symmetry in cuprate family of high temperature SC and $s_\pm$ in Fe-SCs.

The primary reason for such anomaly is the involvement of electrons of localized d and f-orbitals which are substantially slower in their motion such that Coulomb interactions are comparable to the KE or even larger. Under such circumstances Coulomb interaction dominates over the attractive e^--ph coupling due to insufficient screening via retardation effects. There are other alternative mechanisms also conceptualized to understand the pairing in these unconventional SCs, for example spin fluctuation exchange, where spins can form a polarizable medium and lead to an effective interaction amongst electrons [38] and Cooper pairs of higher angular momentums $l > 0$, like l = 1(Sr_2RuO_4 [3]), l = 2(Cuprate SCs [49]) and l= 3(UPt_3 [58]). However, the exact picture of pairing mechanism in most of the high temperature SCs is still unknown and remains an intricate puzzle to unravel. In the following sections we introduce some newly discovered SCs which we have used for electronic structure study for present thesis work.

1.2.1 Noncentrosymmetric SC BiPd

BiPd is a **noncentrosymmetric(NCS)** SC which has a T_c is $\sim$ 3.7 K [17]. It shows a transition from orthorhombic(β-BiPd) to monoclinic(α-BiPd) structure at 210°C. Fig.1.7 shows the crystal structure of α-BiPd, in which Bi (Blue) and Pd (Red) atoms are arranged in two adjacent double layers. The bonding between alternative layers is weak and Bi(Pd) atoms are coordinated to Pd(Bi) atoms situated at seven nearest neighbour (nn) sites. One of the interesting aspect of the NCS crystals is broken inversion symmetry that gives rise to antisymmetric spin-orbit interaction(ASOC) which has been theoretically predicted to form an unconventional pairing in the NCS SCs. However, it has not been experimentally realized due to weak SOC in most of the NCS SCs, like $Mg_{10}Ir_{19}B_{16}$ [10], Mo_3Al_2C [11], $Re_{24}Nb_5$ [12], Re_3W [13] or strong correlation effects in some other SCs of NCS family, like $CePt_3Si$ [14], UIr [15].

In this scenario, discovery of superconductivity in NCS compound BiPd has brought some new excitement to this field due to the presence of heavy elements Bi (Z = 83) and Pd (Z = 46) SOC is expected to be strong while electronic correlation is moderate in this compound as suggested by Kadowaki-Woods value estimated from resistivity measurements [16]. Therefore, it provides an excellent ground to study the role of SOC effects in the electronic structure of NCS SCs. Physical properties of BiPd, like electrical resitivity, magnetic susceptibility and heat capacity

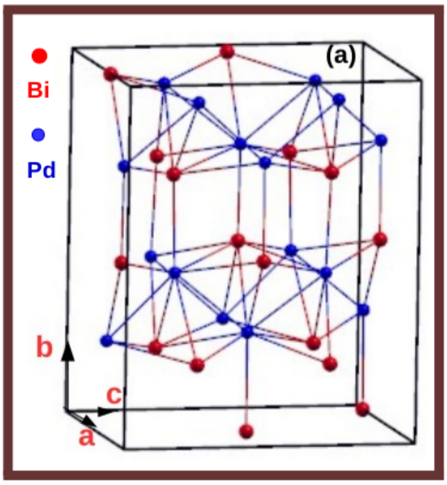

Figure 1.7: Crystal structure of BiPd.

have informed that it is a s-wave type BCS SC [17, 19] while some measurements, like Andreev spectroscopy [20], nuclear quaderpole resonance(NQR) [21] and London penetration depth [22] have found signals of spin-triplet pairing coexisting with spin-singlet component. Our combined results of ARPES and DFT calculations emphasize that the pairing could be of spin-singlet nature mediated by phonons in BiPd.

1.2.2 Pd based ternary chalcogenide SCs

Discovery of Pd based ternary chalcogenides, like $Nb_2Pd_{0.95}S_5$ [6,7], Nb_2PdSe_5 [8], Ta_2PdS_5 [9], $Ta_2Pd_{0.97}S_6$ [10], $Ta_2Pd_{0.97}Te_6$ [11] and $Ta_4Pd_3Te_{16}$ [12] is a recent advancement in the field of superconductivity. These layered compounds are fertile for hosting unconventional superconducting state owing to their Quasi-2-dimensional (Q2D) character [12]. The interesting compounds in this low dimensional family, are $Nb_2Pd_{0.95}S_5$ and $Nb_2Pd_{1.2}Se_5$. They are isomorphic and exhibit a T_c around 6 K. Fig.1.8 shows the crystal structure of $Nb_2Pd(Se/S)_5$ which crystallizes in a centrosymmetric structure with space group symmetry $C_{2/m}$(# 12). $Nb_2Pd_{0.95}S_5$ shows a Fermi liquid behavior at low temperatures. Sommerfiled coefficients estimated for $Nb_2Pd_{1.2}Se_5$ and $Nb_2Pd_{0.95}S_5$ i.e 15.7 and 32 mJ/mol-K^2 respectively, indicate moderately and strongly coupled electronic interactions respectively in them. Heat capacity measurements have shown signatures of multiband superconducting behavior in both the compounds which is well described by the two band-α model. On the other hand, ternary compounds such as $Ta_2Pd_{0.97}S_6$ and $Ta_2Pd_{0.97}Te_6$ belonging to the same monoclinic structure ($C_{2/m}$) like $Nb_2Pd_{0.95}S_5$, show a different behavior. These compounds share a common structure composed of chains of Pd and Nb/Ta centred polyhe-

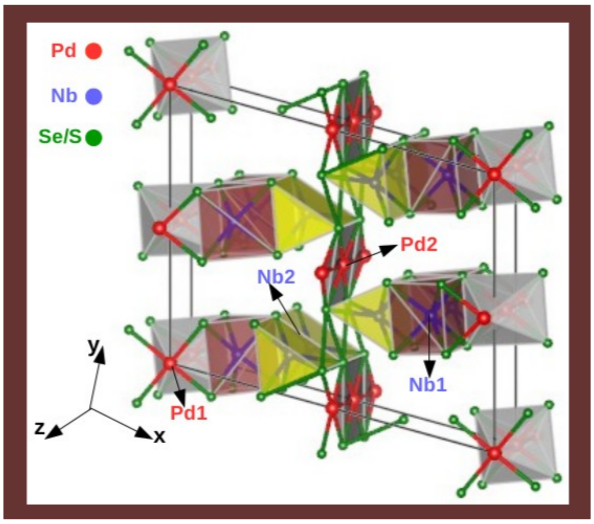

Figure 1.8: Crystal structure of $Nb_2Pd(Se/S)_5$.

dra with S/Te atoms. Changes in the structural geometry is a key factor determining the different physical behavior of these ternary SCs.

We performed a comprehensive photoemisson study on some of these ternary SCs $Nb_2Pd_{0.95}S_5$, $Nb_2Pd_{1.2}Se_5$, $Ta_2Pd_{0.97}S_6$ and $Ta_2Pd_{0.97}Te_6$ in conjugation with DFT based calculations. We observe that the VB spectra of $Nb_2Pd_{0.95}S_5$, $Nb_2Pd_{1.2}Se_5$ and $Ta_2Pd_{0.97}S_6$ are qualitatively similar except some slight differences in the energy position of various features. On the other hand, the VB spectra of $Ta_2Pd_{0.97}Te_6$ is remarkably different, particularly in the near E_f region where a clear metallic edge is observed, unlike the other compounds. Our study also shows the existence of a temperature dependent pseudogap in $Nb_2Pd_{0.95}S_5$ while the near E_f states remain unchanged with the lowering of temperature to 77 K in $Nb_2Pd_{1.2}Se_5$, $Ta_2Pd_{0.97}S_6$ and $Ta_2Pd_{0.97}Te_6$. In our calculated DOS, states crossing the E_f are dominated by different Pd-4d and Nb-4d orbitals ensuring significant role for multiband effects in $Nb_2Pd_{1.2}Se_5$ and $Nb_2Pd_{0.95}S_5$ compounds. Our comprehensive study provides a deeper insight into the VB states of these Pd based ternary compounds in correlation with their different structural geometry.

1.2.3 Fe based chalcogenide SCs

Iron based SCs, particularly members of $FeSe_{1-x}Te_x$ family have gained much attention due to their nature of strong electron correlation, unlike other SCs. Superconductivity in the $FeSe_{1-x}Te_x$ compounds was first reported by Hsu *et al.* [53] in the FeSe (x = 0) compound exhibiting a T_c $\sim$ 8 K which rises up to 37 K under pressure (7GPa) [5]. On the other hand, the other extreme composition of this family, $Fe_{1.068}Te$, though not a superconductor shows a spin density wave

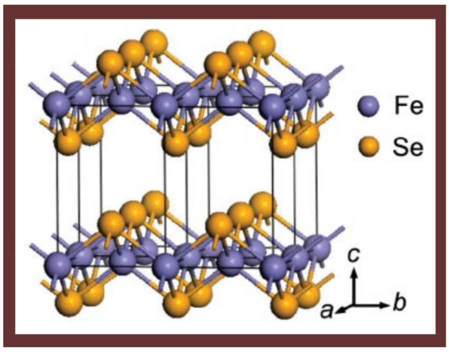

Figure 1.9: Crystal structure of FeSe.

(SDW) ordering at 67 K [6] with an accompanying structural transition from tetragonal to monoclinic. Both FeSe and FeTe have tetragonal crystal structure belonging to space group symmetry P_4/nmm as shown in Fig.1.9. It consists of a square planar sheet of Fe atoms, which is tetrahedraly coordinated with anion (Se/Te) atoms. However, the height of the anion atom from the Fe square plane is different in these two compounds and this plays a pivotal role in determining the electronic properties of these systems [11, 12].

A recent ARPES study on $FeSe_{1-x}Te_x$ compositions by Ieki *et al.* [14] has shown clearly the strong electronic correlation in these compounds. In addition, our angle integrated valence band photoemission study on $FeSe_{1-x}Te_x$ [18] revealed significant spectral weight shifts in the near E_f region with Se doping leading to the formation of a pseudogap. Further, a temperature dependent orbital selective spectral weight transfer was also observed in our study [18]. Motivated by these findings we investigated the electronic structure of FeSe and FeTe as a function of the strength of the Coulomb interaction U and intra-atomic exchange *J* based on LDA+U scheme using LMTO method. We observed multi orbital correlation effect in Fe-3d states which is more prominent in FeSe in comparison to FeTe. Our results further point out the correlations effects depend on the anion height in the family of Fe superconductors.

Bibliography

[1] M. Z. Hasan and C. L. Kane, *Rev. Mod. Phys.*, **82**, (2010), 3045.

[2] Xiao-Liang Qi and Shou-cheng Zhang, *Rev. Mod. Phys.*, **83**, (2011), 1057.

[3] von Klitzing, K., G. Dorda, and M. Pepper, *Phys. Rev. Lett.*, **45**, (1980), 494.

[4] Laughlin, R. B. *Phys. Rev. B*, **23**, (1981), 5632.

[5] Thouless, D. J., M. Kohmoto, M. P. Nightingale, and M. den Nijs, *Phys. Rev. Lett.*, **49**, (1982), 405.

[6] Bernevig, B. A., T. L. Hughes, and S. C. Zhang, *Science*, **314**, (2006), 1757.

[7] Konig, M., S. Wiedmann, C. Brune, A. Roth, H. Buhmann, L.Molenkamp, X.-L. Qi, and S.-C. Zhang, *Science*, **318**, (2007), 766.

[8] Kane C L, Mele E J. , *Phys Rev Lett.*, **95**, (2005), 146802.

[9] Fu, L., and C. L. Kane, *Phys. Rev. B*, **76**, (2007), 045302.

[10] Hsieh, D., D. Qian, L. Wray, Y. Xia, Y. S. Hor, R. J. Cava, and M. Z. Hasan, *Nature*, **452**, (2008), 970.

[11] Zhang, H., C.-X. Liu, X.-L. Qi, X. Dai, Z. Fang, and S.-C. Zhang, *Nature*, **5**, (2009), 438.

[12] Chen, Y. L., *et. al.* , *Science*, **325**, (2009), 178.

[13] Xia, Y., *et. al.* , *Nature*, **5**, (2009), 398.

[14] Zhang H J, Liu C X, Qi X L, *et. al.* , *Phys Rev B*, **80**, (2009), 085307.

[15] Feng W X, Zhu W G, Weitering H H, *et. al.*, *Phys Rev B*, **85**, (2012), 195114.

[16] Zhi Ren, A. A. Taskin, Satoshi Sasaki, Kouji Segawa, and Yoichi Ando, *Phy. Rev. B*, **82**, (2010), 241306(R).

[17] Zhi Ren, A. A. Taskin, Satoshi Sasaki, Kouji Segawa, and Yoichi Ando, *Phy. Rev. B*, **84**, (2011), 165311.

[18] Xiao D, Yao Y G, Feng W X, *et. al.* , *Phys. Rev. Lett.*, **105**, (2010), 096404.

[19] Lin H, Markiewicz R S, Wray L A, *et. al.* , *Phys. Rev. Lett.*, **105**, (2010), 036404.

[20] Wang Y J, Lin H, Das T, *et. al.*, *New J. Phys*, **13**, (2011), 085017.

[21] Y. Xia, D. Qian, D. Hsieh, L.Wray, A. Pal, H. Lin, A. Bansil, D. Grauer, Y. S. Hor, R. J. Cava and M. Z. Hasan, *Nat. Phys.*, **5**, (2009), 398.

[22] Xiao-Liang Qi, Rundong Li, Jiadong Zang, Shou-Cheng Zhang, *Science*, **323**, (2009), 1184.

[23] Liang Fu and C. L. Kane, *Phy. Rev. Lett.*, **100**, (2008), 096407.

[24] David Hsieh, Y Xia, L Wray, Dong Qian, A Pal, JH Dil, J Osterwalder, F Meier, G Bihlmayer, CL Kane, YS Hor, RJ Cava, M Zahid Hasan, *Science*, **323**, (2009), 919.

[25] J.B. Pendry and S.J. Gurman, *Surface Science*, **49**, (1975), 87.

[26] Fukui T, Hatsugai Y. , *J. Phys. Soc. Japan*, **76**, (2007), 053702.

[27] D. Hsieh, Y. Xia, D. Qian, L. Wray, J. H. Dil, M. Z. Hasan *et. al.* , *Nat. Lett.*, **460**, (2009), 1101.

[28] Liang Fu and C. L. Kane, *Phy. Rev. Lett.*, **102**, (2009), 216403.

[29] A. R. Akhmerov, Johan Nilsson, and C.W. J. Beenakker, *Phy. Rev. Lett.*, **102**, (2009), 216404.

[30] Joel Moore, *Nat. Phy.*, **5**, (2009), 378.

[31] Z.-H. Zhu, G. Levy, B. Ludbrook, A. Damascelli *et. al.*, *Phy. Rev. Lett.*, **107**, (2011), 186405.

[32] Hadj M. Benia, Chengtian Lin, Klaus Kern, and Christian R. Ast, *Phy. Rev. Lett.*, **107**, (2011), 177602.

[33] P. D. C. King, R. C. Hatch, Ph. Hofmann, *Phy. Rev. Lett.*, **107**, (2011), 096802.

[34] T. Forster, P. Kruger and M. Rohlfing, *Phy. Rev. B.*, **91**, (2015), 035313.

[35] Kunjalata Majhi, Koushik Pal, Himanshu Lohani, Abhishek Banerjee, Pramita Mishra, Anil K Yadav, R Ganesan, B R Sekhar, Umesh V Waghmare and P S Anil Kumar, *arXiv:1605.01613v1*.

[36] K. Govaerts, K. Park, C. De Beule, B. Partoens and D. Lamoen, *Phy. Rev. B.*, **90**, 155124, (2014).

[37] Bin Liu, Wuyuan Xie, Han Li, Yanrong Wang, Daoping Cai, Dandan Wang, Lingling Wang, Yuan Liu, Qiuhong Li and Taihong Wang, *Sci. Rep.*, **4**, (2014), 04639.

[38] Manfred Sigrist, *AIP Conf. Proc.*, **789**, (2005), 165.

[39] H. K. Onnes, *Comm. Phys. Lab. Univ. Leiden*, **Nos. 119**, (1911), 120.

[40] W. Meissner and R. Ochsenfeld, *Naturwiss.*, **21**, (1933), 787.

[41] H. London and F. London, **Proc. Roy. Soc. London**, **A149**, (1935), 71.

[42] J. Bardeen, L. N. Cooper and J. R. Scrieffer, *Phy. Rev.*, **108**, (1957), 1175.

[43] D. A. Ashby and Rees D. Rawlings, *J. Mater. Sci.*, **12**, (1977), 975.

[44] L.A. Pendrys, D.H. Douglass, *Solid Stat. Commu.*, **18**, (1976), 177.

[45] F. Steglich, J. Aarts, C. D. Bredl, W. Lieke, D. Meschede, W. Franz, H. Schfer, *Phy. Rev. Lett.*, **43**, (1979), 1892.

[46] W. H. Lee and R. N. Shelton, *Phys. Rev. B*, **35**, (1987), 5369(R).

[47] K. Bechgaard, K. Carneiro, M. Olsen, R B. Rasmussen, C. B. Jacobsen, *Phys. Rev. Lett.*, **46**, (1981), 852.

[48] G. Saito, H. Yamochi, T. Nakamura, T. Komatsu, M. Nakashima, H. Mori, K. Oshima, *Physica B*, **169**, (1991), 372.

[49] H. Yamauchi, M. Karppinen, *Supercond. Sci. Technol.*, **13**, (2000), R33.

[50] M. K. Wu, J. R. Ashburn, C. J. Torng, P. H. Hor, R. L. Meng, L. Gao, Z. J. Huang, Y. Q. Wang, C. W. Chu, *Phys. Rev. Lett.*, **58**, (1987), 908.

[51] Y. Kamihara, T. Watanabe, M. Hirano, H. Hosono, *J. Am. Chem. Soc.*, **130**, (2008), 3296.

[52] Rotter M, Tegel M, Schellenberg I, Hermes W, Pottgen R and Johrendt D, *Phys. Rev. B*, **78**, (2008), 020503.

[53] F.-C. Hsu, J.-Y. Luo, K.-W. Yeh, T.-K. Chen, T.-W. Huang, Yan, M.-K. Wu *et. al.*, **Proc. Natl. Acad. Sci U.S.A.**, **105**, (2008), 14262.

[54] Bhanu Joshi, A. Thamizhavel and S. Ramakrishnan, *Phys. Rev. B.*, **84**, (2011), 064518.

[55] R. Jha, B. Tiwari, P. Rani, H. Kishan and V. P. S. Awana, *J. Appl. Phys.*, **115**, (2014), 213903.

[56] A. P. Drozdov, M. I. Eremets, I. A. Troyan, V. Ksenofontov, S. I. Shylin, *Nature*, **525**, (2015), 73.

[57] A. P. Mackenzie, Y. Maeno, *Rev. Mod. Phys.*, **75**, (2000), 657.

[58] N.H. van Dijk, P. Rodire, c B. Fak, A. Huxley, J. Flouquet, *Physica B*, **319**, (2002), 220.

[59] T. Klimczuk, F. Ronning, V. Sidorov, R. J. Cava, and J. D. Thompson, *Phys. Rev. Lett.*, **99**, (2007), 257004.

[60] I. Bonalde, H. Kim, R. Prozorov, C. Rojas, P. Rogl, and E. Bauer, *Phys. Rev. B*, **84**, (2011), 134506.

[61] C. S. Lue, T. H. Su, H. F. Liu, and Ben-Li Young, *Phys. Rev. B* , **84**, (2011), 052509.

[62] Y. Huang, J. Yan, Y. Wang, L. Shan, Q. Luo, W. Wang and Hai-Hu Wen, *Supercond. Sci. Technol.*, **21**, (2008), 075011.

[63] R. Onuki, A. Sumiyama, Y. Oda, T. Yasuda, R. Settai and Y. Onuki, *J. Phys. Condens. Matter*, **21**, (2009), 075703.

[64] T. Akazawa, H. Hidaka, T. Fujiwara, T. C. Kobayashi, E. Yamamoto, Y. Haga, R. Settai, and Y. Onuki, *J. Phys. Condens. Matter*, **16**, (2004), L29.

[65] Rajveer Jha, Reena Goyal, P. Neha, V. Maurya, A. Srivastava, Anurag Gupta, S. Patnaik and V. P. S. Awana, *Sup. Sci. and Tech.*, **26**, (2016), 25008.

[66] Zhixiang Sun, Mostafa Enayat, Ana Maldonado, Calum Lithgow, Ed Yelland, Darren C. Peets, Alexander Yaresko, Andreas P. Schnyder and Peter Wahl, *Nature Comm.* , **6**, (2015), 6633.

[67] Mintu Mondal, Bhanu Joshi, Sanjeev Kumar, Anand Kamlapure, Somesh Chandra Ganguli, Arumugam Thamizhavel, Sudhansu S Mandal, Srinivasan Ramakrishnan and Pratap Raychaudhuri, *Phys. Rev. B.*, **86** , (2012), 094520.

[68] Kazuaki Matano, Satoki Maeda, Hiroki Sawaoka, Yuji Muro, Toshiro Takabatake, Bhanu Joshi, Srinivasan Ramakrishnan, Kenji Kawashima, Jun Akimitsu, Guo-qing Zheng, *J. Phys. Soc. Jpn.*, **82**, (2013), 084711.

[69] L. Jiao, J. L. Zhang, Y. Chen, Z. F. Weng,Y. M. Shao, J. Y. Feng, X. Lu, B. Joshi, A. Thamizhavel, S. Ramakrishnan, and H. Q. Yuan, *Phys. Rev. B* , **89**, (2014), 060507(R).

[70] Q. Zhang, G. Li, D. Rhodes, A. Kiswandhi, T. Besara, B. Zeng, J. Sun, Siegrist, M. D. Johannes and L. Balicas, *Scientific Reports*, **3**, (2013), 1446.

[71] Seunghyun Khim, Bumsung Lee, Ki-Young Choi1, Byung-Gu Jeon, Dong Hyun Jang, Deepak Patil, Seema Patil, Rokyeon Kim, Eun Sang Choi, Seongsu Lee, Jaejun Yu and Kee Hoon Kim, *New J. Phys.*, **15**, (2013), 123031.

[72] Y. F. Lu, T. Takayama, A. F. Bangura, Y. katsura, D. Hashizume and H. Takag, *J. Phys. Soc. Japan*, **83**, (2014), 023702.

[73] B. Tiwari, B. B. Prasad, R. Jha, D. K. Singh and V. P.S. Awana, *J. of Super. Nov. Magn.*, **27**, (2014), 2181.

[74] R. Goyal, B. Tiwari, R. Jha, and V. P.S. Awana, *J. of Super. Novel. Magn.*, **28**, (2015), 119.

[75] Wen-Hu Jiao, Zhang-T Tang, Yun-Lei Sun, Y. Liu, Q. Tao, Chun-Mu Feng, Yue-Wu Zeng, Zhu-An Xu and Guang-Han Cao, *J. of Am. Chem. Soc.*, **136**, (2014), 1284.

[76] S. Margadonna, Y. Takabayashi, Y. Ohishi, Y. Mizuguchi, *et. al.* , *Phys. Rev. B*, **80**, (2009), 064506.

[77] S. Li, C. De la Cruz, Q. Huang, Y. Chen, J. W. Lynn, J. Hu, *et. al.* , *Phys. Rev. B* , **79**, (2009), 054503.

[78] E. Z. Kuchinskii, I. A. Nekrasov, M. V. Sadovskii, *arXiv:1004.0801v1* (2010)

[79] Y. Mizugucgi, Y. Hara, K. Deguchi, S. Tsuda, T. Yamaguchi, K. Takeda, H. Kotegawa, H. Tou and Y Takano,*Sup. Sci. Tech.*, **23**, (2010), 054013.

[80] E. Ieki, K. Nakayama, Y. Miyata, T. Sato, H. Miao, N. Xu, *et. al.*, *Phys. Rev. B* , **89**, (2014), 140506(R).

[81] P. Mishra, H. Lohani, R. A. Zargar, V. P. S. Awana and B. R. Sekhar, *J. Phys. Condens Matter*, **26**, (2014), 425501.

Chapter 2

Experimental Methodology

This chapter provides a brief introduction to the basics of photoelectron spectroscopy and photoemission technique which were employed in this thesis work to investigate the electronic structure of some topological insulators (TIs) and superconductors (Scs). The present chapter is divided into two sections, the first section provides an introduction to the spectroscopy. In the second section we describe our lab based experimental set-up of photoemission.

2.1 Photoemission Spectroscopy

Photoelectron spectroscopy (PES) is one of the most important techniques contributed immensely to the understanding of electronic structure behind various exotic phenomena in physics of solids. History of photoemission begins with the famous experiment performed by Heinrich Hertz and Wilhelm Hallwachs in 1887 where they demonstrated that negative charge can be extracted from a solid when its surface is illuminated by ultraviolet light [1, 2]. Later on, in 1905 Albert Einstein described the PE process in the light of quantum formalism [3]. This field was further developed by many pioneering groups mainly, the group of Spicer [4] and Berglund [5] at Stanford, the group of Turner [6] and the group of Siegbahn at Uppsala [7]. First angular dependent band mapping came from the group of Smith, Traum and DiSalvo on the layered compounds TaS_2 and $TaSe_2$ in 1974 [8–11].

Most of the macroscopic properties manifested by materials has its origin in microscopic electron dynamics, particularly within an energy window of a few k_BT near the Fermi level. Study of those very low energy electronic states require electron energy analyzers with high resolution. This has been a long-sought goal of photoemission technique from early days. This quest resulted in mid 1990s with the advent of modern electron analyzer from Scienta which has improved energy resolution significantly from long-staggering 20-40 meV to 5 meV [12]. In addition, electron detection system has also been upgraded from one dimensional(1D) to two dimensional(2D) with angular resolution better then 0.2° and high efficiency of data acquisition [13, 14]. Recently, a vacuum ultraviolet laser based photoemission set-up has been made which has further brought down the energy resolution to $\sim$ 0.26 eV [15, 16]. These technical advancements lead to the experimental realization of many exotic properties, like Dirac fermion [1], Weyl fermion [9] etc. and established the PES as the most demanding tool in the field of condensed matter physics. Various books and excellent review articles are available in this field and we mainly adopted the work of H$\ddot{u}$fner [19], Schattke [16], Pendry [21], and Wahish [22] to prepare this section.

2.1.1 Basic principles of photoemission

The basic concept of photoemission (PE) processes is the photoelectric effect. When a photon of energy $h\nu$ impinges upon the surface of a material and the photon energy is sufficiently high, it can kickout an electron from its bound state within the material. The outgoing electron is called a photoelectron and its kinetic energy (KE) can be measured by using an electrostatic analyzer. This process is illustrated in the schematic picture of Fig.2.1(a).

The Binding Energy (BE) of the outgoing photoelectron is determined by the following relation of energy conservation

$$E_{KE} = h\nu - |E_{BE}| - W_{\phi} \tag{2.1}$$

where, E$_{KE}$ is the kinetic energy of the photoelectron, hν is the photon energy, E$_{BE}$ is the binding energy of the electron inside the solid and ϕ is the work function (the energy required for an electron at E$_F$ to just escape from the solid).

The energy level diagram of this process is presented in Fig.2.1(b).

In addition to the energy, the parallel component of momentum (K$_{||}$) of the photoexcited electron is also conserved at the solid-vacuum interface which leads to the following equation

$$\mathbf{p}_{||}/\hbar = \mathbf{K}_{||} = \mathbf{k}_{||} + \mathbf{G}_{||} \tag{2.2}$$

where, $\mathbf{p}_{||}$ is the momentum of the photoelectron in vacuum and $\mathbf{k}_{||}$ is the wave vector of the crystal state which is connected to the wave vector of photoexcited electron($K_{||}$) by appropriate reciprocal lattice vector $\mathbf{G}_{||}$ in extended Brillouin zone(BZ) scheme. On the contrary, the perpendicular component of the photoelectron does not conserve in the PE process due to symmetry breaking along the perpendicular direction to the surface.

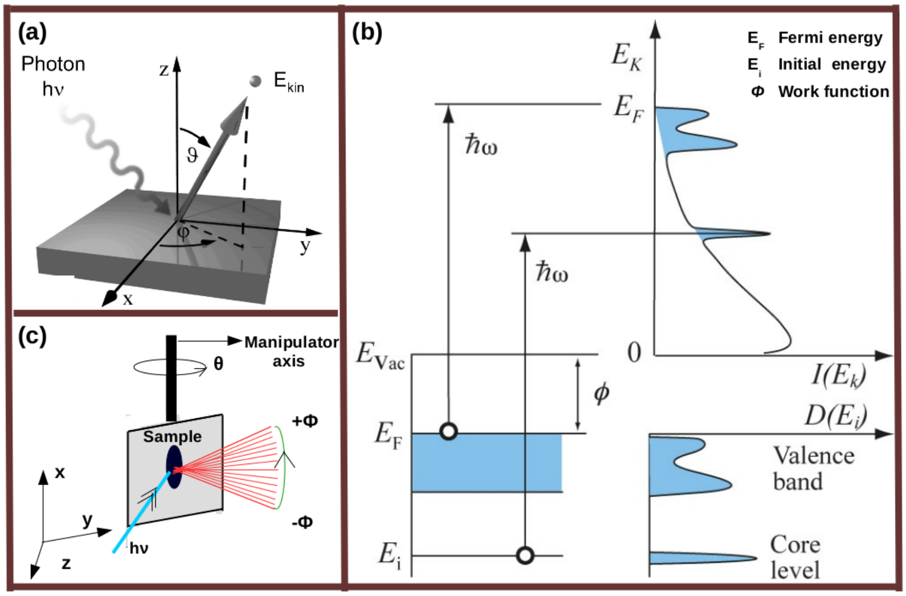

Figure 2.1: (a) A schematic picture of photoemission experiment where the characteristics of photoelectron are defined by its kinetic energy (E$_{KE}$) and momentum (**p**). The value of momentum is determined from the polar angles(θ and ϕ) of emission. (b) An intuitive representation to describe the energy level profile inside the solid and resulting photoemission spectra. (c) A rough sketch of photoelectron detection in our experimental set-up. In this geometry, photoelectron emitting in the angular range $\pm\phi$ at fix θ value which represents different values of $K_{\|}$ along the x-axis can be measured simultaneously. By varying the value of θ different parts of the Brillouin zone can be covered.

The value of K can be determined from the measured KE of the photoelectron on the basis of the free electron model.

$$K = \frac{\sqrt{2m_e E_{KE}}}{\hbar} \tag{2.3}$$

The cartesian component of K can be obtained from the polar(θ) and azimuthal(ϕ) angles of emission defined in the experimental geometry(Fig.2.1(a))

$$\begin{aligned} K_{\|_x} &= \frac{\sqrt{2m_e E_{KE}}}{\hbar} \sin\theta\cos\phi \\ K_{\|_y} &= \frac{\sqrt{2m_e E_{KE}}}{\hbar} \sin\theta\sin\phi \\ K_{\|_z} &= \frac{\sqrt{2m_e E_{KE}}}{\hbar} \cos\theta \end{aligned} \tag{2.4}$$

In Fig.2.1(c), we present a rough sketch of the geometrical configuration of photoelectron detection in our PE set-up. In this arrangement, the photoelectrons emitting at the fix θ value within certain angular range($\pm\phi$), which correspond to different values of $K_{\|}$ along the x-axis, can be measured simultaneously. Similarly, by rotating the θ at various values, y component of the $K_{\|}$ can be obtained along with different values of the $K_{\|_x}$. This exercise provides K-information of the entire BZ and immensely convenient for Fermi surface (FS) mapping. In this case, the relation between the K and angles(θ and ϕ) is given by following equation.

$$K_{\parallel} = \frac{\sqrt{2m_e E_{kin}}}{\hbar}(\hat{\mathbf{y}}.\sin\theta\cos\phi + \hat{\mathbf{x}}.\sin\phi) \tag{2.5}$$

2.1.2 Theory of photoemission

Hamiltonian of an electron in a solid under the influence of electromagnetic field (EM) is defined as

$$H = \frac{\mathbf{P}^2}{2m} + V(\mathbf{r}) - \frac{e}{2m}[\mathbf{A}(\mathbf{r}).\mathbf{p} + \mathbf{p}.\mathbf{A}(\mathbf{r})] + \frac{e^2}{2m}|\mathbf{A}(\mathbf{r})|^2 \tag{2.6}$$

The first and second term of the Hamiltonian are KE and potential energy part of the electron while rest of the terms describe the interaction between the electron and EM field(V_I) where **A**(**r**) is the vector potential of the field.

The interaction potential becomes simplified by applying the fact that the **P** and **A** commute in ultraviolet regime.

$$V_I = -\frac{e}{m}[\mathbf{A}(\mathbf{r}).\mathbf{p}] + \frac{e^2}{2m}|\mathbf{A}(\mathbf{r})|^2 \tag{2.7}$$

The value of $|\mathbf{A}|^2$ is small so this term can be neglected that is known as **linear response in the external filed** and V_I takes the following form

$$V_I = -\frac{e}{m}[\mathbf{A}(\mathbf{r}).\mathbf{p}] \tag{2.8}$$

The external field is periodic in space

$$\mathbf{A}(\mathbf{r}) = A_0.\mathbf{e}^{i\mathbf{k}.\mathbf{r}} = A_0.\hat{\mathbf{e}}(1 + i\mathbf{k}.\mathbf{r} + ...) \tag{2.9}$$

where A_0 is the complex amplitude of the field, $\hat{e}$ is a unitary vector in the direction of the light polarization and **k** is a vector pointing in the propagation direction of the field.

Using **dipole approximation** in the above expression (Eq.2.9) only the first term is retained and all the higher order terms(**k.r** $<<$ 1) are neglected. Thus, interaction further simplifies to

$$V_I = -\frac{e}{m}[\hat{\mathbf{e}}.\mathbf{p}] \tag{2.10}$$

To calculate the photocurrent from this electron-photon interaction (V_I) first order perturbation theory is utilized. There are two models to understand the full process of photoemission from the excitation to emission of the photoelectron, one is **three step model** proposed by Spicer and Berglund [5, 23–25] and the other is **one step model** [16, 21]. A pictorial comparison between both the process are depicted in Fig.2.2(a) and (b) respectively.

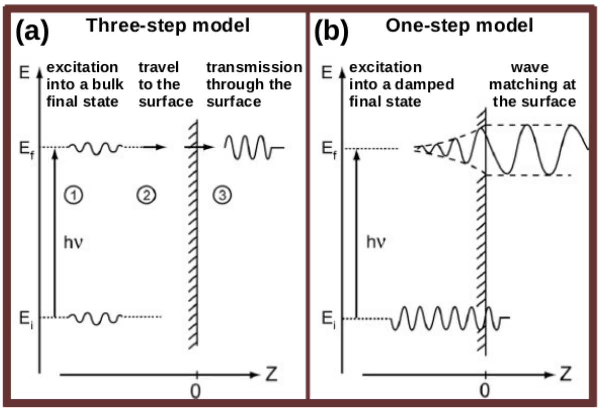

Figure 2.2: Schematics of three (a) and one (b) step model to elucidate the process of photoemission (taken from Ref. [19]).

In the three step model, PE process is considered in three independent steps; optical excitation of the electron in solid, then transport of the electron to the surface and finally escape of the electron into vacuum. The energy distribution of the photoelectrons [19] considering the interaction V$_I$ in the Fermi Golden rule under the three step model is expressed as

$$\begin{aligned} N(E, \mathbf{K}_{\|}, \hbar\omega) \propto \sum_{f,i} & |M_{f,i}(\mathbf{k}_i, \mathbf{k}_f)|^2 d(E_f, \mathbf{k}_f) |T(E_f, \mathbf{K}_{\|})|^2 \\ & \delta(E_f(\mathbf{k}_f) - E_i(\mathbf{k}_i) - \hbar\omega)\delta(E - [E_f(\mathbf{k}_f) - \phi]) \\ & \delta(\mathbf{k}_i + \mathbf{G} - \mathbf{k})\delta(\mathbf{K}_{\|} - \mathbf{p}_{\|}(\theta, \phi)/\hbar) \end{aligned} \tag{2.11}$$

where M$_{f,i}$($\mathbf{k}_i$,$\mathbf{k}_f$) is transition matrix element

$$M_{f,i} = \frac{ie\hbar}{mc} A_0 < \Psi_f | \mathbf{e}.\nabla | \Psi_i > \tag{2.12}$$

$$\Psi_f(\mathbf{k}) = \sum_{\mathbf{G}} u_f(\mathbf{k}, \mathbf{G}) e^{i(\mathbf{K}+\mathbf{G}).\mathbf{r}} \tag{2.13}$$

d(E$_f$,$\mathbf{k}_f$) is the transport coefficient describing the fraction of the total number of photoelectron created within one mean free path λ from the surface. However, the electrons which suffer from scattering in the transport that give rise to a continuous background in the PE spectra which is generally normalized or subtracted. |T(E$_f$,$\mathbf{K}_{\|}$)| is transmission factor.

$\delta(E_f(\mathbf{k}_f) - E_i(\mathbf{k}_i) - \hbar\omega)$ is delta function to ensure the energy conservation at optical excitation.

$\delta(E - [E_f(\mathbf{k}_f) - \phi])$ is a delta function imposing the condition that the KE of electron measured outside the sample is equal to its final state energy inside the sample after subtracting the work function.

$\delta(\mathbf{k}_i + \mathbf{G} - \mathbf{k})$ is a delta function to depict momentum conservation in extended zone scheme inside the crystal. Here momentum of the photon is neglected due to its relatively quite small value.

$\delta(\mathbf{K}_{\parallel} - \mathbf{p}_{\parallel}(\theta, \phi)/\hbar)$ is a delta function related to conservation of the parallel component of momentum of outside photoelectron($\mathbf{p}(\theta, \phi)$) and momentum of inside electron ($\mathbf{K}$) at the crystal surface.

As clear from the last delta function in the above photocurrent expression (Eq.2.11) a detector of small (preferably $\leq 2°$) solid angle acceptance facilitates to measure photoelectrons of a narrow k-interval range which is exclusively needed for band mapping in single crystals and known as **angle resolved photoemission measurements (ARPES)**. On the other hand, if the solid angle of detection is large then k information is smeared out due to summation over the entire outgoing wave vectors. The measurements done under this geometry are refered as **angle integrated photoemission measurements (AIPES)** and extensively used for polycrystalline samples to get information on total density of states (DOS).

Another important factor associated to the photocurrent expression (Eq.2.11) is the dependency of transition matrix element ($M_{f,i}$) on the photon energy as illustrated in Fig.2.3. This matrix element is directly proportional to the integral value between the initial state wave function and the wave function of escaping electron. It is large for low KE electron to low angular momentum of initial state and large for higher KE electron to higher angular momentum of initial state. This fact, divides photoemission measurements broadly into two parts, first is **X-ray photoelectron spectroscopy (XPS)** where photons of $\sim$ 100 eV $\leq$ 2000 eV energy range are employed which is mainly used for the core level study and elemental detection. The second technique utilizes

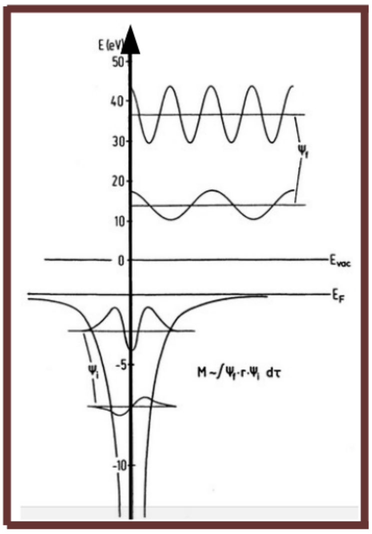

Figure 2.3: Energy level diagram to demonstrate the dependency of the matrix element($M_{f,i}$) on photon energy in the PE process. The low (high) energy final states mainly overlap with low (high) angular momentum initial states and different final states can be accessed by just varying the photon energy (taken from Ref. [19]).

photons of the lower energy range $\sim$ 4 to 100 eV and known as **ultraviolet photoemission spectroscopy (UPS)** which is quite helpful to probe the valence band (VB) region due to its large photocrosssection to the VB states. In addition many other informations, like orbital contribution from different atoms, difference between bulk and surface states can be estimated from the PE spectra by varying the photon energy.

In the PE process, besides photoelectrons all other particles are also relaxed in the photoexcitation. However, this point is missing in the three step model and more advanced treatment *i. e.* **one step model** has been proposed to account for this. In this model(Fig.2.2(b)) the scattering events in the bulk and surface is condensed into a coherent final state which is introduced into the matrix element of photo-excitation, known as time-reversal low energy electron diffraction (LEED) state. In addition, electrons interact with each other and with other particle like objects phonon, plasmon *etc.* in the system. To handle such a complicated interaction picture many body treatment is required where a system of N interacting particles is decomposed to M non-interacting quasi particles [16]. This introduces the concept of the spectral function A(ω,**k**) which is calculated by using the Green's function formalism

$$A(\mathbf{k},\omega) = -\frac{1}{\pi} ImG(\mathbf{k},\omega) \tag{2.14}$$

Green function can be written as

$$G(\mathbf{k},\omega) = \frac{1}{\omega - \epsilon_{\mathbf{k}} - \Sigma(\mathbf{k},\omega)} \tag{2.15}$$

where $\Sigma(\mathbf{k},\omega)$ is the self energy of the system and $\epsilon_{\mathbf{k}}$ is the band energy.

This many body interaction not only affects the energy of the photohole but also change its lifetime. This change of life time can be accounted by considering the self energy term to be a complex quantity.

$$\Sigma(\mathbf{k},\omega) = \Sigma^{'}(\mathbf{k},\omega) + i\Sigma^{''}(\mathbf{k},\omega) \tag{2.16}$$

and spectral function is modified to the following form

$$A(\mathbf{k},\omega) = \frac{1}{\pi} \frac{\Sigma^{''}(\mathbf{k},\omega)}{[\omega - \epsilon - \Sigma^{'}(\mathbf{k},\omega)]^2 + [\Sigma^{''}(\mathbf{k},\omega)]^2} \tag{2.17}$$

There are various methods to determine the self energy of the system from the ARPES intensity map of near Fermi region using some approximations, like particle-hole symmetry, background subtraction *etc.* [26, 27]. Therefore, ARPES measurements are quite important in the context to reveal the nature of interactions involving in the microscopic physics of solids.

2.2 Photoemisson set-up

Images in Fig.2.4 and 2.5 show the photoemission system in our laboratory consisting of two ultra high vacuum (UHV) chambers; analysis and preparation, and one small “fast entry load-lock (FEL)” chamber which is used to load the samples without affecting the UHV condition in the others. The analysis chamber (Main Chamber) is made up of mu metal to shield the photoelectrons from the magnetic field of earth and other stray sources. The sample preparation chamber is made up of stainless steel and is equipped with a four-axes manipulator, a diamond file, a sample heater and an Ar ion sputter gun. The analysis chamber accommodates the sources of energetic photons (X-ray and VUV-light), the hemispherical electron energy analyzers (SCIENTA R3000 and OMICRON AR 65) and low energy electron diffraction (LEED) unit. It is also equipped with a four axis sample manipulator-cum cryostat which can bring down the temperature to 20 K. Magnetically coupled transfer rods are used for moving the sample between the different chambers. Vacuum pumps (rotary, turbo molecular, ion and titanium sublimation) are located at different parts in the system for attaining UHV condition. Pirani and Ion gauges are used to measure the

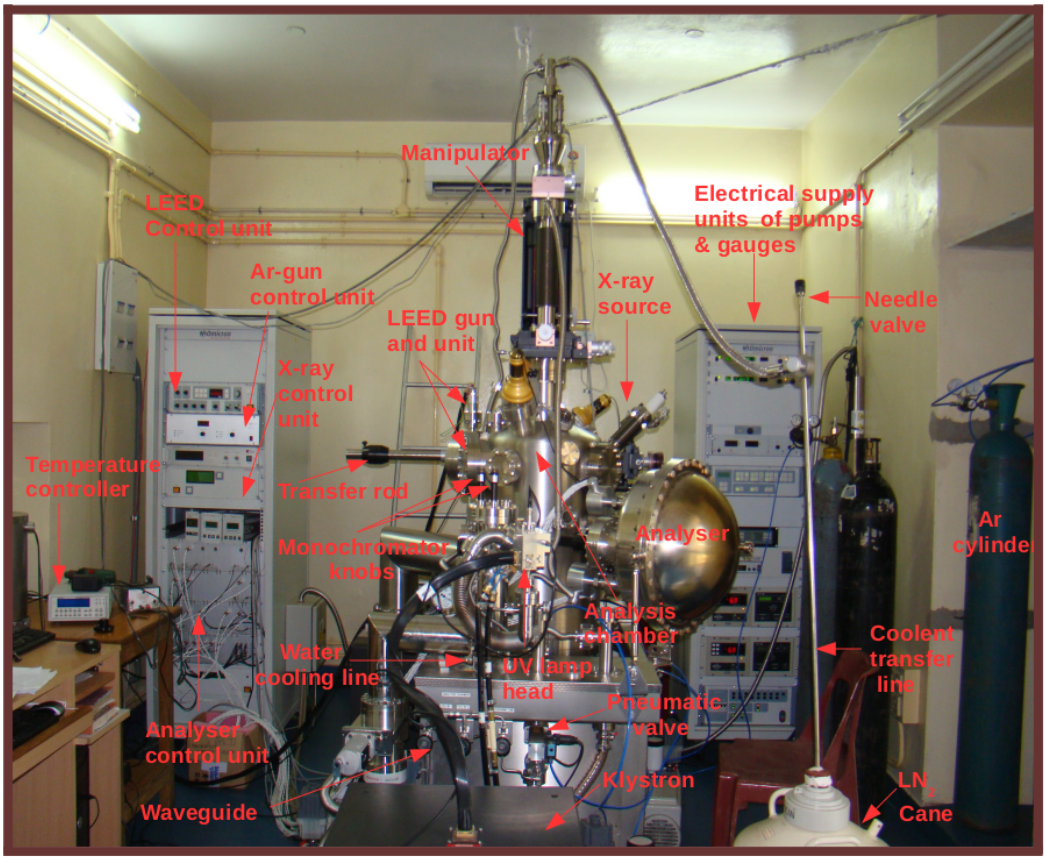

Figure 2.4: Image of photoemission system in our laboratory. Important parts of the system are labeled in the image.

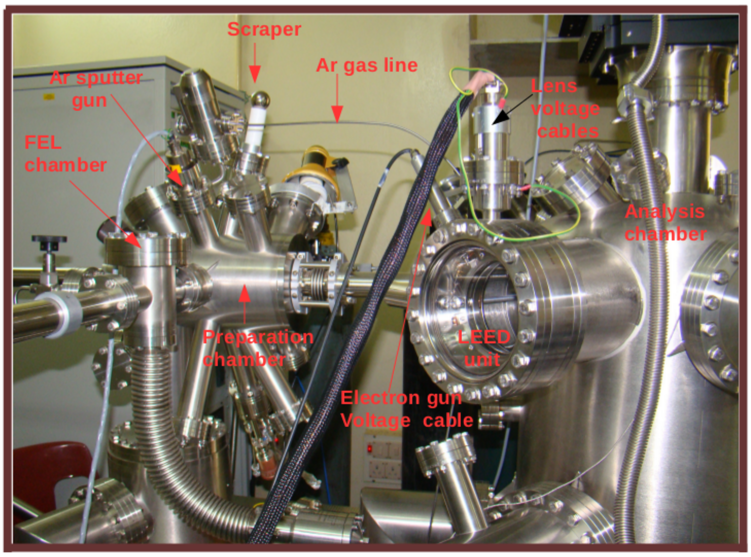

Figure 2.5: Image of the system at different angle in order to provide a clear view of the preparation chamber.

vacuum in the chambers. In the following we depict some of the important components of the system. Main sources of these information are the manuals of Scienta and Omicron.

1) Electron Lens

An electrostatic lens system is used to collect and focuses the emitted photoelectron from the sample to the entrance slit of the hemispherical analyzer. It also matches the initial kinetic energy of the electrons to the fixed pass energy of the analyzer. Inside the electrostatic lens, metal plates are held at specific potentials. The lens system can be used in two modes, **transmission** and **angular multiplexing mode**. The transmission mode is intended for large spot analysis of polycrystalline samples and special resolution in this mode is $\sim 300\ \mu$m. On the other hand, in angular multiplexing mode emission angle is imaged and used for angle resolved measurements. In this mode photoelectron emitted within the angular range $\pm\ 8^\circ$ along the longitudinal axis of the lens system are only able to reach the detector. Thus, under such geometrical arrangement, a bunch of photoemission intensity vs KE spectra for every ϕ angle between $\pm\ 8^\circ$ at a fix θ can be collected simultaneously, where θ, ϕ are polar angles along the orthogonal directions as could be seen in Fig.2.1(c). In this configuration, the data set which is constantly acquired as scanning the different θ angles along with different ϕ angles can provide a complete intensity(I(θ, ϕ, KE)) map of the FS as described in the previous section(Eq.2.5).

2) Hemispherical Analyzer

After exiting the lens, the electrons enter into the hemispherical analyzer. It consists of two metal hemispheres which are placed in such an order that their centre of curvature coincides to the same

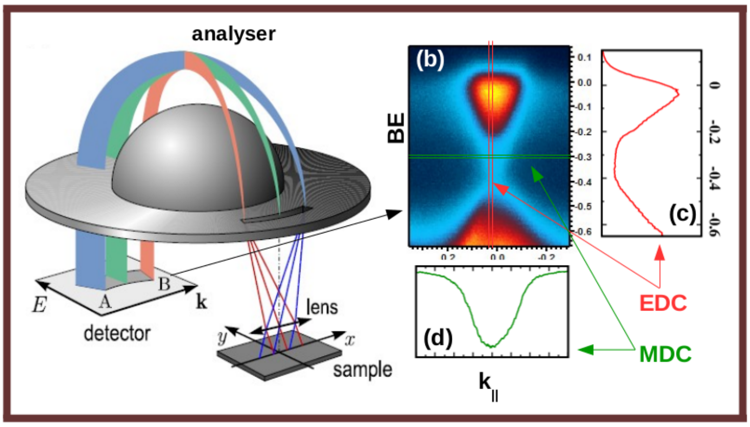

Figure 2.6: (a) Image shows the working principle of modern electron spectrometer of Scienta. Photoelectrons emanating from the sample in a certain angular range can be collected from the lens system which pass through the analyzer and then detected by the multi channel multiplier and simultaneously a 2D intensity image of energy vs momentum is obtained from the CCD camera. (b) Example of the intensity plot where the vertical and horizontal scales correspond to binding energy (BE) and parallel component of the momentum of photoelectrons and cuts (red and green) along the same directions are used to extract energy density curves (EDC) (c) and momentum density curves (MDC) (d) respectively.

point. Both the hemispheres are put at different voltages that results an electric field between the two. As the electrons enter the sphere they undergo different circular path depending on their KE. The higher KE electrons collide to the outer sphere whereas lower KE electrons end up to the inner sphere. Therefore, electrons in a small energy window are able to pass to the other end of hemisphere successfully. This energy window is defined as **pass energy** and is determined by following formula

$$E_P = \frac{eV}{R_2/R_1 - R_1/R_2} \tag{2.18}$$

where R_1 and R_2 are the radii of the hemispheres and V is the voltage applied between them.

The energy resolution of the concentric hemispherical analyzer is calculated as [28]

$$\Delta E = E_P(\frac{x_1 + x_2}{2R_0} + \alpha^2) \tag{2.19}$$

where x_1 and x_2 are the width of entrance and exit apertures respectively. α is the angular acceptance of electron beam at the entrance slit. R_0 is the mean radius of the hemispherical analyzer.

In the present thesis work photoemission data were collected by SCIENTA R3000 hemispherical analyzer with a mean radius of 135 mm and angular coverage range of ± 8°. The entrance slit width of the hemispherical analyzer can be adjusted to any of the six slit apertures, 0.2 (straight), 0.2 (curved), 0.4 (curved), 0.8 (curved), 1.3 (straight), 3.0 (straight).

3) Multi Channel Detector After passing through the lens and analyzer electrons encounter a two dimensional (2D) multi channel detector. The detector is built using electron multi channel plates (MCP) coupled to a phosphorous screen in front of a charge coupled device (CCD) camera consisting 600 simultaneous energy channels and 400 angular channels. The role of the multiplier plate is to amplify incident electrons to million times through secondary emission. Thus, each individual electron coming through the analyzer becomes a packet of electrons in a given energy/momentum bin on the other end side of the MCP which hits the phosphorus screen creating a flash of light. This flash is then detected by the Firewire CCD camera and thus, a 2D intensity image is obtained. The whole journey of the photoelectrons starting from the lens system to the detection by MCP/CCD are schematically picturised in the Fig.2.6(a). An illustration of 2D intensity image plot is also shown in Fig.2.6(b) while Fig.2.6(c) and (d) depict the energy density curve (EDC) and momentum density curve (MDC) extracted from the cuts (red and green) along the binding energy and momentum axis of this image plot

4) Photon Sources

Two photon sources are attached to the system; first ultra violet (UV) source (SCIENTA VUV 5k) and second X-ray source (Omicron DAR 400). For the work covered in this thesis I have used the first one and its details are as follows.

(i) UV Lamp

The SCIENTA VUV 5k is a high intensity monochromatized VUV (vacuum ultra violet) radiation source. The VUV radiation originates from radiative transitions in the Helium plasma excited by electron impact using the electron cyclotron resonance (ECR) technique. Discharge occurs in the discharge cavity inside the lamp head of VUV 5050, in a magnetic field tuned to the microwave frequency, generated from a microwave generator VUV 5011, to meet the ECR conditions.

The microwave (RF) generator mainly consists of a 10 mW dielectric resonator oscillator (DRO) and a four cavity klystron amplifier (Varian VKX 7913). Klystron amplifies the radio frequency signal by converting the kinetic energy in a DC electron beam into radio frequency power. This RF power is then transported via a ferrite circulator to the output waveguide. When the high voltage is switched on, the RF energy goes to the cavity and is reflected back to the circulator, which redistributes it into a high power dummy load. A small part of this reflected power is detected and subsequently compared to a reference voltage. If the level is above 20%, 12 V DC is fed out to the spark generator at the lamp head. This generates 25 kV pulses that discharge inside one of the hollow magnet pole pieces to ignite the plasma. As soon as the discharge starts, the reflection disappears and the high voltage pulses cease. The oscillating RF electric field then reaches the transformer located inside the lamp head via waveguide. The transformer is an impedance matching structure between the rectangular waveguide and a pair of transmission lines composed

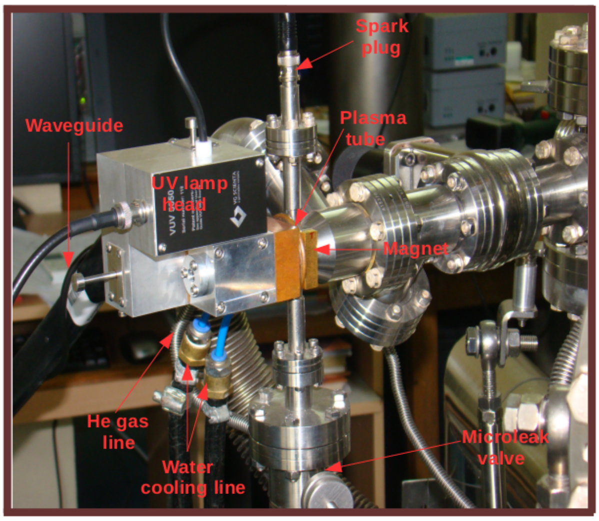

Figure 2.7: Picture of the UV lamp head attached to the system where individual parts are marked for clarity.

of Tantalum. The electric field then reaches the plasma cavity where it causes Helium discharge by ECR phenomena in the presence of an inhomogeneous magnetic field created by the magnets coupled externally to the plasma tube as could be seen in Fig.2.7. An oscillating electric field with its electric field vector perpendicular to the magnetic field vector results in acceleration of the particles, like in a cyclotron. In comparison to the standard method of creating a discharge by application of DC voltage between two electrodes, ECR has added advantages. Firstly, the plasma is achieved in a small volume due to efficient acceleration. Secondly, ECR plasma requires much lower gas pressure. The VUV source can be operated with various discharge gases, like Helium, Neon, Argon, Krypton, Xenon or Hydrogen. In the Helium discharge process photons of characteristic energy are emitted originating from two groups of radiative transition. The first one belongs to the decay of excited neutral helium atoms and the second one originates from the decay of singly ionized helium atoms. The strongest lines occur at 21.22 eV and 40.81 eV for He-I and He-II respectively.

The He I and He II lines are separated by means of VUV5040 monochromator. It consists of a toroidal grating that selects and refocuses the chosen wavelength generated from the UV source via the adjustment of outer and central knobs. The VUV flux density is $\sim$ 1.5 $\times$ 10^{16} photons/sr second with a beam diameter of 2 mm. Two stages of differential pumping are employed to maintain the chamber in UHV while providing a stable pressure in the lamp. At the first stage, the discharge region is pumped down to a pressure of $\sim 10^{-2}$ mbar using a rotary pump, whereas for the second stage, a turbomolecular pump is employed to further reduce the He gas pressure before the main vacuum chamber.

3) Low energy electron diffraction (LEED)

In order to determine the orientation of a crystalline surface the LEED unit is used. A schematic of this set-up is displayed in Fig.2.8. The main elements in the LEED unit are an electron gun and a detection system. The cathode element in the electron gun is made of thoriated tungsten which is negatively biased with respect to the sample. Electrons emitted from this cathode via thermionic emission are accelerated and focused into a beam using a set of electron lenses. The electrons incident normally on the surface are backscattered elastically and diffraction pattern is seen on the screen in case of single crystalline well ordered surface otherwise a diffused circular pattern appears on the screen in case of polycrystals. LEED detection system consists of four hemispherical concentric grids and a phosphor screen. The grids serve the purpose of screening out the inelastically scattered electrons. The first grid is grounded to shield the sample from the high electric fields from the luminescent screen. The second grid, the suppressor, is set to a voltage just below the acceleration voltage of the incident electrons to remove inelastically scattered electrons from the diffracted beam. The last grid is grounded to shield the suppressor from the high voltage on the luminescent screen. After passage through the last grid the elastically scattered electrons are accelerated towards the screen by the screen voltage.

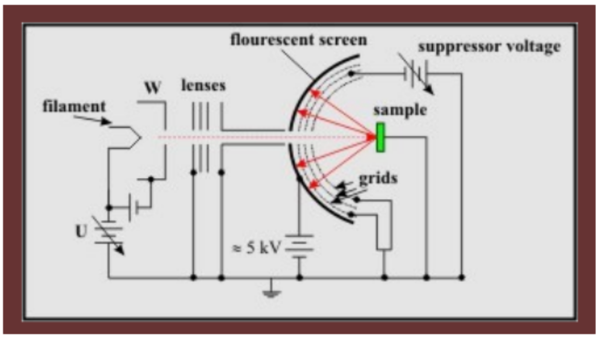

Figure 2.8: A simplified presentation to illustrate the low energy electron diffraction (LEED) system.

2.3 Experimental Operation

Need of ultra high vacuum (UHV) condition

First we explain why UHV condition is essential to perform PE experiments. It can be understand from Fig.2.9 which describes the “universal curve” electron escape depth(λ) as a function of the KE of electron for different metals. This curve shows that the escape depth is only few angstrom for the KE range between 10 to 2000 eV which is mostly concerned in the PE experiments.

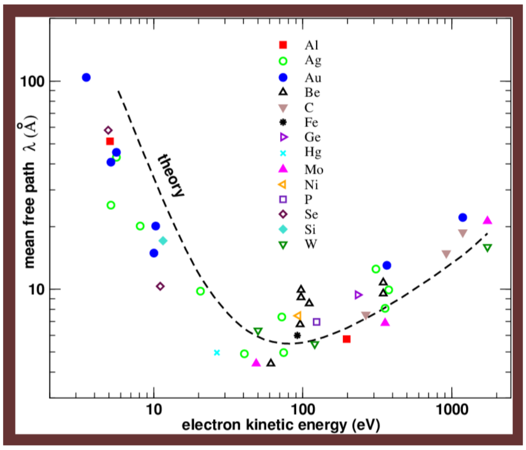

Figure 2.9: Plot of an universal curve describing electron escape depth(λ) as a function of the KE of electron for various metals.

Therefore, an atomically clean surface which truly represents the bulk is required for a meaningful PE study. The UHV condition is needed to prevents such a clean surface from the contamination of residual gases for a time scale enough to perform the experiments.

Procedure of the experiment

Sample is pasted on a standard stainless steel(SS) plate with the use of UHV compatible glue and painted silver paste all around it to make it conducting. The sample plate is first loaded in the FEL chamber for 2-3 hr. pumping before transfer it to preparation chamber. In the preparation chamber polycrystalline samples are scrapped by diamond file to make a fresh surface and this process is repeated in many times until contamination feature occur $\sim$ E_b = -9.5 eV is completely disappeared in PE spectra. We use Ar sputter gun to clean the polycrystalline film of Ag sample and it is used for the Fermi energy calibration. On the other hand, to get a fresh surface in case of single crystal samples standard post cleaving technique is used where small nail glued on the sample is removed by a strong hit using the scraper inside the preparation chamber. After preparing the clean surface, the sample is moved to analysis chamber from the preparation chamber with help of magnetically coupled transferring rod. In analysis chamber, sample position is optimized to receive the maximum exposure of the incident photo light by manipulating x, y, z and θ degree of freedoms of the manipulator. In case of single crystal samples crystal orientation is checked using LEED detection before performing the ARPES measurements. A microleak valve is used to regulate the pressure of He gas to switch on the UV lamp and maintain it to least($\sim$ 0.1 - 0.2 %) reflection condition. Similarly, by adjusting the monochromator knob photon energy can be sweeped between different He excitation energies. In present work, we mainly used He-I(21.2 eV) and He-II(40.8 eV) photon energy. For low temperature measurements liquid N_2 is used to cool down the sample to 77 K by a cryostat. The temperature of the sample is measured by using a Si diode on the back of the sample plate. A small heater is also attached at the manipulator tip. A feedback system (LackShore 331 temperature controller) where the temperature of the sample controls the current through the filament, allows a constant temperature to be set. To collect the spectra commands are set from VG-Scienta software (SES 1.26-r$_{6/7}$), from where pass energy, step size, lens modes, dwel time *etc.* parameters can be fine-tuned by the command panel window. In the preset work lens mode transmission and A20 were opted for angle integrated and angle resolved measurements respectively. The pass energy = to 5 meV and step size = 10/5 meV were selected for the spectra of full/short energy scans at He-I source energy while the pass energy = 10 meV and step size 20/10 meV were set for the spectra of full/short energy scans at He-II energy. In the experiments related to band bending in TIs, different gases (N_2, O_2 and Ar) were filled in the preparation chamber $\sim 3.5 \times 10^{-5}$ mbar pressure and through controlling of manual valve these gases were allowed to pass in the analysis chamber to create a partial pressure $\sim 4 \times 10^{-9}$ mbar.

Bibliography

[1] H. Hertz, *Ann. Phys.*, **31**, (1887), 983.

[2] W. Hallwachs, *Ann. Phys.*, **33**, (1888) 301.

[3] A. Einstein, *Ann. Phys.*, **31**, (1905), 132.

[4] W. E. Spicer, and C. N. Berglund, *Phys. Rev. Lett.*, **12**, (1964), 9.

[5] C. N. Berglund and W. E Spicer, *Phys. Rev.*, **136**, (1964), A1044.

[6] D. W. Turner, C. Baker, A. D. Baker, and C. R. Brundle, Molecular Photoelectron Spectroscopy (London: Wiley-Interscience) (1970).

[7] C. Nordling, E. Sokolowski, and K. Seigbahn, *Phys. Rev.*, **105**, (1957), 1676.

[8] N. V. Smith, and L. F. Mattheiss, *Phys. Rev. B*, **9**, (1974), 1341.

[9] N. V. Smith, *Phys. Rev. B*, **9**, (1974), 1365.

[10] N. V. Smith, M. M. Traum, and F. J. DiSalvo, *Solid State Comm.*, **15**, (1974), 211.

[11] M. M. Traum, N. V. Smith, and F. J. DiSalvo, *Phys. Rev. Lett.*, **32**, (1974), 1241.

[12] VG Scienta **http://www.vacgen.com** and SPECS GmbH **http://www.specs.de**.

[13] Aebi, J. Osterwalder, P. Schwaller, L. Schlapbach, M. Shimoda, T. Mochiku, and K. Kadowaki, *Phys. Rev. Lett.*, **72**, (1994), 2757.

[14] T. Valla, A. V. Fedorov, P. D. Johnson, B. O. Wells, S. L. Hulbert, Q. Li, G. D. Gu, and N. Koshizuka, *Science*, **285**, (1999), 2110.

[15] T. Kiss, F. Kanetaka, T. Yokoya, T. Shimojima, K. Kanai, S. Shin, Y. Onuki, T. Togashi, C. Zhang, C. T. Chen, and S. Watanabe, *Phys. Rev. Lett.*, **94**, (2005), 057001.

[16] Guodong Liu, Guiling Wang, Yong Zhu, Hongbo Zhang, Guochun Zhang *et. al. Rev. Sci. Instrum.*, **79**, (2008), 023105.

[17] M. Z. Hasan and C. L. Kane, *Rev. Mod. Phys.*, **82**, (2010), 3045.

[18] Su-Yang Xu, Ilya Belopolski, Nasser Alidoust, Madhab Neupane, Guang Bian, Chenglong Zhang, Raman Sankar, Guoqing Chang, Zhujun Yuan, Chi-Cheng Lee, Shin-Ming Huang, Hao Zheng, Jie Ma, Daniel S. Sanchez, BaoKai Wang, Arun Bansil, Fangcheng Chou, Pavel P. Shibayev, Hsin Lin, Shuang Jia, M. Zahid Hasan, *Science*, **349**, (2015), 613.

[19] Stefan H$\ddot{u}$fner, Photoelectron Spectroscopy: Principles and Applications, **Springer**, (1996).

[20] Wolfgang Schattke (Editor) and Michel A. Van Hove (Editor), Solid-State Photoemission and Related Methods: Theory and Experiment, **Wiley VCH**, (2003).

[21] J.B. Pendry, Theory of photoemission, *Surface Science*, **57**, (1976), 679.

[22] Amal al-Wahish, introduction to photoemission and application to layered oxides Ph.D thesis work (2009).

[23] H. Y. Fan, *Phys. Rev.*, **68**, (1945), 43.

[24] H. Mayer, and H. Thomas, *Z. Phys.*, **147**, (1957), 419.

[25] H. Puff, *Phys. Stat. Sol.*, **1**, (1961), 636.

[26] M. R. Norman, H. Ding, H. Fretwell, M. Randeria and C. Campuzano, *Phys. Rev. B*, **60**, (1999), 7585.

[27] A. A. Kordyuk, S. V. Borisenko, A. Koitzsch, J. Fink, M. Knupfer, and H. Berger, *Phys. Rev. B*, **71**, (2005), 214513.

[28] H. Luth, Solid Surfaces, Interafces, and Thin Films, Springer, 4th edition (2001).

Chapter 3

Details of Calculations

This chapter briefly describes the details of first principles or *ab initio* methods of electronic structure calculations. The basic motive to perform such calculations is to get a deeper insight on our photoemission results. The term “First principles” refers that only basic structural informations are required to determine the electronic properties of the system without any need of tuneable parameters. This method simplifies a complicated many electron problem to a problem of many independently moving electrons in an effective mean field by applying some fundamental approximations which is solved under the frame work of density functional theory(DFT). This is discussed in the first section and second section is on the fundamentals of the band structure calculation methods based on DFT formulation.

3.1 Density Functional Theory

Over the past few years **density functional theory(DFT)** has emerged as the most successful and enormously employed methodology to describe the properties of condensed matter systems covering a broad range from conventional bulk materials to complex materials, like interface, molecules and very recently proteins and nano materials. Initially, in 1927 **Thomas** [1] and **Fermi** [2] conceptualized an idea that density of electrons can be used as the basic variable instead of electron wavefunctions to solve a many electron problem. However, they missed electronic exchange and correlation part in their scheme which was later on in 1930 introduced by **Dirac** [3]. Though this approach of Thomas-Fermi-Dirac severely failed to describe many of the electronic properties but it paved way for the foundation of DFT laid by **Hohenberg** and **Kohn** [4] in 1964. According to their scheme, all properties of a system can be described to be unique functionals of its ground state density and using some approximations, it can be practically feasible to calculate the electronic properties of materials through DFT formulation. In the following, we describe the very basic features of this remarkable theory.

Born-Oppenheimer approximation

The Hamiltonian of a many body condensed matter system consisting nuclei and electron is

$$\begin{aligned} H_{Tot} = -\sum_{i=1}^{N}\Big(-\frac{\hbar^2}{2M_I}\nabla^2_{R_I} - \frac{\hbar^2}{2m_e}\nabla^2_{r_i} + \frac{1}{2}\sum_{I,J;I\neq J}\frac{Z_I Z_J e^2}{|\mathbf{R_I}-\mathbf{R_J}|} + \frac{1}{2}\sum_{i,j;i\neq j}\frac{e^2}{|\mathbf{r_i}-\mathbf{r_j}|} \\ + \sum_{I,i}\frac{Z_I e^2}{|\mathbf{R_I}-\mathbf{r_i}|}\Big) \end{aligned} \tag{3.1}$$

where the indexes I and J run on nuclei, i and j on electrons. $\mathbf{R}_I$ and M_I are positions and masses of the nuclei, $\mathbf{r}_i$ and m_e of the electrons, Z_I the atomic number of nucleus I. The first and second terms correspond to kinetic energy(KE) of the nuclei and electrons respectively. The third and fourth terms are the potential energy of nucleus-nucleus and electron-electron Coulomb interaction respectively. The last term is the potential energy originating from nucleus-electron Coulomb interaction.

To solve this equation of interacting many particles is a cumbersome task. In 1927, **Born** and **Oppenheimer** [5] proposed that at each instant the electronic system can be considered in the ground state of each instantaneous ionic configuration due to much heavier atomic masses of the nuclei drastically reduce their movement in comparison to electrons. This allows to separate out the movement of electrons and nuclei. And the system can be considered to be one with electrons moving in a static external potential(V_{ext}) exerted by the nuclei. This approximation is also named as "**adiabatic approximation**". Thus, in the above Hamiltonian(Eq.3.1) only electronic terms survive. Shr*ö*dinger equation for this Hamiltonian is given by

$$H\Psi = E\Psi \tag{3.2}$$

where Ψ is the many electron wavefunction and E is the energy of the electronic system in the external potential.

Hohenberg and **Kohn** [4] formulated two basic theorems of the DFT for a system of N interacting electrons with a non degenerate ground state.

1) The ground state electronic density n($\mathbf{r}$) of an interacting particle system uniquely determines the external potential $V_{ext}(\mathbf{r})$ with an additional constant.

2) The total energy of the system is minimized by the ground state electron density.

The first theorem simplifies the N electron problem to the determination of a three variable function (n(**r**)) and the second theorem ensures the calculation of ground state density via minimization of the energy functional.

The total energy of the interacting electronic system in an external potential V_{ext} is written as

$$E[n] = \int V_{ext}(\mathbf{r})n(\mathbf{r})d\mathbf{r} + F[n] \tag{3.3}$$

where F[n] = T[n] + V_{ee} corresponds to a functional of the ground state density. T[n] and V_{ee} represent the KE factor and electron-electron Coulomb interaction terms respectively.

The energy functional E[n] can be minimized with the constraint

$$\int n(\mathbf{r})d\mathbf{r} = N \tag{3.4}$$

where N being the total number of electrons.

However, the exact form of F[n] is unknown which restricts further proceeding in the calculation. **Kohn and Sham(KS)** [6] overcame this problem by defining a virtual system of non interacting electrons which has the same ground state density like the original interacting system. The functional F[n] and E[n] of this virtual system are the following

$$F[n] = T_0[n] \tag{3.5}$$

$$E[n] = \int V_{eff}(\mathbf{r})n(\mathbf{r})d\mathbf{r} + F[n] \tag{3.6}$$

Now, the original functional F[n] of the interacting system can be expressed in terms of the total KE of the non interacting system and an electron electron interaction part.

$$F[n] = T_0[n] + \int \frac{n(\mathbf{r})n(\mathbf{r}^{'})}{|\mathbf{r}-\mathbf{r}^{'}|}d(\mathbf{r})d(\mathbf{r}^{'}) + E_{xc}[n] \tag{3.7}$$

where E_{xc}[n] defines the **exchange correlation(XC)** which includes the many electron interactions. The second term belongs to the **Hartree part(V$_H$)**. Using this modified functional F[n] the energy functional of interacting system becomes

$$\begin{aligned} E[n] &= F[n] + \int V_{ext}(\mathbf{r})n(\mathbf{r})d\mathbf{r} \\ &= T_0[n] + \int n(\mathbf{r})[V_{ext}(\mathbf{r}) + V_H(\mathbf{r})]d(\mathbf{r}) + E_{xc}[n] \end{aligned} \tag{3.8}$$

Minimizing this total energy functional with respect to the density provides

$$\frac{\delta E[n]}{\delta n(\mathbf{r})} = \frac{\delta T_0[n]}{\delta n(\mathbf{r})} + V_{ext}(\mathbf{r}) + V_H(\mathbf{r}) + \frac{\delta E_{xc}[n]}{\delta n(\mathbf{r})} - \mu \tag{3.9}$$

where μ is a **Lagrange multiplier** which ensures the conservation of total number of electrons in the system.

Applying the same procedure of variational principle to the non interacting system(Eq.3.6) gives

$$\frac{\delta E[n]}{\delta n(\mathbf{r})} = \frac{\delta T_0[n]}{\delta n(\mathbf{r})} + V_{eff}(\mathbf{r}) = \mu \tag{3.10}$$

comparison between the Eq.3.9 and Eq.3.10 gives rise to the following relation

$$V_{eff} = V_{ext}(\mathbf{r}) + V_H(\mathbf{r}) + V_{xc}(\mathbf{r}) \tag{3.11}$$

where the XC potential is defined as

$$V_{xc}(\mathbf{r}) = \frac{\delta E_{xc}[n]}{\delta n(\mathbf{r})} \tag{3.12}$$

Now by solving the single particle Kohn-Sham equations

$$H_{KS}\Psi_i(\mathbf{r}) = \Big[- \Delta_i + V_{eff}(\mathbf{r})\Big]\Psi_i(\mathbf{r}) = \epsilon_i \Psi_i(\mathbf{r}) \tag{3.13}$$

of the virtual system the single particle density of the interacting system can be determined

$$n(\mathbf{r}) = \sum_{i=1}^{Occ.} |\Psi_i(\mathbf{r})|^2 \tag{3.14}$$

This is a significant reduction to the many electron problem. In the next step, the Kohn-Sham equations are solved self consistently and finally, the ground state total energy E[n] of the electronic system can be obtained by using the converged density as follows

$$E = \sum_{i=1}^{Occ.} \epsilon_i - \iint \frac{n(\mathbf{r})n(\mathbf{r}')}{|\mathbf{r} - \mathbf{r}'|}\, d\mathbf{r}\, d\mathbf{r}' - \int n(\mathbf{r})V_{xc}(\mathbf{r})d\mathbf{r} + E_{xc}[n] \tag{3.15}$$

where the last three factors are incorporated to correct the double counting in the sum of the eigenvalues. In this expression, except XC part the other KE and electrostatic parts are known in the exact forms. Thus, this XC part can be approximated in such a manner to get a satisfactory description of a realistic condensed matter systems. The most widely accepted approximations are **local density approximation(LDA)** and **generalized gradient approximation(GGA)**.

Description of local density approximation(LDA)

The XC energy in the LDA approximation [7] is given by

$$E_{xc}^{LDA}[n] = \int n(\mathbf{r})\epsilon_{xc}[n(\mathbf{r})]d\mathbf{r} \tag{3.16}$$

where $\epsilon_{xc}[n]$ is the exchange correlation energy per particle of a homogeneous gas of interacting electron density n(**r**). This approximation can be further generalized to spin polarized systems as a **local spin density approximation(LSDA)** [8,9]

$$\begin{aligned} &E_{xc}^{LSDA}[n\uparrow, n\downarrow] = \int n(\mathbf{r})\epsilon_{xc}\Big[n\uparrow(\mathbf{r}), n\downarrow(\mathbf{r})\Big]d\mathbf{r} \\ &n = n\uparrow + n\downarrow \end{aligned} \tag{3.17}$$

where ϵ_{xc}[n(**r**)] is the XC energy per electron of a uniform electron system of density n(**r**). n↑ and n↓ refer to the charge density of the ↑ and ↓ spin electrons respectively.

Under this approximation it is assumed that the charge density n(**r**) varies smoothly with respect to **r**. However, in strongly correlated systems, like transition metal oxides which has partially filled d and f orbitals, LSDA based results markedly deviate from the experimental findings.

Description of generalized gradient approximation(GGA)

The **GGA** approximation [10, 11] has emerged as one of the most promising attempts to remedy the deficiencies of the LDA approximated XC energy. In this approximation the XC functional not only depends on the electron density, like LDA but also on the first gradient $|\nabla_n|$ of the electron density. This inclusion of $|\nabla_n|$ introduces a few non locality to the previous LDA functional as well as removes some of the self interaction present in the LDA.

Description of LDA+U

The discussed above L(S)DA and GGA derived XC potential are orbital independent so they can not adequately address the properties of systems associated with localized d and f shells. To deal with the electronic correlation in d and f orbitals various methods have been introduced, like **self interaction corrections(SIC)** [12], **Hartree-Fock(HF)** [13], **GW approximation** [14] and **LDA+U** [15]. We employed LDA+U method to study the correlation effects in Fe-3d orbitals in Fe-chalcogenide superconductors. In the following we describe the essence of this method.

In **LDA+U** scheme delocalized s and p electrons are treated by LDA/GGA approximation whereas localized d and f electrons described by orbital dependent potential

$$\frac{1}{2}U\sum_{i\neq j} n_i n_j \tag{3.18}$$

where n$_i$ and n$_j$ are the d or f orbital occupancies.

The total energy in L(S)DA+U methods is given by

$$E_{Tot}^{LDA+U}[\rho_\sigma(\mathbf{r}), \{n_\sigma\}] = E^{LSDA}[\rho_\sigma(\mathbf{r})] + E^U[\{n_\sigma\}] - E_{dc}[\{n_\sigma\}] \tag{3.19}$$

where σ is the spin index, $\rho_\sigma(\mathbf{r})$ represents the electronic density for spin σ electrons and $n\{\sigma\}$ denotes the density matrix of d or f electrons for spin σ. The first term corresponds to the usual LSDA energy functional while second term describes the electron - electron Coulomb interaction energy which is written as

$$\begin{aligned} E^U[\{n\}] = \frac{1}{2}\sum_{\{m\},\sigma} \{ &< m, m^{''}|V_{ee}|m^{'}, m^{'''} > n_{m,m^{'},\sigma} n_{m^{''},m^{'''},-\sigma} \\ &- (< m, m^{''}|V_{ee}|m^{'}, m^{'''} > - < m, m^{''}|V_{ee}|m^{'''}, m^{'} >) n_{m,m^{'},\sigma} n_{m^{''},m^{'''},\sigma} \} \end{aligned} \tag{3.20}$$

where m is the magnetic quantum number and V_{ee} is the screened Coulomb interactions among the d or f electrons. The final term accounts for the double counting which is needed to separate out an averaged LDA energy contribution of these d or f electrons from the LDA energy and defined as

$$\begin{aligned} &E_{dc}[\{n_\sigma\}] = \frac{1}{2}UN(N-1) - \frac{1}{2}J[N\uparrow(N_\uparrow - 1) + N\downarrow(N_\downarrow - 1)] \\ &N = N_\uparrow + N_\downarrow \end{aligned} \tag{3.21}$$

where Nσ = Tr(n$_{m,m'}$, σ) and U and J are the screened Coulomb and exchange parameters respectively.

The matrix elements of V_{ee} can also be defined in terms of spherical harmonics and effective Slater integrals F_k [16] as following

$$< m, m^{''}|V_{ee}|m^{'}, m^{'''} > = \sum_k a_k(m, m^{'}, m^{''}, m^{'''}) F_k \tag{3.22}$$

where k value lies within $0 \leq k \leq 2l$

$$a_k(m, m^{'}, m^{''}, m^{'''}) = \frac{4\pi}{2k+1}\sum_{q=-k}^{k} < lm|Y_{kq}|lm^{'} >< lm^{''}|Y_{kq}^*|lm^{'''} > \tag{3.23}$$

$$F_k \approx \iint_0^\infty (r_1 R_i(r_1))^2 (r_2 R_i(r_2))^2 \frac{r_<^k}{r_>^{k+1}}\, dr_1\, dr_2 \quad \text{for } k > 0 \tag{3.24}$$

In this $r_<$ and $r_>$ denote the radius which are smaller and larger than r_1 and r_2 respectively. The screened Coulomb and exchange parameters U and J can be redefined in terms of this Slater integrals as follows

$$\begin{aligned} &U = F_0; J = (F_2 + F_4)/14 && \text{for 3d and 4d systems} \\ &U = F_0; J = (286F_2 + 195F_4 + 250F_6)/6435 && \text{for 4f and 5f systems} \end{aligned} \tag{3.25}$$

The screened Coulomb parameter can be calculated from the constraint LDA method [17] while relation F_4/F_2 and F_6/F_2 are taken from atomic calculations. Therefore, absence of any adjustable parameters makes LDA+U recipe to an *ab initio* method.

3.2 Methods of band structure calculations

The KS equations(Eq.3.13) are solved numerically by self consistent method. In the beginning, an electron density is calculated from the superposition of atomic electron density. This is utilized to calculate the KS potentials and subsequently the KS equations are solved with single particle eigenvalues and eigenfunctions. The solutions of the KS equations are employed to generate a new electron density. In the next step, condition of self consistency is checked which could be the change in total energy or electron density from the previous iteration. If the condition is not fulfilled then electron density updated by mixing a small amount of electron density from the previous iteration and new cycle starts. This process iterates until the self consistency is achieved. After that, various quantities, like total energy, forces, stress, eigenvalues, density of states, band structure can be calculated from the converged density of electronic states.

To solve the KS equations numerous methods are available which can be broadly classified in two categories. One is fixed basis and cellular method, where the basis set are constant and only expansion parameters of the electronic wavefunctions are varied to attain the minimum of the total energy. On the other hand, the second method allows the basis sets to be updated at every iteration in the process to reach the self consistency. We used both the fixed basis set and plain wave basis methodology to solve the KS equations for electronic structure calculations which are inherent in **tight binding linear muffin-tin orbital atomic sphere approximation(TBLMTO-ASA)** [18] and **quantum espresso(QE)** [20] codes respectively. Following subsections provide a brief introduction to both the approaches.

3.2.1 Linear muffin-tin method(LMTO)

LMTO method was introduced by Anderson *et. al.* [20–22] which is one of the most successful methodology to solve the KS equations. In the LMTO, system is assumed to be composed of m$\ddot{u}$ffin-tin(MT) spheres of radius $\mathrm{s}_{\mathbf{R}}$ centred at sites **R**, where the potential is spherically on average inside this sphere. While it is constant outside the MT sphere as shown in the Fig.3.1. It can be defined as

$$V(\mathbf{r}) = V_0 + \sum_{\mathbf{R}} v_{\mathbf{R}}(\mathbf{r}_{\mathbf{R}}) \quad \mathbf{r}_{\mathbf{R}} = \mathbf{r} - \mathbf{R} \tag{3.26}$$

where

$$v_{\mathbf{R}}(\mathbf{r}_{\mathbf{R}}) = \begin{cases} v(r) & \mathrm{r}_{\mathbf{R}} \leq s_{\mathbf{R}} \\ 0 & \mathrm{r}_{\mathbf{R}} > s_{\mathbf{R}} \end{cases} \tag{3.27}$$

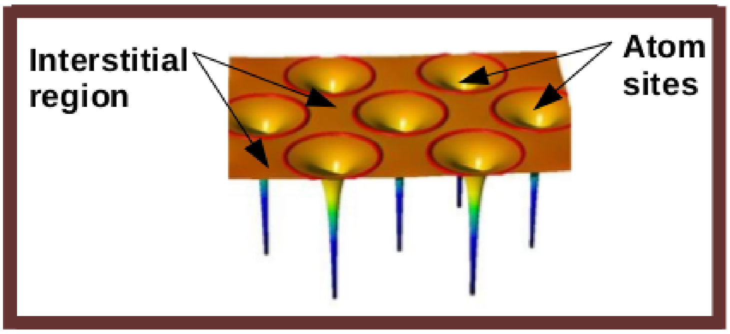

Figure 3.1: Mϋffin-tin potential with atomic sphere approximation (ASA).

The wavefunction corresponding to spherical potential inside the MT sphere can be written as

$$\phi_{\mathbf{R},L}(\mathbf{r},\epsilon) = \phi_{\mathbf{R},l}(r,\epsilon)Y_L(\hat{\mathbf{r}}), \quad L \equiv (l,m) \tag{3.28}$$

where L is the composite momentum and ϵ is the energy at which the solution is obtained. The functions $Y_L(\hat{r})$ are spherical harmonics and $\phi_{\mathbf{R},l}(r,\epsilon)$ is the radial amplitude which is solution of the following equation

$$\Big[-\frac{\partial^2}{\partial r^2} - \frac{2}{r}\frac{\partial}{\partial r} + \frac{l(l+1)}{r^2} v_{\mathbf{R}}(r) - \epsilon\Big]\phi_{\mathbf{R},l}(r,\epsilon) = 0 \tag{3.29}$$

On the other hand, the potential is assumed to be a constant outside the MT sphere. So, again the wavefunctions can be decomposed into the radial and angular parts. Now, considering the KE of electron (ϵ - V_0) outside the sphere is zero which is known as **atomic sphere approximation (ASA)**. The radial equation under this approximation takes the following form

$$\Big[-\frac{\partial^2}{\partial r^2} - \frac{2}{r}\frac{\partial}{\partial r} + \frac{l(l+1)}{r^2}\Big]R_l(r) = 0 \tag{3.30}$$

and its solution should be a linear combination of regular and irregular solutions

$$\begin{aligned} J_L(\mathbf{r}) &= J_l(r)Y_L(\hat{\mathbf{r}}) = \frac{1}{2(2l+1)}(\frac{r}{w})^l Y_L(\hat{\mathbf{r}}) \\ K_L(\mathbf{r}) &= K_l(r)Y_L(\hat{\mathbf{r}}) = (\frac{w}{r})^{(l+1)} Y_L(\hat{\mathbf{r}}) \end{aligned} \tag{3.31}$$

In order to match the solution of inside and outside the MT sphere smoothly at the sphere boundary($\mathbf{r}$ = $s_{\mathbf{R}}$), they have same logarithmic derivative at that point. The logarithmic derivative of radial function J_l(r) and K_l(r) are given by

$$D[J_l(r)] = l \quad ; \quad D[K_l(r)] = -l-1 \tag{3.32}$$

In order to satisfy the above matching condition

$$D[\phi_{\mathbf{R},l}(r,\epsilon)]|_{r=s_{\mathbf{R}}} = D[K_l(r)] = -l-1 \tag{3.33}$$

The case of many MT spheres

We generalize above mathematical recipe of single MT sphere to a realistic case, where multiple MT spheres are present in the system. In such a case, the solution Ψ(r) to the Schr$\ddot{o}$dinger equation can be written down as a linear combination of MT orbitals $\Psi_{\mathbf{R},L}$(**r**,ϵ)

$$\Psi(\mathbf{r}) = \sum_{\mathbf{R},L} a_{\mathbf{R},L}\Psi_{\mathbf{R},L}(\mathbf{r},\epsilon) \tag{3.34}$$

In this case, a linear combination of the J$_L$ and K$_L$ functions are required for the matching condition which can be done by calculating Wronskian of the functions. The matching of $\phi_{\mathbf{R},l}$(r,ϵ) at r = s$_{\mathbf{R}}$ is given by

$$N_{\mathbf{R},l}(\epsilon)\phi_{\mathbf{R},l}(r,\epsilon) \to K_l(r) - P_{\mathbf{R},l}(\epsilon)J_l(r) \tag{3.35}$$

where $P_{\mathbf{R},l}(\epsilon)$ and $N_{\mathbf{R},l}(\epsilon)$ are called potential and normalization functions respectively and defined as follows

$$P_{\mathbf{R},l}(\epsilon) = \left.\frac{\{\phi_{\mathbf{R},l}(r,\epsilon),K_l(r)\}}{\{\phi_{\mathbf{R},l}(r,\epsilon),J_l(r)\}}\right|_{r=S_{\mathbf{R}}} \text{ and } N_{\mathbf{R},l}(\epsilon) = \left.\frac{w}{2}\frac{1}{\{\phi_{\mathbf{R},l}(r,\epsilon),J_l(r)\}}\right|_{r=S_{\mathbf{R}}} \tag{3.36}$$

From these mathematical formulation the MT orbital $\Psi_{\mathbf{R},L}$(**r**,ϵ) takes the following form

$$\Psi_{\mathbf{R},L}(r,\epsilon) = \begin{cases} N_{\mathbf{R},l}(\epsilon)\phi_{\mathbf{R},l}(\mathbf{r},\epsilon) + P_{\mathbf{R},l}(\epsilon)J_L(\mathbf{r}) & \mathrm{r}_{\mathbf{R}} \le s_{\mathbf{R}} \\ K_L(\mathbf{r}) & \mathrm{r}_{\mathbf{R}} > s_{\mathbf{R}} \end{cases} \tag{3.37}$$

The parts which are inside and outside of the MT sphere are called its head and tail respectively. K$_L$(**r**) is defined as the envelope function and this function centred at site R and can be expanded in terms of the regular functions J$_L$($\mathbf{r}'_R$) centred at different sites $\mathbf{R}' \neq \mathbf{R}$

$$K_L(\mathbf{r_R}) = -\sum_{L'} S_{\mathbf{R},L,\mathbf{R}',L'}J_{L'}(\mathbf{r}_{\mathbf{R}'}) \quad \text{for } \mathbf{r}_{\mathbf{R}'} \le S_{\mathbf{R}'} \tag{3.38}$$

where S$_{\mathbf{R},L,\mathbf{R}',L'}$ is called canonical structure constant and defined as

$$S_{\mathbf{R},L,\mathbf{R}',L'} = \sum_{L''}(-1)^{(l''+1)}\frac{8\pi(2l''-1)!!C_{LL'L''}}{(2l'-1)!!(2l-1)!!}K_{L''}(\mathbf{R}'-\mathbf{R}) \tag{3.39}$$

where C$_{LL'L''}$ = $\int Y_L(\hat{\mathbf{r}})Y_{L'}(\hat{\mathbf{r}})Y_{L''}(\hat{\mathbf{r}})d\Omega$ are Gaunt coefficients.

Now, muffin-tin orbitals can be rewritten as

$$\Psi_{\mathbf{R},L}(\mathbf{r},\epsilon) = \begin{cases} N_{\mathbf{R},l}(\epsilon)\phi_{\mathbf{R},L}(\mathbf{r_R},\epsilon) + P_{\mathbf{R},l}(\epsilon)J_L(\mathbf{r_R}) & \mathrm{r}_\mathbf{R} \leq s_\mathbf{R} \\ \sum_{L'} S_{\mathbf{R},L,\mathbf{R}'L'} J_{L'}(\mathbf{r_{R'}}) & \mathrm{r}_{\mathbf{R}'} \leq s_{\mathbf{R}'}(\mathbf{R}' \neq \mathbf{R}) \\ K_L(\mathbf{r}) & \mathrm{r}_\mathbf{R} \in I \end{cases} \tag{3.40}$$

where I refers to the interstitial part *i. e.* the region outside the MT spheres.

To solve the KS equations using these new basis set of MT spheres, the term $\mathrm{P}_{\mathbf{R}'l}(\epsilon)J_{L'}(\mathbf{r}_{R'})$ inside the atomic sphere $\mathbf{R}'$ needs to be canceled from the tail contribution coming from all the other spheres. This condition is expressed as follows

$$\sum_{\mathbf{R},L} a_{\mathbf{R},L}[P_{\mathbf{R},l}(\epsilon)\delta_{\mathbf{R},L}\delta_{\mathbf{R}',L'} - S_{\mathbf{R},L,\mathbf{R}',L'}] = 0 \tag{3.41}$$

This is also known as **Korringa-Kohn-Rostoker(KKR)-ASA** equation.

Thus, the set of ϵ_i and $\mathrm{a}_{\mathbf{R},L}$ satisfying the above condition are the eigenvalues of KS equations and the corresponding eigenfunctions respectively. Physical significance of the potential term $\mathrm{P}_{\mathbf{R}L}$ is to define the scattering properties of the individual atoms and the structure constant $\mathrm{S}_{\mathbf{R},L,\mathbf{R}',L'}$ is to inform the positions of the different atoms. The main obstacle to solve this equation is the nonlinear energy dependence on the potential functions which forbids the standard diagonalization norm to solve the secular matrix. This problem is sortout by linearizing the KKR-ASA equation on the energy dependency.

Linearization of MT orbitals

In order to linearize the KKR-ASA equation, first we expand the radial function $\phi_{\mathbf{R},L}$(r,ϵ) around a characteristic energy ϵ = $\epsilon_{\nu,\mathbf{R},L}$ using a Taylor expansion.

$$\phi_{\mathbf{R},L}(r,\epsilon) = \phi_{\mathbf{R},L}(r) + \dot{\phi}_{\mathbf{R},L}(r)(\epsilon - \epsilon_{\nu,\mathbf{R},l}) + ... \tag{3.42}$$

By the linear combination of $\phi_{\mathbf{R},L}$(r) and $\dot{\phi}_{\mathbf{R},L}$(r) inside all the atomic spheres generates the modified linear muffin-tin orbital(LMTO).

$$\chi_{\mathbf{R},L}(\mathbf{r_R}) = \begin{cases} -\{K,\dot{\phi}\}_{\mathbf{R},l}\phi_{\mathbf{R},L}(\mathbf{r_R}) + \{K,\phi\}_{\mathbf{R},L}\dot{\phi}_{\mathbf{R},L}(\mathbf{r_R}) & \mathrm{r}_\mathbf{R} \leq s_\mathbf{R} \\ \sum_{L'} S_{\mathbf{R},L}S_{\mathbf{R}',L'}\left[\{J,\dot{\phi}\}_{\mathbf{R}',l'}\phi_{\mathbf{R}',L'}(\mathbf{r_R}') \right. & \\ \left. -\{J,\phi\}_{\mathbf{R}',l'}\dot{\phi}_{\mathbf{R}',L'}(\mathbf{r_{R'}})\right] & \mathrm{r}_{\mathbf{R}'} \leq s_{\mathbf{R}'}(\mathbf{R}' \neq \mathbf{R}) \\ K_L(\mathbf{r_R}) & \mathrm{r}_\mathbf{R} \in I \end{cases} \tag{3.43}$$

Now, an energy independent suitable basis set is available to solve the KS equations and eigenvalues can be obtained by solving the

$$\det\Big[\epsilon O_{\mathbf{R},L,\mathbf{R}',L'} - H_{\mathbf{R},L,\mathbf{R}',L'}\Big] = 0 \tag{3.44}$$

where $O_{\mathbf{R},L,\mathbf{R}',L'}$ and $H_{\mathbf{R},L,\mathbf{R}',L'}$ are overlap and Hamiltonian matrices respectively in this new basis set of LMTO.

This real space LMTOs can also be transformed to reciprocal space by using the Bloch sum

$$\chi_L^{\mathbf{k}}(\mathbf{r}) = \sum_{\mathbf{R}} e^{i\mathbf{k}.\mathbf{R}} \chi_{\mathbf{R},L}(\mathbf{r}_{\mathbf{R}}) \tag{3.45}$$

where the solutions are the linear combinations of the LMTOs

$$\Psi_{\mathbf{k},\nu}(\mathbf{r}) = \sum_{L} a_L^{\mathbf{k}\nu} \chi_L^{\mathbf{k}}(\mathbf{r}) \tag{3.46}$$

and the secular equation transforms to

$$\sum_{L} [\epsilon_\nu(\mathbf{k}) O_{L,L'}(\mathbf{k}) - H_{L,L'}(\mathbf{k})] a_L^{\mathbf{k}\nu} = 0 \tag{3.47}$$

Concept of Downfolding

Downfolding transformation is a very useful and powerful procedure in LMTO method. It reduces the size of an LMTO basis set by removing the orbitals of minor importance and accounting into the retaining orbitals. A prototype example is Si where d orbitals are lesser importance because the bonding is mainly sp^3 character, so these orbitals can be downfolded into the LMTOs of remaining s and p orbitals. We used this concept in the correlations study of Fe-chalocgenides which results will be discussed in details in chapter 8.

3.2.2 Plain Wave method

In this method, **plane waves(PWs)** e$^{i.\mathbf{kr}}$ are used to expand the eignfunctions of the KS equations. The basis set of wave vector is defined as follows

$$< \mathbf{r}|\mathbf{k} + \mathbf{G} >= \frac{1}{N\Omega} e^{i.(\mathbf{k}+\mathbf{G}).\mathbf{r}} \quad ; \quad \frac{\hbar^2}{2m}|\mathbf{k} + \mathbf{G}|^2 \leq E_{cut} \tag{3.48}$$

where Ω is unit cell volume, NΩ refers to crystal volume and E$_{cut}$ denotes to the cutoff on the kinetic energy(KE) of PWs. The KS equations have the following form in this basis set of PWs

$$\sum_{\mathbf{G}'} (< \mathbf{k} + \mathbf{G}|H_{KS}|\mathbf{k} + \mathbf{G}^{'} > -\epsilon_i \delta_{\mathbf{G}.\mathbf{G}'}) C_{i,\mathbf{k}+\mathbf{G}'} = 0 \tag{3.49}$$

The other major construction in this scheme is the potential exerted by the nuclei is replaced by **pseudopotential(PP)**. In the PP scheme an effective potential function is assumed in place of the original electron-ion core potential V$_{ei}$($\mathbf{r}$) as could be seen in Fig.3.2. One of the commonly used choice is

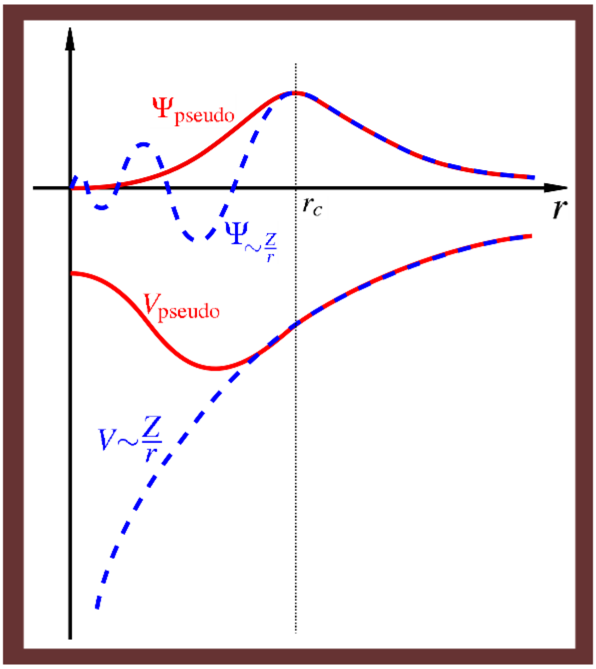

Figure 3.2: Graphical representation of pseudowavefunction and pseudopotential scheme.

$$V_{pp}(\mathbf{r}) = \begin{cases} A_l(E) & \mathbf{r} \leq \mathbf{r}_c \\ -\frac{Ze^2}{4\pi\epsilon_0 \mathbf{r}} & \mathbf{r} > \mathbf{r}_c \end{cases} \tag{3.50}$$

where, A_l is a constant potential which depends on angular momentum l and energy E. It can be determined with the help of bound state energies of atoms. The potential is purely Coulombic outside the radius r_c of valence core partition which is also called pseudoionize radius. In case, all electron orbital matches to corresponding pseudopotential orbital with continuous first derivative at $\mathbf{r} = \mathbf{r}_c$ then the PP is defined as **norm conserving pseudopotential(NC-PP)** [23]. This PP is highly efficient to reproduce the scattering properties of the true potential in a wide range of energies which is also known as “tranferability” of the PP. The nature of PP is substantially dependent on the value of $\mathbf{r}_c$. For example, if $\mathbf{r}_c$ is large then less number of PWs are sufficient enough to build a reasonable basis set for satisfactory results. However, for small $\mathbf{r}_c$ energy cutoff is required to be high. But the transferability decreases as the $\mathbf{r}_c$ increases, therefore it is difficult to work with NC-PPs of localized orbitals, like 3d transition metals. Because they demand large energy cutoff of the PWs for correct representation of pseudowavefunctions. Vanderbilt proposed a beautiful algorithm to sortout this problem *i. e.* **ultrasoft pseudopotential(US-PP)** [24]. In US-PP the norm conserving constraint is removed to optimize the smoothness of pseudo wavefunctions without sacrificing transferability. Beside this, PPs can also be modified according to the need of the system if the results from the standard PPs are not very much convincing by adjusting the boundary conditions, like the value of $\mathbf{r}_c$, changing the XC functional, reconstruction of all electron wavefunction, switching between non relativistic and fully relativistic parameters etc.

In the below, we present a comparison between some essential features of both the methods.

LMTO method	**PW method**
• Process of convergence is fast due to minimal basis set size formed by a few functions at each atom site.	• Many PWs are needed for reasonable basis set that result a slow convergence.
• Difficult to evaluate convergence quality.	• Evaluation of convergence quality can be improved easily by increasing the energy cutoff.
• Involvement of two and three centre integrals makes it difficult to implement.	• Presence of Fourier transform makes it simple to use.
• Finite system can be easily modeled.	• Supercell construction are required to handle the finite systems.
• Geometric optimization is not possible due to presence of pulay forces.	• Forces can be easily calculated due to absence of pulay forces thereby calculations of structural relaxation can be easily performed.

As it is clear from the above comparison that Fe-3d, highly localized, orbital requires large number of PWs for correct representation which causes high computational load. Therefore, we used the LMTO method for correlation study in Fe-chalcogenides. On the other hand, we employed PWs methodology(QE) to model the electronic structure of other compounds, which were used in our photoemission study, due to absence of the 3d localized orbital in the valence region of these compounds.

Bibliography

[1] L. H. Thomas, *Proc. Cambridge Phil. Roy. Soc.*, **23**, (1927), 542.

[2] E. Fermi, *Rend. Accad. Naz. Lincei*, **6**, (1927), 602.

[3] P. A. M. Dirac, *Proc. Cambridge Phil. Roy. Soc.*, **26**, (1930), 376.

[4] P. Hohenberg and W. Kohn, *Phys. Rev.* **136**, (1964), B864.

[5] M. Born and R. Oppenheimer, *Annalen der Physik*, **84**, (1927), 457.

[6] W. Kohn and L. J. Sham, *Phys. Rev.*, **140**, (1965), A1133.

[7] U. von Barth and L. Hedin, *J. Phys. C: Solid State Phys.*, **5**, (1972), 1629.

[8] J. P. Perdew and A. Zunger, *Phys. Rev. B*, **23**, (1981), 5048.

[9] J. P. Perdew and Y. Wang, *Phys. Rev. B*, **45**, (1992), 13244.

[10] J. P. Perdew, J. A. Chevary, S. H. Vosko, K. A. Jackson, M. R. Pederson, and C. Fiolhais, *Phys. Rev. B*, **46**, (1992), 6671.

[11] J. P. Perdew, K. Burke, and M. Ernzerhof, *Phys. Rev. Lett.*, **77**, (1996), 3865.

[12] A. Svane and O. Gunnarsson, *Phys. Rev. Lett.*, **65**, (1990), 1148.

[13] S. Massida, M. Posternak and A. Baldereschi, *Phys. Rev. B*, **48**, (1993), 5058.

[14] L. Hedin, *Phys. Rev.*, **139**, (1965), A796.

[15] V. I. Anisimov, F. Aryasetiawan and A. I. Lichtenstein, **J. Phys. Condens. Matter**, **9**, (1997), 767.

[16] J. C. Slater, Quamtem Theory of Atomic Structure, **Vol. 1.** McGraw-Hill, New York, (1960).

[17] V. I. Anisimov, J. Zaanen and O. K. Andersen, *Phys. Rev. B*, **44**, (1991), 943.

[18] R. W. Tank, O. Jepsen, A. Burkhardt and O. K. Andersen, *The Stuttgart TB-LMTO-ASA programe*, **Version 47**

[19] Giannozzi P. *et. al. http:/www.quantum-espresso.org*.

[20] O.K.Andersen, *Phys. Rev. B*, **12**, (1975), 3060.

[21] H. L. Skriver, **The LMTO method**, Springer, New York (1984).

[22] O.K.Andersen and O.Jepsen *Phys. Rev. Lett.*, **53**, (1984), 2571.

[23] D. R. Hamann, M. Shluter, and C. Chiang, *Phys. Rev. Lett.*, **43**, (1979), 1494.

[24] Vanderbilt D, *Phys. Rev. B*, **41**, (1990), 7892.

Chapter 4

A Comparative ARPES study on Bi_2Se_3 and BiSe topological insulators

In this chapter, first we present our ARPES results on strong TI Bi_2Se_3. Then, we compare these results with the ARPES results on a recently discovered BiSe compound, which has been predicted theoretically to be a weak TI. We observed a noticeable difference between the surface state bands of the two compounds which elucidates the vital role of structural geometry in governing the topological properties in Bi based binary TIs.

4.1 Introduction

In the past few years, many extensive studies have been reported on various aspects of a newly discovered state of matter called “Topological Insulator (TI)” [1, 2]. The reason to get such a high attention by this new state is its non trivial topological character. TIs promise to host many exotic features like, Dirac particle [1, 3], Majorana fermion [7, 8], and Magnetic monopole [4]. TIs exhibit insulating nature in bulk, like an ordinary insulator but has a conducting surface due to surface states(SSs). These SSs show a linear dispersion, like Dirac states. They also exhibit unique properties, for example spin-momentum locking, robustness against any non magnetic impurity and Anderson localization. Such a spin filtered and dissipationless surface currents are thought to be highly useful in spintronics [7] and transport devices [7,8]. Some of these SSs related properties have also been experimentally realized in many compounds, mainly in binary chalcogenides $(Bi,Sb)_2(Se,Te)_3$ [3, 12]. In the case of Bi_2Se_3 a clear Dirac like dispersion of the SSs has been observed in angle resolved photoelectron spectroscopy(ARPES) measurements and also their spin helicity have been confirmed by using spin resolved photoemission experiments [12]. These topological properties of binary compounds can further be tuned in quaternary compounds

$Bi_{2-x}Sb_xTe_{3-y}Se_y$(BSTS) by varying the pnictogen and chalcogen ratio. Many compounds of this family have been synthesized recently [13, 14].

These peculiar SSs are manifested from SOC induced band inversion in association with time reversal symmetry. The topological nature of these SSs are generally characterized by scheme of Z_2 indices(ν_0,ν) as proposed by Fu and Kane [13]. This value is calculated mainly from the bulk band structure of the system. Under this classification, systems those have ν_0 = 1 are defined as a strong TIs, like Bi_2Se_3 while the systems ν_0 = 0 are called weak TIs. The term 'weak' refers to fragile character of the SSs to disorder, unlike strong TIs [14]. Theoretical calculations have shown that they can host some interesting properties, like half integer quantum Hall effects [15]. However, so far experimental evidence of the weak topological insulating phase has been witnessed only in $Bi_4Rh_3I_9$ [30]. Recently, Wagmare *et. al.* [17] have found the calculated value of Z_2 invariant in BiSe is (0;001) which signifies its weak topological character. This prediction has been further supported by transport measurements on BiSe thin films by Anil Kumar *et. al.* [17]. The crystal structure of BiSe consists a Bi bilayer sandwitched between two Bi_2Se_3 type quintuple layers(QLs). The possible root for the emergence of the weak topological insulating phase in this system is the interlayer coupling between the Bi bilayer and Bi_2Se_3 QL [18]. Another report also supports existence of numerous TIs of $(Bi_2)_m(Bi_2Se_3)_n$ structural unit from calculations based on density functional theory(DFT) [19].

Experimental reports on weak TIs are very few. In this chapter we present a comparative ARPES study between the strong TI Bi_2Se_3 and weak TI BiSe. We observe clear Dirac like surface state bands(SSBs)and their temporal evolution due to band bending(BB) effects in Bi_2Se_3. Although, the atomic composition of BiSe is the same like that of Bi_2Se_3, the SSBs in BiSe resembles Rashba split states. This could be the manifestation of Rashba splitting in Bi bilayer states due to charge transfer from the terminated Bi bilayer to adjacent Bi_2Se_3 QL. Our findings elucidate the role of structural geometry in the formation of topological character of Bi based binary TIs.

4.2 Experimental Details

High quality single crystals of Bi_2Se_3 and BiSe were grown by modified Bridgman method and details can be found from previous reports [17, 20]. Single crystals were cleaved *in-situ* in the preparation chamber at a pressure of 1.0×10^{-9} mbar using standard post technique. ARPES measurements were carried out by using a high flux GAMMADATA VUV He lamp (VUV5000) attached to a VUV monochromator (VUV5040) and a SCIENTA R3000 analyser. At the HeI line(21.2 eV), the photon flux was of the order of 10^{16} photons/s/steradian with a beam spot of

2 mm. Fermi energies were calibrated by measuring on a freshly evaporated Ag film on to the sample holder. The total energy resolution estimated from the width of the Fermi edge, was about 27 meV for the HeI excitation energy while the angular resolution was better than 1° in the wide-angle mode(8°) of the analyser. All the measurements were performed inside the analysis chamber under a base vacuum of 4.0×10^{-10} mbar at room temperature.

4.3 Results and Discussion

Fig.4.1(a) shows the primitive unit cell of Bi_2Se_3 which has a rhombohedral structure, where layers of Bi(red) and Se(green) atoms are arranged in an order Se1-Bi-Se-Bi1-Se2. This arrangement holds a center of inversion at the Se atom site which makes Se1 and Bi atoms equivalent to Se2 and Bi1 atoms respectively. This arrangement is defined as a quintuple layer (QL). A more clear picture of this layered structure is apparent in a hexagonal unit cell as displayed in Fig.4.1(b), where one of the QL region is marked by a rectangular box. Bonding between the adjacent QLs is relatively weak compared to the bonding within the QL and van der Wall nature. This bonding characteristics provides an easily cleavable plane for ARPES measurements. On the other hand, in case of BiSe crystal a Bi bilayer (blue atoms) resides between the two adjacent QL structure of Bi_2Se_3 as could be seen in Fig.4.1(c). Fig.4.1(d) depicts a low energy electron diffraction (LEED) image of the Bi_2Se_3 surface. The hexagonal symmetry of the surface Brillouin zone (BZ) is clearly visible from the diffraction spots. Further, high symmetry k-points Γ, K and M are marked. Γ-K' denotes k- direction along which bands are mapped in our ARPES measurements, which is offset from the Γ-K direction by 15°.

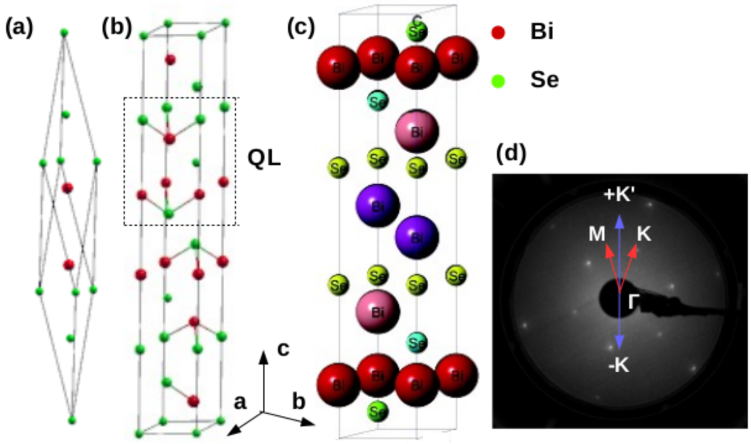

Figure 4.1: (a) and (b) Primitive and hexagonal unit cell structure of Bi_2Se_3. (c) Crystal structure of BiSe. (d) LEED image of Bi_2Se_3 where high symmetry k-points Γ, K and M are marked. Blue arrow denotes Γ-K' direction along which bands are mapped and it is offset from Γ-K direction by 15°

Fig.4.2(a) and (b) display the ARPES intensity plots along the Γ-K' direction of the surface BZ taken at He-I(21.2 eV) and He-II (40.8 eV) photon energy respectively. Intensity pattern seen in the Fig.4.2(a) informs that various bands are present in the binding energy (BE) range E_b = -0.3 eV to -5.0 eV of the valence band (VB) and they are strongly dispersive in nature. Interestingly, a faint intensity (enclosed in red colour box) is also observed in the vicinity of the E_f which is confined to a narrow k-spacing around the Γ point, despite the fact that Bi_2Se_3 is a semiconductor. Comparing these results with He-II case (Fig.4.2(b)) it is found that dispersion of the bands lying at deeper BE modifies sharply while the near E_f cone type feature remains intact. The photoelectrons extracted from these two photon energies correspond to different k values along the perpendicular direction (k_z) to the sample surface. Therefore, constant shape of the cone type bands, while varying the photon energy, indicates that there is no dispersion along the k_z direction in these bands. This result shows the two dimensional character of these bands and they are surface state bands (SSBs).

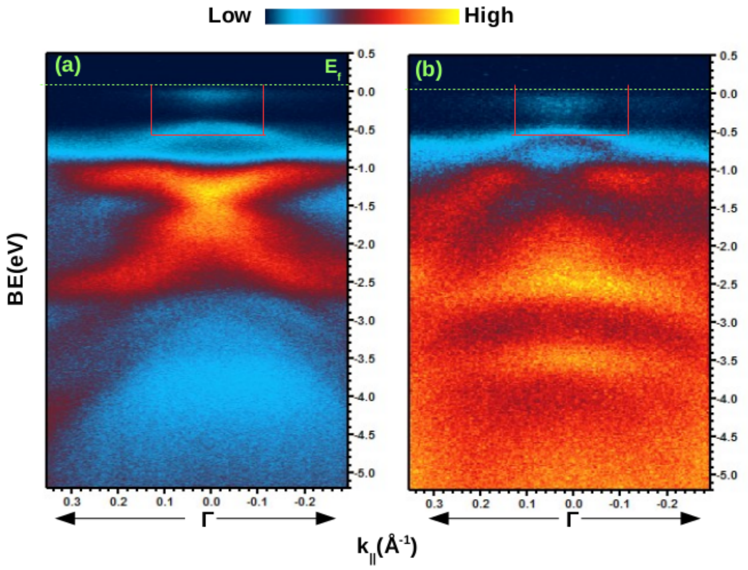

Figure 4.2: (a) and (b) ARPES intensity plots of Bi_2Se_3 taken along the Γ-K' direction of the surface BZ using He-I(21.2 eV) and He-II(40.8 eV) photon energy respectively.

In order to trace the characteristics of SSBs, high resolution image of the near E_f region is presented in Fig.4.3(a). In this image two distinct SSBs (green doted line) can be clearly seen which show a linear dispersion like Dirac states. These bands meet $\sim E_b$ = -0.28 eV at the Γ point which is called Dirac point (DP). The intensity distribution between these two SSBs represents the filled conduction band (CB) states. On the other hand, bulk VB spanning in BE range E_b = -0.3 to -0.6 eV, shows an inverted parabolic dispersion. Electron band velocity is $\sim 3.1 \times 10^5$ m/s around the DP as estimated from the slope of SSB using relation $1/\hbar\, \partial E/\partial k$. These observations are fairly consistent with previous ARPES reports [12]. Another interesting feature observed in this system is the gradual shifting of the SSBs towards the higher BE as time elapses after the sample cleaving. This behaviour is clearly evident in Fig.4.3(b) which is collected ∼ 10 hr. after the measuring time of Fig.4.3(a). In this figure, the position of DP lies at substantially higher BE ∼ E_b = -0.4 eV in comparison to Fig.4.3(a) and also the separation between the two SSBs increases in k space as denoted by an arrow. This temporal evolution of the SSBs is a signature of BB which is caused due to accumulation of additional charges at the surface. The sources of these charges could be Se vacancies and adsorption of residual gases at the surface [11, 12, 34, 35]. In addition, significant enhancement is also found in the bulk CB states. These BB induced changes are also reflected in the energy density curves (EDC). Fig.4.3(c) and (d) represent plots of EDC spectra extracted from the Fig.4.3(a) and (b) respectively. In Fig.4.3(c), two features are observed at the Γ point(ϕ = 0.0) spectra(black). One occurs at near the E_f and the second ∼ E_b = -0.5 eV. Intensity of the

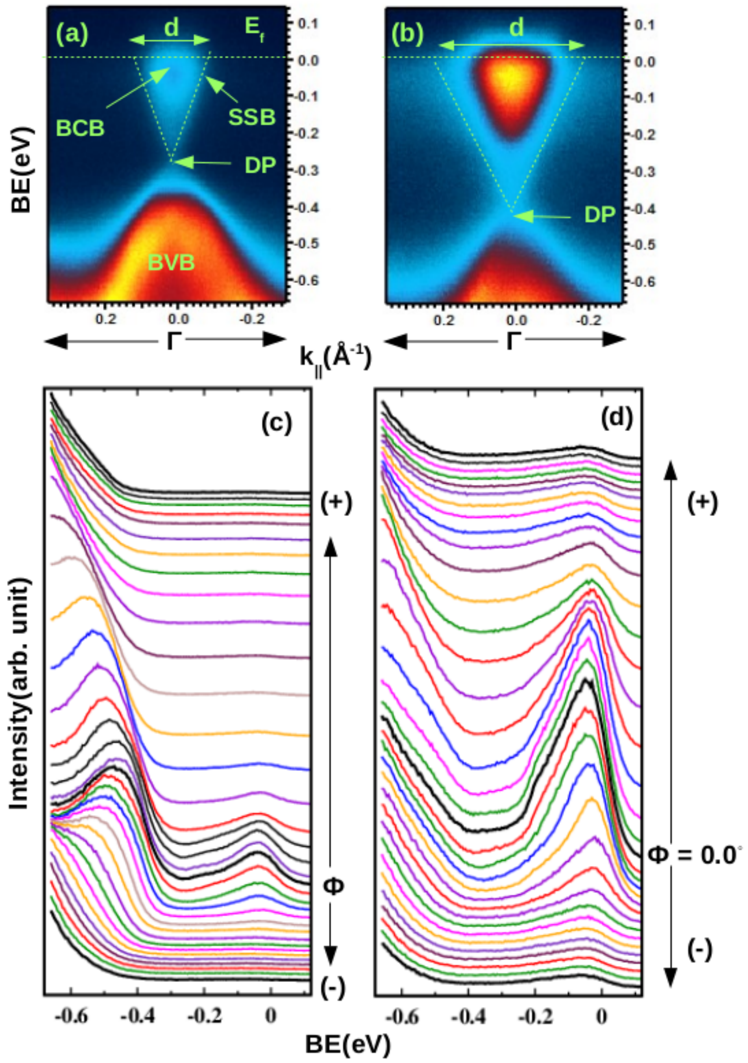

Figure 4.3: (a) and (b) ARPES intensity plots of Bi_2Se_3 in the near E_f region taken ∼ 0:30 hr. and 11:00 hr. after the sample cleaving using He-I photon energy respectively. (c) and (d) EDC plots extracted from the images(a) and (b) respectively.

later feature is much higher than the former. This situation is completely changed in the Fig.4.3(d) where the near E_f feature appears as an intense peak type structure while the higher BE feature is missing at the Γ point spectra. The same behaviour also persists at different ϕ spectra.

As discusses previously, the crystal structure of BiSe is composed of same atomic elements (Bi and Se) as presented in Bi_2Se_3 and differs only in their arrangement (see Fig.4.1(b) and (c)). In order to investigate the role of structural geometry, we performed ARPES measurements on BiSe and the results are presented in Fig.4.4. Fig.4.4(a) corresponds to the ARPES intensity map taken along the Γ-M direction of the surface BZ of BiSe. In this image two parabolically dispersing SSBs can be identified. These are strikingly different from the Dirac like surface states observed in Bi_2Se_3(Fig.4.3(a)). These two inverted parabolic SSBs, which are separated in k-space resembles to Rashba split (RS) states. The crossing of these two SSBs (E_R) occurs $\sim$ -0.2 eV BE at the Γ point while their apexes just touch the E_f around $k_{||}$ = $\pm$ 0.2 eV Å^{-1}(k_0). From these values we estimated the Rashba split parameter(E_R/k_0) to be $\sim$ 0.3 which is small in comparison to the Bi based system Bi_2Te_2Se [24]. This observation of RS like SSBs is consistent with the theoretical prediction by Wagmare *et. al.* [17]. In order to see the behaviour of the SSBs at other k values in the BZ, we collected the ARPES images along the k-directions Γ-M'(Fig.4.4(b)) and Γ-M''(Fig.4.4(c)) which are 8° and 15° offset from the Γ-M direction respectively. In image of Fig.4.4(b) one of the RS split SSBs is completely visible however, interference of the bulk VB and bulk CB states make it obscure to identify clearly. Similarly, Fig.4.4(c) also indicates the presence of RS like SSBs. The position of E_R and k_0 are found to be at larger values compared to their values in Fig.4.4(a). This difference is possibly a signature of the BB effect, analogous to the situation in Bi_2Se_3 mentioned previously. Image in Fig.4.4(a) was collected after 0:30 hr. from sample cleaving whereas the image in Fig.4.4(c) was recorded 4:00 hr. after the cleaving. Likewise, occurrence of a triangular shape intensity patch in the middle of the two SSBs at the Γ point indicates the large enhancement in the filled CB states, similar to the increment in intensity confined between the two SSBs in Bi_2Se_3(Fig.4.3(b)) case. In order to see changes in the spectral features, EDC plots are presented in Fig.4.4(d)-(f) which are obtained from the intensity maps Fig.4.4(a)-(c). In these plots, near E_f high spectral weight can be seen at the Γ point(ϕ = 0.0°) spectra(black) which remains almost same in all other spectra corresponding to different ϕ angles. This observation is contrary to the case of Bi_2Se_3(Fig.4.3d)), where the near E_f feature intensity rapidly falls as moving to either side of the Γ point(ϕ = 0.0°). Thus, these results inform that the RS like SSBs persist along different k-cuts and it could be an indication of their isotropic nature. The origin of these states probably lies in the coupling between the Bi bilayer and its nearest QL. This causes a charge transfer from Bi bilayer terminated surface to adjacent QL and thereby leads

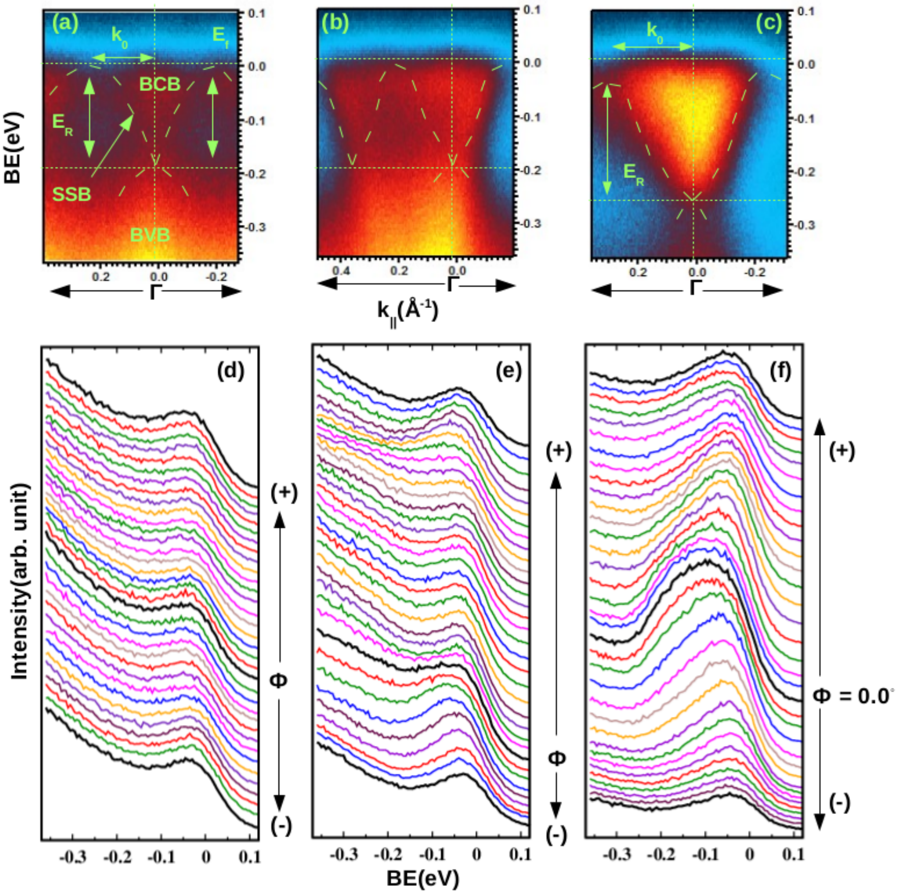

Figure 4.4: (a) ARPES intensity map taken along Γ-M direction of the surface BZ of BiSe. (b) and (c) are the same images taken along Γ-M' and Γ-M" directions which are 8° and 15° offset from the Γ-M direction respectively. (d) - (e) EDC plots obtained from the images(a) - (c) respectively.

to Rashba kind of splitting in the exposed Bi bilayer states [18]. Our findings also have a fairly good agreement with previously reported ARPES results on similar system Bi films grown on Bi_2Se_3 [25].

Recently Wagmare *et. al.* [17] have shown that the calculated value of Z_2 indices in BiSe is (0;001). This suggests that BiSe belongs to a category of weak TIs under the classification scheme proposed by Fu and Kane [13]. This weak topological signal has been further endorsed by weak-antilocalization cusp seen in magnetoresistance measurements by Anil Kumar *et. al.* [17]. From our ARPES results, it can be seen that the observed SSBs signal in the weak TI BiSe are distinctly different from the nature of SSBs in the strong TI Bi_2Se_3. This emphasize that the origin of SSBs in the two compounds is different as proposed by the calculations.

4.4 Conclusion

We present a comparative study of our ARPES results on Bi_2Se_3 and BiSe. We observed Dirac like linearly dispersing bands in the bulk energy gap region of Bi_2Se_3 which originate from the surface states. These states gradually shift towards higher BE as a function of time after the cleaving due to BB effects. Interestingly, the SSBs in BiSe resembles RS states unlike the Bi_2Se_3. This RS type surface states are also found along the different k-directions. The effects of BB are also seen in this system which drags these states to higher BE as time elapses after cleaving. These RS states could be originating from the coupling between the Bi bilayer and the adjacent QL as predicted by the DFT calculations. Further, theoretical calculations have shown that BiSe and Bi_2Se_3 belong to weak and strong classes of TIs respectively. In our comparative ARPES study of BiSe and Bi_2Se_3 we have also found difference in their SSBs features, though these compounds have same elemental composition. These findings reveal the important role of structural geometry in the topological properties of Bi based binary TIs.

Bibliography

[1] M. Z. Hasan and C. L. Kane, *Rev. Mod. Phys.*, **82**, (2010), 3045.

[2] Xiao-Liang Qi and Shou-cheng Zhang, *Rev. Mod. Phys.*, **83**, (2011), 1057.

[3] Y. Xia, D. Qian, D. Hsieh, L.Wray, A. Pal, H. Lin, A. Bansil, D. Grauer, Y. S. Hor, R. J. Cava and M. Z. Hasan, *Nat. Phys.*, **5**, (2009), 398.

[4] Liang Fu and C. L. Kane, *Phy. Rev. Lett.*, **100**, (2008), 096407.

[5] David Hsieh, Y Xia, L Wray, Dong Qian, A Pal, JH Dil, J Osterwalder, F Meier, G Bihlmayer, C L Kane, Y S Hor, R J Cava, M Zahid Hasan, *Science*, **323**, (2009), 919.

[6] Xiao-Liang Qi, Rundong Li, Jiadong Zang, Shou-Cheng Zhang, *Science*, **323**, (2009), 1184.

[7] Shun-Qing Shen, Spintronics and spin current, *AAPPS Bulletin*, **18**, (2008), 29.

[8] Liang Fu and C. L. Kane, *Phy. Rev. Lett.*, **102**, (2009), 216403.

[9] A. R. Akhmerov, Johan Nilsson, and C.W. J. Beenakker, *Phy. Rev. Lett.*, **102**, (2009), 216404.

[10] D. Hsieh, Y. Xia, D. Qian, L. Wray, J. H. Dil, F. Meier, J. Osterwalder, L. Patthey, J. G. Checkelsky, N. P. Ong, A. V. Fedorov, H. Lin, A. Bansil, D. Grauer, Y. S. Hor, R. J. Cava and M. Z. Hasan, *Nat. Lett.*, **460**, (2009), 1101.

[11] Zhi Ren, A. A. Taskin, Satoshi Sasaki, Kouji Segawa, and Yoichi Ando, *Phy. Rev. B*, **82**, (2010), 241306(R).

[12] Zhi Ren, A. A. Taskin, Satoshi Sasaki, Kouji Segawa, and Yoichi Ando, *Phy. Rev. B.*, **84**, (2011), 165311.

[13] Liang Fu, C. L. Kane and E. J. Mele, *Phy. Rev. Lett.*, **98**, (2007), 106803.

[14] C. L. Kane and E. J. Mele, *Phy. Rev. Lett.*, **95**, (2005), 146802.

[15] Chao-Xing Liu, Xiao-Liang Qi and Shou-Cheng Zhang, *Physica E*, **44**, (2012), 906.

[16] Bertold Rasche, Anna Isaeva, Michael Ruck, Sergey Borisenko, Volodymyr Zabolotnyy, Bernd Bchner, Klaus Koepernik, Carmine Ortix, Manuel Richter and Jeroen van den Brink, *Nat. Mater.*, **12**, (2013), 422.

[17] Kunjalata Majhi, Koushik Pal, Himanshu Lohani, Abhishek Banerjee, Pramita Mishra, Anil K Yadav, R Ganesan, B R Sekhar, Umesh V Waghmare and P S Anil Kumar, *arXiv:1605.01613v1*

[18] K. Govaerts, K. Park, C. De Beule, B. Partoens and D. Lamoen, *Phy. Rev. B.*, **90**, (2014), 155124 .

[19] J. Zhang, X. Liu and G. Huang, *Phy. Stat. Solidi(b)*, **9**, (2015), 252.

[20] Anil K. Yadav, Kunjalata Majhi, Abhishek Banerjee, R.Ganesan, P. Mishra, **H. Lohani**, B. R. Sekhar and P. S. Anil Kumar, *AIP Conference Proceedings*, **1731**, (2016), 100012.

[21] Hadj M. Benia, Chengtian Lin, Klaus Kern, and Christian R. Ast, *Phy. Rev. Lett.*, **107**, (2011), 177602.

[22] P Rakyta, B Ujfalussy and L Szunyogh, *New. J. Phys.*, **17**, (2015), 123011.

[23] T. Forster, P. Kruger and M. Rohlfing, *Phy. Rev. B.*, **91**, (2015), 035313.

[24] K Miyamoto, T Okuda, M Nurmamat, M Nakatake, H Namatame, M Taniguchi, E V Chulkov, K A Kokh, O E Tereshchenko and A Kimura, *New. J. Phys.*, **16**, (2014), 065016.

[25] Lin Miao, Z. F. Wang, Wenmei Ming, Meng-Yu Yao, Meixiao Wang, Fang Yang, Y. R. Song, Fengfeng Zhu, Alexei V. Fedorov, Z. Sun, C. L. Gao, Canhua Liu, Qi-Kun Xue, Chao-Xing Liu, Feng Liu, Dong Qian, and Jin-Feng Jia, *PNAS*, **110**, (2013), 2758.

Chapter 5

Band Structure of Topological Insulator $BiSbTe_{1.25}Se_{1.75}$

In this chapter, we extended our previous work on Bi based binary TIs to quaternary alloy $BiSbTe_{1.25}Se_{1.75}$(BSTS). We performed a detail electronic structure study of BSTS using ARPES and first principles method. Our study shows that the topological character of Bi based compounds, besides structural geometry(result of previous chapter) also depends crucially on the atomic composition.

5.1 Introduction

Discovery of the new quantum state of matter called "topological insulators (TI)" have attracted world wide interest due to their exotic properties which are manifestations of a non-trivial band topology [1,2]. TIs have insulating bulk and conducting edges due to the presence of some peculiar surface states (SSs). These SSs are spin non-degenerate with a unique property of spin momentum locking which results from the strong spin-orbit coupling (SOC) effects in combination with time reversal symmetry. It has been theoretically predicted that these SSs host many interesting properties like, Dirac fermion [1, 3], magnetic monopole [4] and Majorana bound state at the vortex in superconducting regime [7, 8]. Strong immunity of these SSs to Anderson localization and backscattering in presence of non-magnetic impurities have tremendous technical advantages, especially for functional applications like spintronic devices and quantum computers [7, 8]. Furthermore, tunability of the crossing point of the topological SSs, called the Dirac point (DP) by chemical doping, is another aspect important from such technological point of view [9–12]. In the known Bi and Sb based binary TIs the DP and the SSs are often obscured by contributions from bulk states. Tetradymite Bi_2Te_2Se which is isostructural to the protypical TIs Bi_2Se_3 and Bi_2Te_3 has been found to be suitable for such tuning of the DP within the bulk band gap owing to its relatively large bulk resistivity [13]. The resistivity can be optimized in the Sb doped quaternary alloy $Bi_{2-x}Sb_xTe_{3-y}Se_y$ by changing the ratio of the pnictogen (Bi and Sb) and chalcogen (Se and Te) atoms without disturbing its crystallinity. In this compound, topological nature with different bulk resistivity has been experimentally observed in a wide range of x and y combinations [14]. Thus, $Bi_{2-x}Sb_xTe_{3-y}Se_y$ provides an ideal platform to study the nature of topological surface states by tuning the Dirac node through controlling the proportion of chalcogen/pnictogen atoms.

Recently, quantum hall effect (QHE) [15] and scanning tunnelling spectroscopy (STS) [16] studies have been used to confirm the topological characters of $BiSbTeSe_2$ and $Bi_{1.5}Sb_{0.5}Te_{1.7}Se_{1.3}$. Tunability of the Dirac cone also has been observed in some of the compositions of $Bi_{2-x}Sb_xTe_{3-y}Se_y$ by using angle resolved photoelectron spectroscopy (ARPES) measurements [18, 19]. While most of the reported studies were focussed on the tunability by chemical doping or adding layers of other elements on the surface of TIs, the drifting of the topological surface state bands (SSBs) and DP with aging of the surface which is also important for device applications [20], has not been addressed adequately in this family of TIs [9, 10]. In this chapter, we present a detailed study of the electronic structure and aging effects of $BiSbTe_{1.25}Se_{1.75}$(BSTS) using ARPES in conjunction with density functional theory (DFT) based calculations. In the ARPES data, we observe topological character of the SSBs and a strong warping of the Fermi surface (FS). These results are consistent with our calculated SSBs which fall within the region of bulk band gap. In addition, we find pronounced effects of aging due to band bending (BB) and it is relatively stronger in this compound in comparison to the Bi_2Se_3. The BB effects are enhanced due to the high adsorption of residual gases at low temperatures. Furthermore, experiments performed with constant dosing of different gases show that the BB effects are highly sensitive to gas species.

5.2 Experimental and Calculation Details

The high quality single crystal samples of $BiSbTe_{1.25}Se_{1.75}$(BSTS) used in this study were grown by modified Bridgman method. Stoichiometric amounts of Bi(99.999%), Sb(99.999%), Te(99.999%) and Se(99.999%) were heated in evacuated quartz ampoules to a temperature of 1073 K followed by slow cooling. Large sized single crystals($\sim$ 5 cm) were obtained that cleaved easily along planes normal to the c-axis. The ARPES experiments were carried out using the facilities associated with the BaDELPH beamline of ELETTRA synchrotron center, Italy, equipped with a SPECS Phoibos 150 hemispherical analyser. The photoemission spectra were collected on freshly cleaved (*in-situ* at 77K) surfaces of crystals under a vacuum of the order of 4.0×10^{-11} mbar. In addition, ARPES data were taken by using our laboratory facility decked with a high flux GAMMADATA VUV He lamp (VUV5000) attached to a VUV monochromator (VUV5040) and a SCIENTA R3000 analyser. Fermi energies of the samples were calibrated by using a freshly evaporated Ag film on the sample holder. The total energy resolution estimated from the width of the Fermi edge, was about 27 meV for HeI excitation energy. The angular resolution was better than 1° in the wide-angle mode (8°) of the analyzer. All the measurements were performed inside the analysis chamber under a base vacuum of 3.0×10^{-10} mbar

First-principles calculations were performed by using a plain wave basis set inherent in Quantum Espresso (QE) [20]. Many electron exchange-correlation energy was approximated by the Perdew-Burke-Ernzerhof (PBE) functional [21–23]. Fully relativistic ultrasoft [24] and non relativistic norm conserving pseudopotentials were employed for spin-orbit-coulpled (SOC) and non SOC calculations respectively. Fine mesh of k-points with Gaussian smearing of the order 0.0001 Ry was used for sampling the Brillouin zone integration, and kinetic energy and charge density cut-off were set to 100 Ry and 450 Ry respectively. Surface state calculations on (111) plane were performed using supercell structures of hexagonal unit cell consisting six quintuple layer (QL) with a vacuum separation of ~ 26 Å. Experimental lattice parameters [14] and atomic coordinates were relaxed under damped (Beeman) dynamics with respect to both ionic coordinates and the lattice vectors for all the structures.

5.3 Results and Discussion

Fig.5.1(a) shows the primitive unit cell of $BiSbTeSe_2$ which has a rhombhohdral symmetry. This structure can also be depicted as a hexagonal unit cell as shown in Fig.5.1(b). Basic building block of this structure is the so called quintuple layer (QL) which consists of five atoms arranged in an order Se1-Bi-Se-Sb-Te. The Bi(Se1) atoms are connected to the Sb(Te) atoms with the center of inversion symmetry at the Se atom site. The structure of $BiSbTeSe_2$ is similar to that of Bi_2Se_3. Substitution sites of Sb and Te in Bi_2Se_3 to build the $BiSbTeSe_2$ structure are chosen by considering the total energy minimization among various possible structures. Fig.5.1(c) shows the Brillouin zone (BZ) of the primitive unit cell where the high symmetry k-points are marked. In Fig.5.1(d) we have shown a low energy electron diffraction (LEED) pattern from our BSTS crystal depicting the hexagonal symmetry of the surface BZ. The BSTS crystal cleaves along the (111) crystal plane and scanning tunnelling microscopy experiments have shown that the terminated plane has Te/Se atoms on it [16].

Fig.5.2(a) and (b) show bulk band structure of nominal $BiSbTeSe_2$ composition without and with inclusion of SOC effects respectively. In both the cases, valence band(VB) and conduction

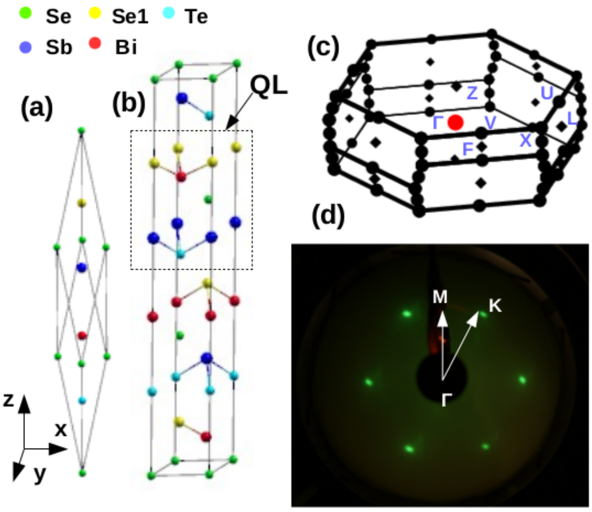

Figure 5.1: (a) and (b) show the primitive and hexagonal unit cells of $BiSbTeSe_2$ respectively. The dotted box encloses the structure of five atomic layers which is called quintuple layer (QL). (c) Brillouin zone of the primitive unit cell where high symmetry k-points are marked. (e) LEED spots depict the hexagonal symmetry of the surface BZ of BSTS where the high symmetry k-directions Γ-K and Γ-M are marked.

band(CB) states are well separated in energy scale. However, the SOC effects induce a small splitting in the bands along various k-directions. The band gap is $\sim$ 0.45eV at Γ point in SOC included case(Fig.5.2(b)) which is higher than the value 0.3eV found in Bi_2Se_3 [17]. Structure of the top most VB(red) and the lowest CB(blue) along the F-Γ-L direction indicate a band inversion at the Γ point after incorporating the SOC effects. This results in a non-trivial value of the Z_2 invariant in this system [26]. In Fig.5.2(c) and (d) the ARPES intensity plots of BSTS, which has a slightly different stoichiometry ($BiSbTe_{1.25}Se_{1.75}$) from the nominal composition ($BiSbTeSe_2$), are presented. These plots are taken along the Γ-M and Γ-K directions of the surface BZ by using 31eV photon energy respectively. Among the various bands seen in the VB region, the deeper lying bands with binding energy (BE) in the range E_b = -0.5 to -4.5 eV show a highly dispersive nature. A cone shaped distribution of low intensity is clearly visible in the vicinity of the E_f around the Γ point which is absent in the calculated band structure. The cone is formed by the topological SSBs in the bulk band gap region of the material. Although, inconsequential to the results of this study, a closer look at the data in the Fig.5.2(c) will reveal the existence a small energy gap near the tip of the cone which could be due to some possible misalignment of the angular position of the sample to the perfect Γ-M direction during the data collection. Nevertheless, in order to have a better comparison, raw data of the bulk bands along the Γ-F and Γ-L directions (Fig.5.2(b)) which correspond to the Γ-M and Γ-K directions of the surface BZ, are plotted adjacent to ARPES images in Fig.5.2(e) and (f) respectively. Along both the directions, the calculated bands placed at

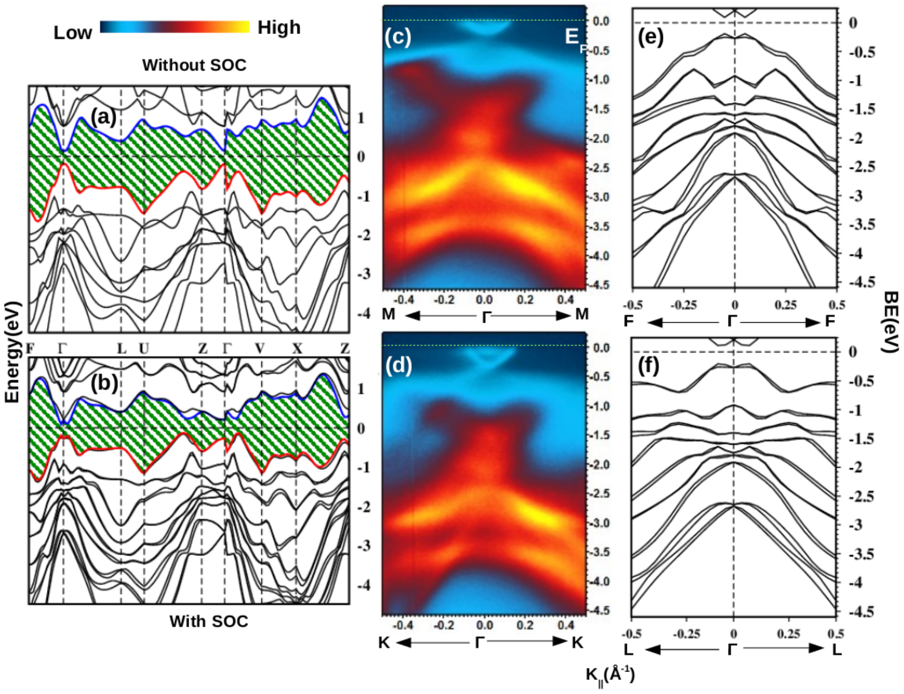

Figure 5.2: (a) and (b) show bulk band structure plots of $BiSbTeSe_2$ without and with inclusion of SOC effects respectively. (c) and (d) show ARPES images of BSTS along the Γ-M and Γ-K directions of the surface BZ respectively. (e) and (f) show the bulk bands of (b) along the Γ-F and Γ-L directions respectively.

higher BE show a fair resemblance to the corresponding intensity pattern observed in the ARPES images.

Fig.5.3(a) shows the near E_f region of ARPES plot taken by using 35 eV photon energy. The two SSBs are clearly visible exhibiting almost a linear dispersion. Intensity between these two SSBs indicates presence of the bulk conduction band (BCB) states occupied due to n-type intrinsic impurities and defects. On the other hand, lower part of the Dirac cone strongly overlaps with the bulk valence band (BVB) states which form a high intensity region at $\sim E_b$ = -0.4 eV. In order to identify the position of the DP, the corresponding energy density curve (EDC) of the image shown in Fig.5.3(a) is plotted in Fig.5.3(b). This EDC is the data taken at the Γ point with k width of $\pm$ 0.02 $Å^{-1}$. As is clear from this spectra the DP appearing at $E_d \sim$ -0.2 eV is obscured by the emission from the BVB states. In order to confirm the surface nature of the SSBs, ARPES images were collected at different photon energies as shown in Fig.5.3(a), (c), (e) and (g) which correspond to images taken at photon energy 35, 33, 31 and 28 eV respectively. EDC spectra (at the Γ point with k width of $\pm$ 0.02 $Å^{-1}$) corresponding to these intensity plots are presented in Fig.5.3(b), (d), (f) and (h) respectively. The BVB gets modified sharply with the variation in photon energy indicating the bulk nature of these higher BE bands while the shape of near E_f

SSBs (upper part of Dirac cone) remains unaffected confirming the surface state character. The slight variation in the intensity of these SSBs is due to the difference in the matrix elements involved in the photoemission process [3]. It should be noted that the SSBs show some significant changes close to the DP. The EDC spectra of 33 eV photon energy (Fig.5.3 (d)) shows an apparent opening of a gap in the SSBs in the vicinity of the DP (E_d = - 0.2 eV), unlike the case of 35 eV photon energy (Fig.5.3 (b)). Similarly, the spectral weight near $\sim$ -0.2 eV BE in the EDC of 31 eV (Fig.5.3 (f)) also shows differences compared to that taken with 28 eV (Fig.5.3 (h)) photon energy. These results show that the SSBs are not of pure 2D character in this compound. The SSBs which mainly form the lower part of the Dirac cone hybridize with the BVB states and therefore acquire a partial 3D character. Origin of these hybridized states could be the impurities or defects in the system as suggested in a theoretical model for finite bulk band gaps by Balatsky *et. al.* [27]. Experimental realization of such impurity induced gap opening in the SSBs at the DP has been recently reported by Rader *et. al.* in their detail ARPES study of $(Bi_{1-x}Mn_x)_2Se_3$ system [28]. Fig.5.3(i) and (k) show the ARPES plot taken with s and p-polarized light of photon energy 31 eV respectively and adjacent Fig.5.3(j) and (l) display the EDC spectra (at the Γ point with k width of $\pm$ 0.02 Å^{-1}) corresponding to them. In both the cases the linearly dispersive SSBs are clearly seen. However, the intensity of the BVBs at $\sim$ E_b = -0.5 eV got drastically reduced in the p-polarized case compared to the s-polarized. These changes are also visible in the spectral features of their EDCs (Fig.5.3(j) and (l)) showing the different orbital character of these bands.

Fig.5.4(a) shows the near E_f region of ARPES intensity plot of BSTS taken by using 31 eV photon energy depicting the two linearly dispersive Dirac like SSBs. In order to demonstrate the evolution of the intensity distribution of the SSBs, we have plotted the constant energy contours (CEC) in Fig.5.4(b), (c) and (d). The Fig.5.4(b) and (d) correspond to the constant BE energy E_f and E_d respectively while Fig.5.4(c) represents the mid point energy (E_m) between the E_f and E_d. The CEC appears nearly in a circular shape around the Γ point at E_d which constantly grows in size and deforms to a hexagonal geometry as energy moves towards the E_f, where BCB states are present. It is evident from Fig.5.4(b) that the intensity shrinks between the two Γ-M directions and reaches its minimum value along the Γ-K direction. This deviation of FS from circular to hexagonal shape has been observed in other TIs also, like Bi_2Te_3 [29] and results in a snow flake like structure of the FS.

Characteristics of the SSBs have been investigated by performing surface state calculations on the (111) crystal plane of $BiSbTeSe_2$. In Fig.5.5(a) bands (red) of 6QL slab structure with Se1 terminated face are plotted along the M-Γ-K direction of the surface BZ. It can be seen that two

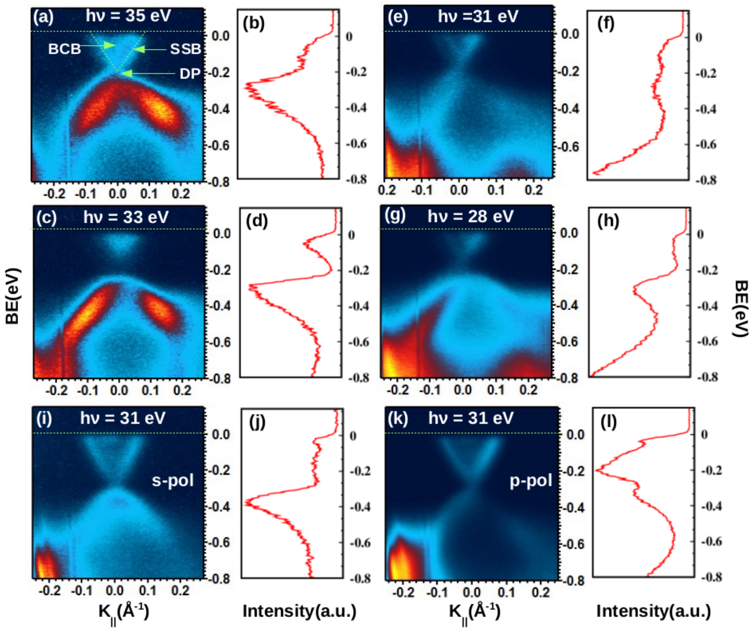

Figure 5.3: (a), (c), (e) and (g) correspond to the near E$_f$ ARPES images taken at photon energy 35, 33, 31 and 28 eV respectively. (b), (d), (f) and (h) show EDC spectra corresponding to the images in (a), (c), (e) and (g) respectively. Intensity map using s and p-polarized photon energy of 31 eV are shown in (i) and (k) respectively. EDC spectra of these images are shown in (j) and (l) respectively.

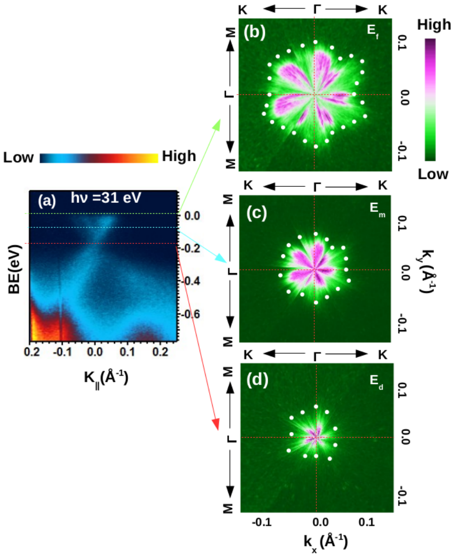

Figure 5.4: (a) correspond to near E$_f$ ARPES images taken at photon energy 31 eV. In (b) and (d) constant energy contour (CEC) are presented at binding energy E$_f$ and E$_d$ respectively, while (c) corresponds to CEC plotted at mid point energy(E$_m$) between the E$_f$ and E$_d$ taken at 31 eV photon energy.

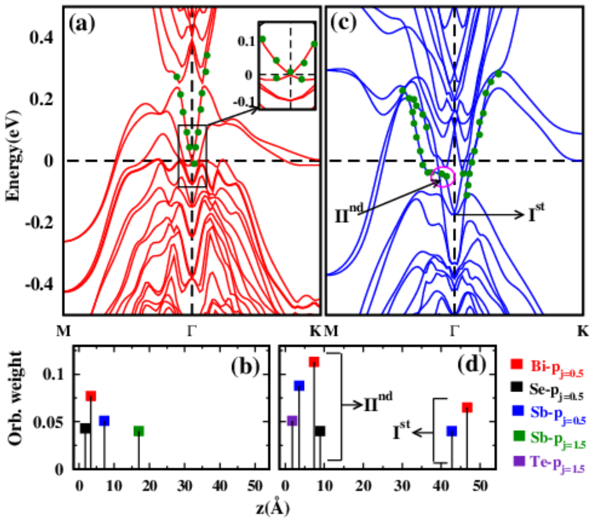

Figure 5.5: (a) and (c) show calculated bands of Se1 and Te terminated face of 6QL slab geometry of $BiSbTeSe_2$ respectively. (b) Weight of atomic orbitals mainly contributing to the 'V' shaped band (enclosed in the black box) at the Γ point in Se terminated plain with respect to their distances from the surface. (d) Similar contribution to V shaped band at the Γ point(I^{st}) and slightly away from the Γ point(II^{nd}) in Te terminated face.

bands falling into the shape of 'V' are observed just above the E_f around the Γ point. Here, green dots represent the orbital contribution coming from the atoms present in the topmost QL. Crossing of these Dirac like SSBs occurring at E_f is more clearly visible in the inset. In order to figure out the origin of these 'V' shaped bands, orbital projection weight of majorly contributing atoms to these bands at the Γ point with respect to their distances from the surface (z) are plotted in Fig.5.5(b). Fig.5.5(b) shows clearly that the orbital character originates primarily from the atoms close to the surface rather than the bulk region and the same character also persists in the nearby k-points of the Γ point. This further confirms the surface state nature of these bands. These results show a qualitative similarity to the previously reported SSBs of $BiSeTe_2$ [26]. The 'V' shaped bands show a high resemblance to the intensity pattern of SSBs observed in the ARPES data (Fig.5.3(a)), though there is slight mismatch in the Fermi position. The mismatch is possibly due to the intrinsic n-doping in the sample which raises the E_f level in the experimental data. The other possibility of Te terminated surface has also examined and bands (blue) of 6QL slab of this geometry are shown in Fig.5.5(c). In this case, the 'V' shaped band around the Γ point (I^{st} region) deviates from linearity as it moves away from the Γ point (II^{nd} region) and its position is quite below the E_f, unlike the case of Se terminated face (Fig.5.5(a)). In addition, the orbital weight of these bands at region I^{st} and II^{nd} are dominated by atomic orbitals placed in the bulk and surface sites respectively as is clear from the Fig.5.5(d). Probably, this large mixing of bulk and surface character leads to the deviation in the dispersion of this band. This contrary origin of the 'V'

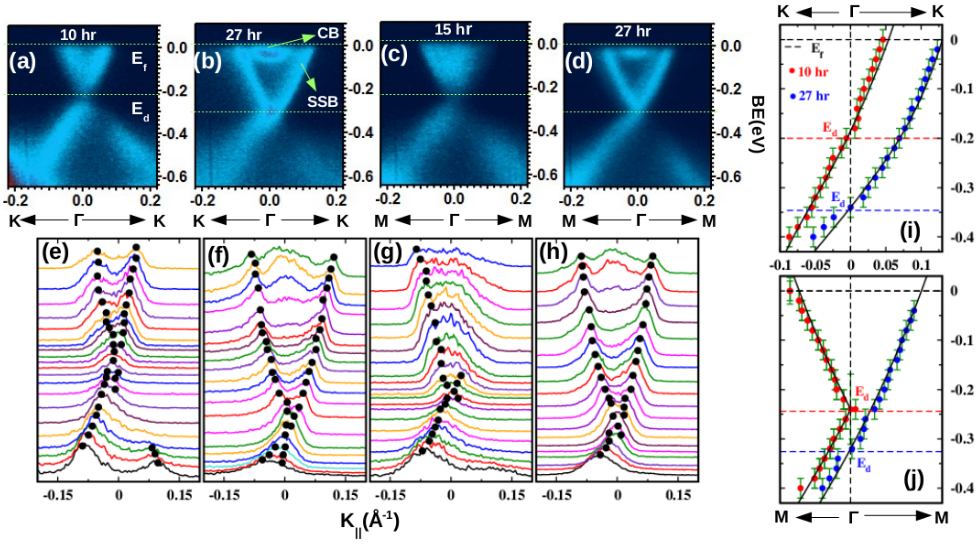

Figure 5.6: (a) and (b) depict the ARPES intensity plots taken at 31 eV photon energy along the Γ-K direction taken ∼ 10 and 27 hrs. after the sample cleaving. (c) and (d) show same images along Γ-M direction collected at different time intervals from the cleaving. (e)-(h) show MDC spectra extracted from the images (a)-(d). The dispersion relation between E and k estimated from the MDC plots are fitted to the calculated values obtained from the model Hamiltonian [32] along the Γ-K (i) and the Γ-M (j) directions.

shaped band around the Γ point, which are bulk and surface originated in Te and Se terminated face respectively, signifies that the SSBs are sensitive to the atomic composition of the surface.

As mentioned before, the tunability of the DP within the bulk band gap of the system is an advantage of BSTS important from the technological point of view which could be achieved by chemical doping. Intimately related to this is the observed gradual shifting of the DP with adsorption of gases or even the elapse of time in ultra high vacuum after the crystal cleaving. This shifting of DP is caused by the band bending effect which has been observed previously in various TIs, like Bi_2Se_3, Bi_2Te_3 [30, 31]. We present our observations of BB effects on the SSBs in Fig.5.6, where 5.6(a) and (b) show ARPES images along the Γ-K direction collected ∼ 10 and 27 hours after the cleaving. As can be seen from Fig.5.6(b), a significant shift of ∼ 0.14eV is observed in the position of E_d in comparison to that in Fig.5.6(a). Further, the filled CB states in the nearby E_f region around the Γ point are clearly demarcated from the SSBs and an arc shaped structure is seen in these CB states which could be a signature of the states of two dimensional electron gas (2DEG) character arising due to the strong BB effect, like in Bi_2Se_3 [30]. Similarly, shift of E_d and appearance of distinct SSBs and CB states can also be found in the ARPES images Fig.5.6(c) and (d) which were collected along the Γ-M direction at different time intervals after the cleaving. Fig.5.6(e)-(h) show plots of momentum density curves (MDC) extracted from the ARPES images of Fig.5.6(a)-(d) respectively, where the linear dispersion of MDC peaks is clearly

Table 5.1: Parameters of calculated SSBs obtained after fitting with the E-k dispersion relation(Eq.5.1) estimated from the ARPES data along the Γ-K and the Γ-M directions.

		Γ-K		
Time(hr.)	1/2m*(eV.Å^3)	ν_0(eV.Å)	α(eV.Å^3)	λ(eV.Å^3)
10	7	3.0	5	130
27	1.8	1.8	5	80
		Γ-M		
15	5	2.85	5	-
27	4	2.65	5	-

seen. An energy dispersion relation of the SSBs can also be obtained from the model Hamiltonian approach proposed by Fu [32] from the following relation.

$$\begin{aligned} E_{\pm}(\vec{k}) &= E_0(k) \pm \sqrt{\nu_k^2 k^2 + \lambda^2 k^6 cos^2(3\theta)} \\ \text{here, } E_0 &= k^2/(2m^*) \quad ; \quad \nu_k = \nu_0(1+\alpha k^2) \end{aligned} \tag{5.1}$$

where E$_{\pm}$ corresponds to the energy of the upper and lower band, E$_0$(k) generates particle-hole asymmetry, m* denotes effective mass, and θ indicates the azimuthal angle of momentum $\vec{k}$ with respect to the x-axis(Γ-M direction). λ is a parameter for the hexagonal warping. ν_0 is Dirac velocity which is modified to ν_k after including a second order correction parameter(α) to the Dirac velocity in the k.p Hamiltonian. The peak positions measured from the MDC plots along the Γ-K and Γ-M directions are fitted to the E-k dispersion relation of the SSBs obtained from the Eq.5.1 in Fig.5.6(i) and (j) respectively. The calculated bands nicely fit near the DP while a slight deviation can be seen in the regions away from the DP where the states of BVB and BCB are predominant. Parameters used for the fitting are tabulated in Table5.1 which shows that ν_0 reduces significantly along the Γ-K direction after 27 hrs. from the cleaving in comparison to the 10 hrs. cleaving case. On the other hand, warping strength, defined as $\sqrt{\lambda/\nu_0}$ remains almost constant under the influence of BB effects. The estimated value of warping strength($\sqrt{\lambda/\nu_0}$ = 6.8) is intermediate between the value found in Bi$_2$Se$_3$ and Bi$_2$Te$_3$ [33] (Further results on warping of the FS and constant energy counters (CES) can be found in section-1 of supplementary note). This result clearly establishes that FS warping and associated out of plane spin polarization can be controlled by the ratio of chalcogen/pnictogen atoms in Bi/Sb based TIs.

Further experiments were performed to understand the BB effect by using laboratory HeI (21.2 eV) photon source in combination with Scienta R3000 electron energy analyzer and results are demonstrated in Fig.5.7(a), (b) and (c). The ARPES intensity maps in these figures are taken at

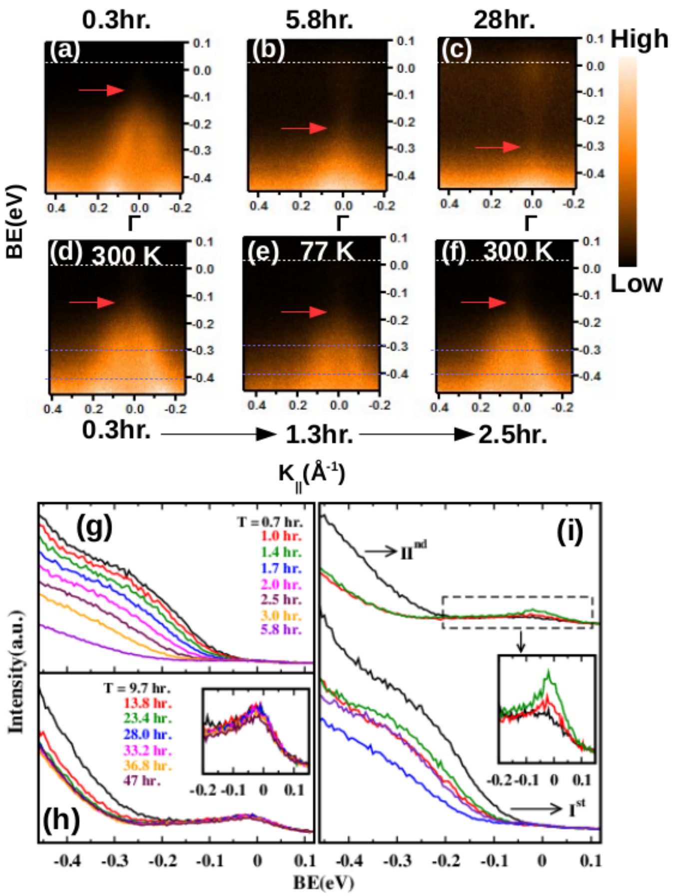

Figure 5.7: (a)-(c) ARPES intensity plots around Γ point at different time periods after the cleaving. (d)-(f) ARPES images of thermal cycling 300 K-77 K-300 K. In (g) and (h) EDC spectra are plotted extracted in a small window around the Γ point from the ARPES images collected at different time scale after the cleaving. Similar EDC plots obtained from the ARPES images of thermal cycling like (d)-(f) are presented in (i). The inset of Fig.5.7 (h) and Fig.5.7 (i) show the spectral weight evolution of the near E$_f$ states.Different colours (black → red → green → blue → magenta) of the EDC spectra represent various stages (300 K → 77 K → 300 K → 77 K → 300 K) of thermal cycling respectively.

0:30, 5:30 and 28:00 hrs. after the crystal cleaving. A clear downward shifting is observed of the BVB maximum (red arrow) as time elapses after the cleaving. Though, the intensity of SSBs is not pronounced just after the cleaving, it starts appearing in a gradual manner with time and becomes distinct in Fig.5.7(c). This temporal evolution is clearer in Fig.5.7(g) and (h), where energy density curve(EDC) spectra taken in a small energy window($\pm$ 0.02 Å^{-1}) around the Γ point at different time intervals after the cleaving are plotted. It is evident from these plots that the states decrease steadily as time passes after the cleaving and saturate around the time scale of 24 hr. In the inset of Fig.5.7(h) the spectral weight evolution of the near E$_f$ states can be seen coming from the filled BCB states. It has been previously proposed that the BB in TIs originate from accumulation of additional charges at the surface. These extra charges arise due to Se vacancies present in the bulk as well as those created at the surface in the process of surface cleaving [34,35]. On the top of that, adsorption of residual gases further change the charge distribution at the surface [10–12]. In order to confirm the role of adatoms in the BB effect, spectra were collected in a cycle of temperatures, 300 K-77 K-300 K. Since, the adsorption of residual gases is faster at low temperatures the effect of BB is supposed to be enhanced at low temperatures. This view is fairly supported by our ARPES data taken at 77 K (Fig.5.7(e)) where a shifting of the BVB towards higher BE in comparison to the initial 300 K data (Fig.5.7(d)) is observed. This again retreats towards its previous position as sample heats upto the room temperature (Fig.5.7(f)). This result of thermal cycling was cross checked by repeating it at different time intervals after the cleaving. EDC spectra of such two set of cycles performed at 0:30 and 24:00 hrs. after the cleaving are presented in Fig.5.7(i). In the Ist cycle, 77 K (red) spectra show a substantial lowering with respect to the 300 K (black) spectra which partially recover with annealing to 300 K (green). The same behavior of down and up-swings continue in next 77 K (blue) and 300 K (indigo) measurements too. The IInd set of cycle also shows a large reduction of spectral weight at 77 K (red) compared to the 300 K (black) spectra. However, states are not enhanced much while the sample anneals to 300 K which could be related to inadequate desorption of the adatoms.

To further investigate the role of adatoms on the BB, thermal cycle experiments were performed under constant exposure of Ar, N_2 and O_2 gases. In first panel, Fig.5.8(a), (b) and (c) show ARPES images taken at 300 K-77 K-300 K respectively just after the cleaving (Ist thermal cycle) in the Ar environment. Similarly, second (Fig.5.8(d)-(f)) and third (Fig.5.8(g)-(i)) panels display ARPES images of the Ist thermal cycle performed under constant dosing of N_2 and O_2 gases respectively. In Fig.5.8(b), a marginal shifting of the BVB maximum (marked with red arrow) is observed towards the E_f, though it was recorded at a later time in comparison to Fig.5.8(a). This result of BB effect is contrary to the behavior observed under the ultra high vacuum conditions (Fig.5.7(e)). It indicates that the Ar adatoms act like an electron acceptor compensating the Se vacancy induced downward BB and thereby lead to a small upward shifting of the BVB. This inference is supported by the relatively large downward shifting of the BVB due to the gas desorption in the next 300 K annealed data (Fig.5.8(c)). These changes are more clearly visible in the higher BE region (between the two red dotted lines). Similar characteristics of hole doping are also seen in the exposure of N_2 gas (Fig.5.8(d)-(f)). However, the dosing of O_2 gas gives rise to a completely opposite BB effect *i. e.* features of n-doping as clear from Fig.5.8(g)-(i). Further, in this case, a faint feature of the SSs appear quite early at the top of BVB, unlike the other gas exposure cases after the cleaving. This probably is linked to the higher adsorption of O_2 gas which accelerates the BB effect. These changes are also compared in the EDC (taken around the Γ point of k width $\pm$ 0.02 Å^{-1}) plots Fig.5.8(j), (k) and (l) which correspond to panel first, second and third respec-

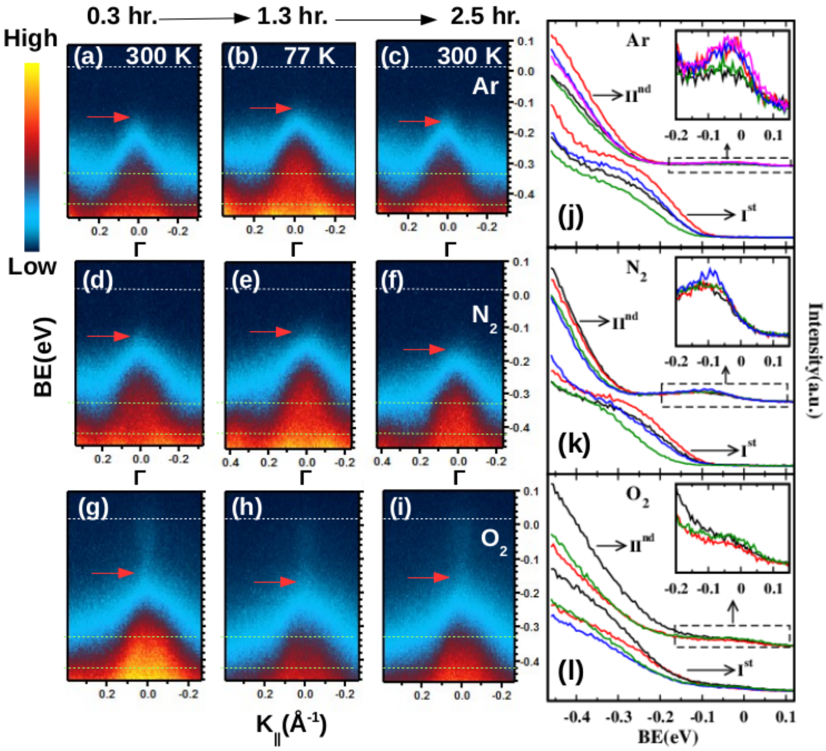

Figure 5.8: (a), (b) and (c) ARPES images taken at 300 K-77 K-300 K respectively just after the cleaving(I^{st} thermal cycle) in Ar environment. (d)-(f) and (g)-(i) display ARPES images of the I^{st} thermal cycle performed under constant dosing of N_2 and O_2 gases respectively. (j), (k) and (l) correspond to EDC(taken around the Γ point) plots of thermal cycling under the exposure of Ar, N_2 and O_2 gases respectively, where the inset of each plots show the enlarged view of the near E_f region. Different colours (black → red → green → blue → magenta) of the EDC spectra represent various stages (300 K → 77 K → 300 K → 77 K → 300 K) of thermal cycling respectively.

tively. Data sets of thermal cycling performed ∼ 0:30 and 24:00 hrs. after the cleaving are marked Ist and IInd respectively. In Fig.5.8(j), a sharp reduction is observed in the intensity of initial 300 K spectra (black) in comparison to the 77 K spectra (red) which again raise and fall at next 77 K (blue) and 300 K (green) data respectively. Similar behavior is reproduced at the IInd set of thermal cycling. In addition, spectral weight enhancement is also found originating from the filled BCB states in the vicinity of E_f as shown in the inset. Thermal cycling trend of the EDC spectra of N_2 case (Fig.5.8(k)) qualitatively matches with the Ar exposure case. Whereas, EDC plots of the O_2 exposure case (Fig.5.8(l)) show a contrary nature in comparison to the Ar dosing case. The small recovery of annealed 300 K (green) spectra with respect to the 77 K (red) in the IInd set of cycle could possibly be a signature of incomplete desorption of the O_2 gas.

It was reported that in the binary TI Bi_2Se_3 the DP moves by 116 meV from its initial position just after cleaving to a saturation value under the influence of BB effects [9]. Our own measurements also showed a shifting of ∼ 0.1 eV in time scale of 11:00 hr. after the sample cleaving in Bi_2Se_3. It is interesting to note that this movement is substantially lesser in comparison to the BSTS where it is ∼ 0.2 eV in similar time scale and experimental conditions. Recent studies on Bi_2Se_3 have shown that not only the extra charges at the surface but also its periodic re-arrangement inside the bulk creates a Coulomb potential of long ranged order contributing to the BB effect [35]. This unique property is inherent to the layered structure of Bi_2Se_3 where charge is accumulated and depleted at both ends of each QLs. Introduction of additional elements (Sb and Te) in the QL of BSTS lead to an asymmetry in the structure of the QL compared to the Bi_2Se_3. The presence of Te atoms in addition to the Se atoms at the terminating faces of the QL structure in $Bi_{1.5}Sb_{0.5}Te_{1.7}Se_{1.3}$ have been observed in STM measurements [16]. This could possibly provide different screening to the surface charges compared to the Bi_2Se_3. So an oscillatory behavior of charge density could persist at larger distances inside the bulk region and result in a Coulomb potential of higher and longer range giving rise to the stronger BB in BSTS in comparison to the Bi_2Se_3. Our experimental observations, stronger BB and lower DP position in BSTS compared to Bi_2Se_3, are consistent with ARPES results on a similar composition $Bi_{1.5}Sb_{0.5}Te_{1.7}Se_{1.3}$ reported by Golden *et. al.* [36]. These authors have also attributed the effective screening of the adsorbate-induced surface charge for different temporal evolution of the SSBs in $Bi_{1.5}Sb_{0.5}Te_{1.7}Se_{1.3}$ and Bi_2Se_3 compounds. In addition, they suggested different composition of the terminated face between the two compounds could also influence the sticking process of the residual gas atoms thereby leading to different BB behaviour. This argument is supported by our first principles results where we find that the nature of SSBs are different between the slab geometry of Se and Te termination(Fig.5.5). Besides this, another factor affecting the BB process could be the difference in the relaxation process of the exposed surface between the two compounds. However, in case of Bi_2Se_3 Hofmann *et. al.* have ruled out any surface lattice relaxation using their LEED study [30].

5.4 Conclusion

In conclusion, we discussed the results of our experimental studies using ARPES and first principle based Quantum Espresso band structure calculations and confirmed the non-trivial topology of the SSBs in BSTS. Our calculations show that the SSBs are sensitive to the atomic composition of the terminating surface and our experimental data shows that they have a partial 3D character. We have undertaken a detailed study of the shifting of the DP by the BB effect with elapse of time as well as adsorption of gases after the crystal cleaving. We find that under the BB effect the DP in BSTS shifts by more than two times compared to that in Bi_2Se_3 to reach the saturation. Our results suggest that the stronger BB in BSTS could be due to the difference in screening of the surface charges because of the different compositions of the QLs of the two compounds. From the MDCs of the ARPES data we obtained an energy dispersion relation showing the warping strength of the Fermi surface in BSTS to be intermediate between those found in Bi_2Se_3 and Bi_2Te_3 and also is tunable by the ratio of chalcogen/pnictogen atoms. Further experiments reveal that the nature of the BB effects are highly sensitive to the exposure of the fresh surface to various gas species; Ar and N_2 show signatures of hole doping while O_2 shows those of electron doping. Our findings could have importance in the tuning of Dirac point in topological insulators especially the members of the BSTS family for technological applications.

Bibliography

[1] M. Z. Hasan and C. L. Kane, *Rev. Mod. Phys.*, **82**, (2010), 3045.

[2] Xiao-Liang Qi and Shou-cheng Zhang, *Rev. Mod. Phys.*, **83**, (2011), 1057.

[3] Y. Xia, D. Qian, D. Hsieh, L.Wray, A. Pal, H. Lin, A. Bansil, D. Grauer, Y. S. Hor, R. J. Cava and M. Z. Hasan *Nat. Phys.*, **5**, (2009), 398.

[4] Xiao-Liang Qi, Rundong Li, Jiadong Zang, Shou-Cheng Zhang, *Science*, **323**, (2009), 1184.

[5] Liang Fu and C. L. Kane, *Phy. Rev. Lett.*,,**100**, (2008), 096407.

[6] David Hsieh, Y Xia, L Wray, Dong Qian, A Pal, JH Dil, J Osterwalder, F Meier, G Bihlmayer, CL Kane, YS Hor, RJ Cava, M Zahid Hasan, *Science*, **323**, (2009), 919.

[7] Liang Fu and C. L. Kane, *Phy. Rev. Lett.*, **102**, (2009), 216403.

[8] A. R. Akhmerov, Johan Nilsson, and C.W. J. Beenakker, *Phy. Rev. Lett.*, **102**, (2009), 216404.

[9] Z.-H. Zhu, G. Levy, B. Ludbrook, C. N. Veenstra, J. A. Rosen, R. Comin, D. Wong, P. Dosanjh, A. Ubaldini, P. Syers, N. P. Butch, J. Paglione, I. S. Elfimov, and A. Damascelli, *Phy. Rev. Lett.*, **107**, (2011), 186405.

[10] P. D. C. King, R. C. Hatch, M. Bianchi, R. Ovsyannikov, C. Lupulescu, G. Landolt, B. Slomski, J. H. Dil, D. Guan, J. L. Mi, E. D. L. Rienks, J. Fink, A. Lindblad, S. Svensson, S. Bao, G. Balakrishnan, B. B. Iversen, J. Osterwalder, W. Eberhardt, F. Baumberger, and Ph. Hofmann, *Phy. Rev. Lett.*, **107**, (2011), 096802.

[11] Hadj M. Benia, Chengtian Lin, Klaus Kern, and Christian R. Ast, *Phy. Rev. Lett.*, **107**, (2011), 177602.

[12] D. Hsieh, Y. Xia, D. Qian, L. Wray, J. H. Dil, F. Meier, J. Osterwalder, L. Patthey, J. G. Checkelsky, N. P. Ong, A. V. Fedorov, H. Lin, A. Bansil, D. Grauer, Y. S. Hor, R. J. Cava and M. Z. Hasan, *Nat. Lett.*, **460**, (2009), 1101.

[13] Zhi Ren, A. A. Taskin, Satoshi Sasaki, Kouji Segawa, and Yoichi Ando, *Phy. Rev. B.*, **82**, (2010), 241306(R).

[14] Zhi Ren, A. A. Taskin, Satoshi Sasaki, Kouji Segawa, and Yoichi Ando, *Phy. Rev. B*, **84**, (2011), 165311.

[15] Yang Xu, Ireneusz Miotkowski, Chang Liu, Jifa Tian, Hyoungdo Nam, Nasser Alidoust, Jiuning Hu, Chih-Kang Shih, M. Zahid Hasan and Yong P. Chen, *Nat. Physics*, **10**, (2014), 956.

[16] Wonhee Ko, Insu Jeon, Hyo Won Kim, Hyeokshin Kwon, Se-Jong Kahng, Joonbum Park, Jun Sung Kim, Sung Woo Hwang and Hwansoo Suh, *Sci. Rep.*, **3**, (2013), 02656.

[17] Haijun Zhang, Chao-Xing Liu, Xiao-Liang Qi, Xi Dai, Zhong Fang and Shou-Cheng Zhang, *Nat. Phy.*, **5**, (2009), 438.

[18] T. Arakane, T. Sato, S. Souma, K. Kosaka, K. Nakayama, M. Komatsu, T. Takahashi, Zhi Ren, Kouji Segawa and Yoichi Ando, *Nat. Comm.*, **3**, (2011), 636.

[19] M. Neupane, S.-Y. Xu, L. A. Wray, A. Petersen, R. Shankar, N. Alidoust, Chang Liu, A. Fedorov, H. Ji, J. M. Allred, Y. S. Hor, T.-R. Chang, H.-T. Jeng, H. Lin, A. Bansil, R. J. Cava, and M. Z. Hasan, *Phy. Rev. B*, **85**, (2012), 235406.

[20] Bin Liu, Wuyuan Xie, Han Li, Yanrong Wang, Daoping Cai, Dandan Wang, Lingling Wang, Yuan Liu, Qiuhong Li and Taihong Wang, *Sci. Rep.*, **4**, (2014), 04639.

[21] Giannozzi P. et al. *http:/www.quantum-espresso.org*.

[22] Perdew J P,Burke K and Ernzerhof M, *Phys. Rev. Lett.*, **77**, (1996), 3865.

[23] Perdew J P and Wang Y, *Phys. Rev. B*, **45**, (1992), 13244.

[24] Perdew J P, Chevary J A, Vosko S H, Jackson K A, Pederson M R, Singh D J and Fiolhais C, *Phys.Rev. B*, **46**, (1992), 6671.

[25] Vanderbilt D Soft self-consistent pseudopotential in a generalized eigenvalue formalism, *Phys. Rev. B*, **41**, (1990), 7892.

[26] Xian-Qi Dai, Bao Zhao, Jian-Hua Zhao, Yan-Hui Li, Ya-Nan Tang and Ning Li, *J. phys. condens. matt.*, **24**, (2012), 035502.

[27] Black-Schaffer M. A. and Balatsky V. A. *Phy. Rev. B*, **85**, (2012), 121103(R)1-4.

[28] J. Sanchez-Barriga, A. Varykhalov, G. Springholz, H. Steiner, R. Kirchschlager, G. Bauer, O. Caha, E. Schierle, E. Weschke, A.A. U nal, S. Valencia, M. Dunst, J. Braun, H. Ebert,

J. Minar, E. Golias, L.V. Yashina, A. Ney, V. Holy and O. Rader *Nat. Comm.*, **7**, (2016), 10559-10.

[29] Y. L. Chen, J. G. Analytis, J.-H. Chu, Z. K. Liu, S.-K. Mo, X. L. Qi, H. J. Zhang, D. H. Lu, X. Dai, Z. Fang, S. C. Zhang, I. R. Fisher, Z. Hussain, Z.-X. Shen, *Science*, **325**, (2009), 178.

[30] Marco Bianchi, Dandan Guan, Shining Bao, Jianli Mi, Bo Brummerstedt Iversen, Philip D.C. King and Philip Hofmann, *Nat. Comm.*, **1**, (2010), 128.

[31] D. Hsieh, Y. Xia, D. Qian, L. Wray, F. Meier, J. H. Dil, J. Osterwalder, L. Patthey, A.V. Fedorov, H. Lin, A. Bansil, D. Grauer, Y. S. Hor, R. J. Cava, and M. Z. Hasan, *Phy. Rev. Lett.*, **103**, (2009), 146401.

[32] Liang Fu, *Phy. Rev. Lett.*, **103**, (2009), 266801.

[33] M. Nomura, S. Souma, A. Takayama, T. Sato, T. Takahashi, K. Eto, Kouji Segawa, and Yoichi Ando, *Phy. Rev. B*, **89**, (2014), 045134.

[34] P Rakyta, B Ujfalussy and L Szunyogh, *New. J. Phys.*, **17**, (2015), 123011.

[35] T. Forster, P. Kruger and M. Rohlfing, *Phy. Rev. B*, **91**, (2015), 035313.

[36] E. Frantzeskakis, N. de Jong, B. Zwartsenberg, T. V. Bay, Y. K. Huang, S. V. Ramankutty, A. Tytarenko, D. Wu, Y. Pan, S. Hollanders, M. Radovic, N. C. Plumb, N. Xu, M. Shi, C. Lupulescu, T. Arion, R. Ovsyannikov, A. Varykhalov, W. Eberhardt, A. de Visser, E. van Heumen, and M. S. Golden, *Phy. Rev. B*, **91**, (2015), 205134-15.

Chapter 6

Fermi Surface and Band Structure of BiPd from ARPES Studies

In the continuation to our work on electronic structure study of Bi based materials, we explored the Fermi surface and band structure of BiPd using ARPES and DFT calculations. Results of these studies are described in this chapter. Although, BiPd has a layered structure similar to other topologically insulating compounds presented in chapter 4 and 5, it shows both superconducting and topological nature. Our findings suggest that BiPd could be a s-wave multiband superconductor.

6.1 Introduction

An upsurge has been witnessed recently in the search for novel materials after realizing the significant role of spin-orbit coupling (SOC) effects in the modification of near Fermi level (E_f) electronic structure of materials and thereby their physical properties. For example, presence of a strong SOC produces conducting edge states in topological insulators (TIs) [1, 7]. Similarly, intertwining of the spin-orbit interaction with non-centrosymmetric (NCS) structures gives rise to some exotic phenomena of mixing up of spin-singlet and triplet Cooper pairing channels [3, 4] in superconductors (SCs). The anomalous value of upper critical field (H_{c2}) [6, 6], presence of Majorana surface states at the junction of superconducting transition temperature (T_c) [7, 8] and existence of Weyl fermion surface states in Weyl semimetals [9] are a few more interesting properties related to the NCS structures behaving under SOC effects. These new class of materials not only present intriguing physics but also have tremendous scope in various applications.

One of the interesting aspects of the NCS crystals is a broken inversion symmetry that gives rise to antisymmetric spin-orbit interaction (ASOC) which has been theoretically predicted to form an unconventional pairing in the NCS SCs. However, most of the NCS SCs, like $Mg_{10}Ir_{19}B_{16}$ [10], Mo_3Al_2C [11], $Re_{24}Nb_5$ [12], Re_3W [13] show conventional s-type superconducting behavior which is attributed to the weak SOC in these compounds. The pairing mechanism becomes quite complex due to strong electron correlation effects in some other SCs of the NCS family, like $CePt_3Si$ [14], UIr [15]. In this scenario, discovery of superconductivity in NCS compound BiPd has brought some new excitement to this field due to the presence of heavy elements Bi (Z = 83) and Pd (Z = 46) SOC is expected to be strong while electronic correlation is moderate in this compound as suggested by Kadowaki-Woods value estimated from resistivity measurements [16]. Therefore, it provides an excellent ground to study the role of SOC effects in the electronic structure of NCS SCs. BiPd shows a transition from orthorhombic (β-BiPd) to monoclinic (α-BiPd) structure at 210°C and its T_c is $\sim$ 3.7 K [17, 18]. Various measurements, like electrical resitivity, magnetic susceptibility and heat capacity helped in establishing a s-wave type BCS superconductivity in this system [17,19]. However, mixing of spin-singlet and triplet order parameter, signature of multigap and Andreev bound states have also been identified from Andreev spectroscopic measurements [20]. Spin-triplet component has also been seen in the nuclear quaderpole resonance (NQR) measurements [21]. Similarly, London penetration depth and its corresponding superfluid density showed an anisotropy with two energy gaps which was further attributed to the mixing of the two pairing states in BiPd [22]. But, so far, there is no consensus reached on the role of ASOC induced spin-triplet pairing in the formation of Cooper pairs. Further, another promising feature, a Dirac cone like surface states has been observed recently in angle resolved photoemission spectroscopy (ARPES) study by Hasen *et al.* [23]. This non-trivial topological character in the superconducting state may pave the path for experimental realization of Majorana states in this system.

Till date there are very few experimental photoemission studies reported on BiPd [23–25] which is mainly focused on the surface state bands. In this chapter, our aim is to investigate the near E_f electronic structure of BiPd by using ARPES measurements and discuss these results in detail along with our calculations based on density functional theory (DFT). We observe a high intensity distribution on the Fermi surface (FS) resulting from various electron and hole like bands present in the vicinity of E_f. These near E_f states are composed primarily of Bi-6p with a little admixture of Pd-$4d_{x^2-y^2/zy}$ orbitals. The FS mainly consists multi sheets of three dimensions (3D) which are due to several spin-orbit splitted bands crossing the E_f. This 3D character does not favor the nesting between the different sheets of FS and weakens the possibility of any density wave instabilities in this system. Our results emphasize that the pairing could be a spin-singlet nature mediated by the phonons in BiPd.

6.2 Details of experiment and calculation

A high quality single crystal of BiPd was synthesized via self flux melt growth technique. Stoichiometry was confirmed by using X-ray diffraction measurements. Results of the structural and other physical characterizations have been reported earlier [16]. Photoemission spectra were collected in angle resolved mode by using a hemispherical SCIENTA-R3000 analyzer and a monochromatized He source (SCIENTA-VUV5040). The photon flux was of the order of 10^{16} photons/s/steradian with a beam spot of 2 mm in diameter. Fermi energy for all measurements were calibrated by using a freshly evaporated Ag film on to the sample holder. The total energy resolution, estimated from the width of the Fermi edge, was about 27 meV for the He-I excitation. Measurements were performed at a base pressure of $\sim 2.0 \times 10^{-10}$ mbar at temperature 77 K. A fresh surface of the sample was prepared by *in-situ* cleaving using post-technique method in the preparation chamber at base pressure of 5.0×10^{-10} mbar and the spectra were taken within 4.0 hour, so as to avoid any surface degradation. All the measurements were repeated many times to ensure the reproducibility of the data.

First-principles calculations were performed by using a plain wave basis set inherent in Quantum Espresso(QE) [20]. Many electron exchange-correlation energy was approximated by Perdew-Burke-Ernzerhof (PBE) functional [21–23]. Both fully relativistic ultrasoft [24] and non relativistic norm-conserving pseudopotentials were used in the calculations in order to see the SOC effects. Fine mesh of k-points with Gaussian smearing of the order 0.0001 Ry was used for sampling the Brillouin zone integration, and kinetic energy and charge density cut-off were set to 100 Ry and 500 Ry respectively. Experimental lattice parameters and atomic coordinates of α-BiPd [18], after relaxed under damped (Beeman) dynamics with respect to both ionic coordinates and the lattice vector, were employed in the calculations. All parameters were optimized under several convergence tests.

6.3 Results and discussion

Fig.6.1(a) shows the crystal structure of α-BiPd, in which Bi (blue) and Pd (red) atoms are arranged in two adjacent double layers. The bonding between alternative layers is weak which makes the (010) plane good for cleaving. Bi(Pd) atoms are coordinated to Pd(Bi) atoms situated at seven nearest neighbour (nn) sites as shown in Fig.6.1(b). The average inter-atomic distance of Pd atoms (1-4) from the Bi atom is 2.85 Å while the Pd atoms 5 and 6 are at 2.89 Å apart. Similarly, Pd atom 7 placed on the adjacent double layer is separated by 2.88 Å from the Bi atom.

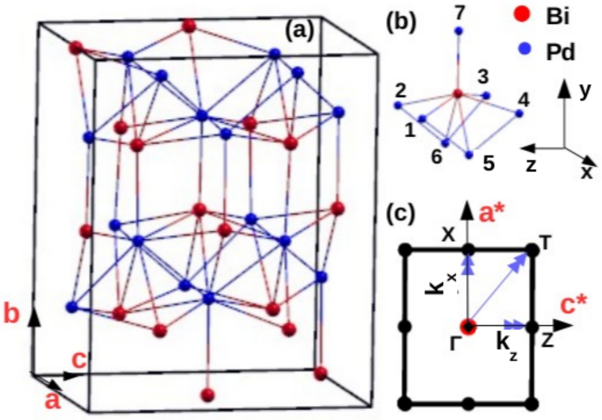

Figure 6.1: (a) Crystal structure of α-BiPd. (b) The coordination environment of Bi(Pd). (c) The 2D surface Brillouin zone of BiPd where Γ, Z, X and T are the high symmetry k-points and blue arrows denote the k-directions of band mapping.

Fig.6.1(c) present the 2D surface Brillouin zone (BZ), where the high symmetry k-points Γ, X, Z and T are shown along with blue arrows indicating the k-directions along which we performed our calculations.

Fig.6.2(a) shows the ARPES intensity map of the FS of BiPd on the Γ-Z plane. It can be clearly seen from this plot that intensity distribution varies significantly at different k-points and it is substantially less around the Γ point. This distribution gradually increases as we move along the Γ-Z direction and quite high intensity is observed around the Z point. The images of energy dispersion along different cuts from #1 to #3 are displayed in Fig.6.2(b)-(d) respectively. In Fig.6.2(b), a high intensity region can be found $\sim$ E_b = -0.7 eV and $k_{||}$ = -0.32 $Å^{-1}$ which rapidly disperses towards the higher binding energy as k approaches to the Γ point. Similarly, moderate intensity is observed near the E_f and around E_b = -0.5 eV which also shows a strong dispersion. Intensity gets modified remarkably along the other two cut directions (#2 and #3). Here, intense patches of intensity distribution can be found, particularly around the center k point in the vicinity of E_f in comparison to cut #1. Likewise, high intensity regions are also observed in many parts on the Γ-T plane of the FS as shown in Fig.6.2(e). Again, the intensity distribution is quite low around the Γ point, whereas it is moderate around T point. Band dispersion along cut #4 to #7 is displayed in Fig.6.2(f)-(i) respectively. In Fig.6.2(f), two parabolically dispersing bands can be viewed in the higher BE region (E_b = -0.7 to -1.1 eV). Similarly, places of high intensity are also observed close to the E_f $\sim$ k = ± 0.22 $Å^{-1}$. These intensity distributions evolve drastically on scanning the different cuts along the Γ-T direction. In the image of cut #5, bands are more intense in the BE range $\sim$ E_b = -0.2 to -0.6 eV relative to cut #4 and again become less intense in the next images collected along the cut #6 and #7. The observed high intensity distribution at various parts of both the FS

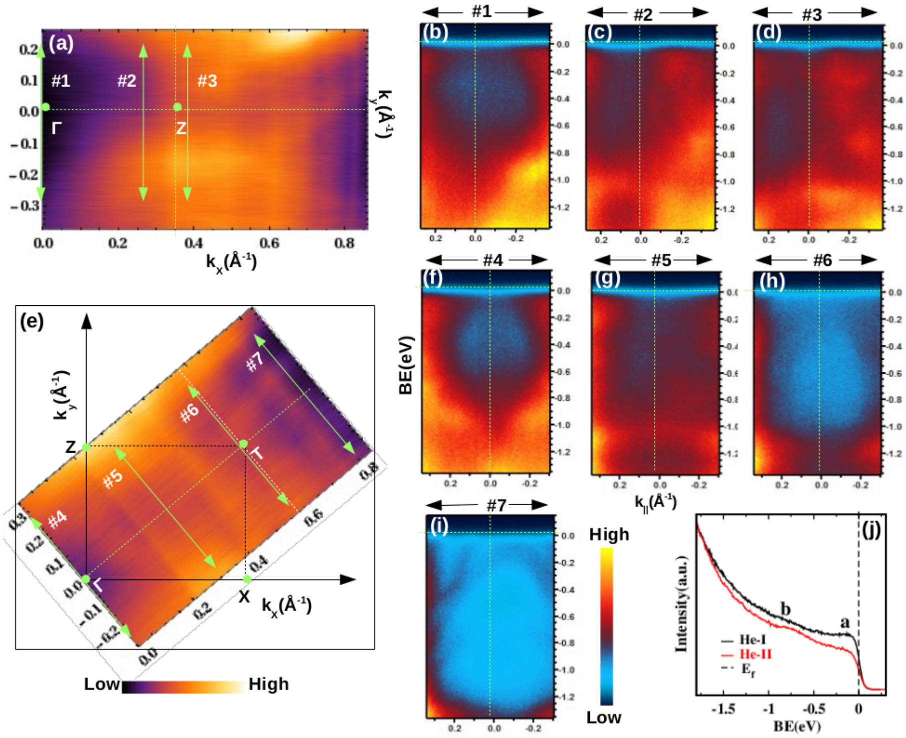

Figure 6.2: (a) and (e) ARPES intensity map of FS on Γ-Z and Γ-T plane respectively. (b)-(d) ARPES images of energy dispersion along different cuts #1 to #3 and (f)-(i) same images taken along cuts #4 to #7 respectively. (j) Comparison of angle integrated valence band spectra of BiPd collected at He-I(black) and He-II(red) photon energy.

plots, which results from the different electronic bands, confirms the good metallic character of BiPd. This observation is also consistent with the resistivity behavior of BiPd [17]. Broadening of the bands which lead to intensity patches in the energy dispersion plots could be an outcome of the large number of closely spaced bands which are not well resolved in these ARPES images or the sizable contribution coming from interlayer 3D coupling [31]. Nevertheless, the strongly dispersive nature of different intensity patterns indicate a weakly correlated character of BiPd. In order to elucidate the nature of the near E_f states a comparison of angle integrated valence band photoemission spectra are presented in Fig.6.2(j) taken at He-I (21.2 eV) and He-II (40.8 eV) photon energy respectively. In He-I spectra (Black), two features “a” and “b” are visible positioned close to the E_f and $\sim E_b$ = -0.9 eV respectively. This near E_f feature (a) is suppressed in He-II spectra (Red) while the intensity of the higher BE feature (b) is slightly enhanced in comparison to the He-I case. These changes in the spectral weight signify that the near E_f bands (a) could be mainly composed of Bi-6p whereas Pd-4d contribution is dominant in the higher BE feature (b) (atomic photoinoinization crosssections [28] of Bi-6p and Pd-4d are different for He-I to He-II).

In order to get a deeper insight into the underlying physics behind the near E_f bands, an enlarged view of this region in the Fig.6.2(b) and (d) are shown in Fig.6.3(a) and (b) respectively. Similarly, Fig.6.3(c), (d) and (e) correspond to the near E_f zoomed images of the Fig.6.2(f), (h) and (i) respectively. In these plots large spectral weight can be seen which indicates the presence of various bands crossing the E_f. In order to resolve these crossings of near E_f bands more clearly, images Fig.6.3(a)-(e) are renormalized by dividing their angular integrated spectrum and presented in Fig.6.3(f)-(j) respectively. In Fig.6.3(f) three bands can be identified; two of them hole like (α and β) and one electron like (δ). The apex of α band lies $\sim$ E_b = -0.28 eV at the Γ point while the band β crosses the $E_f \sim k_{||} = \pm\ 0.1$ Å^{-1} and leads to a hole pocket around the Γ point. On the other hand, small traces of the electron like band δ is found $\sim$ $k_{||}$ = 0.3 Å^{-1} which probably forms an electron pocket around the X point. Similarly, intensity distribution in the vicinity of the Z point (Fig.6.3(g)) shows the presence of a one electron like band around the Z point and a hole like band touching the E_f nearby the Z point. Whereas, along the Γ-T direction two hole like bands(α' and β'), similar to the bands along the Γ-X direction are observed around the Γ point as clear from the Fig.6.3(h). The apex of one band(α') is at higher BE ($E_b \sim$ -0.3 eV) while the other band(β'), which shows nearly a linear dispersion carves a hole pocket around the Γ point. This intensity pattern changes as traversing along this Γ-T direction as clear from the Fig.6.3(i) and (j) which correspond to ARPES images taken along the cut #6 and #7 respectively. Though, intensity of bands are not prominent along the cut #6, three hole like bands could be clearly seen along the cut #7. Two of them form hole pockets and the other band just touches the E_f. The difference in the band dispersion are also evident in plots of energy density curves (EDC) as shown in Fig.6.3(k)-(o) which are extracted from the ARPES images Fig.6.3(a)-(e) respectively. In these EDC plots, sufficient spectral weight is seen close to the E_f and its variation with respect to k differs along various cuts.

We also performed first principles calculations to better understand our ARPES findings. In Fig.6.4(a) non-relativistic band structure of BiPd is presented where four electron pockets (red, blue, green and magenta) and two hole pockets (orange and cyan) are found around the X and Γ points respectively. The dispersion of the near E_f bands are slightly modified along the Γ-T direction in comparison to the Γ-X direction, however, the number of electron and hole pockets remain same. On the other hand, along the Γ-Z direction, two almost degenerate (indigo and brown) hole like bands cross the E_f close to the Z point leading to small hole pockets around the Z point. Moreover, one tiny electron pocket can also be observed between the Γ and the Z point formed by the cyan band. To figure out the orbital character of these bands, orbital resolved DOS is calculated on the same k-space along which bands are obtained and smoothed by a Gaussian smearing. These results show that the DOS originate from Bi-6p and Pd-4d dominate the near E_f

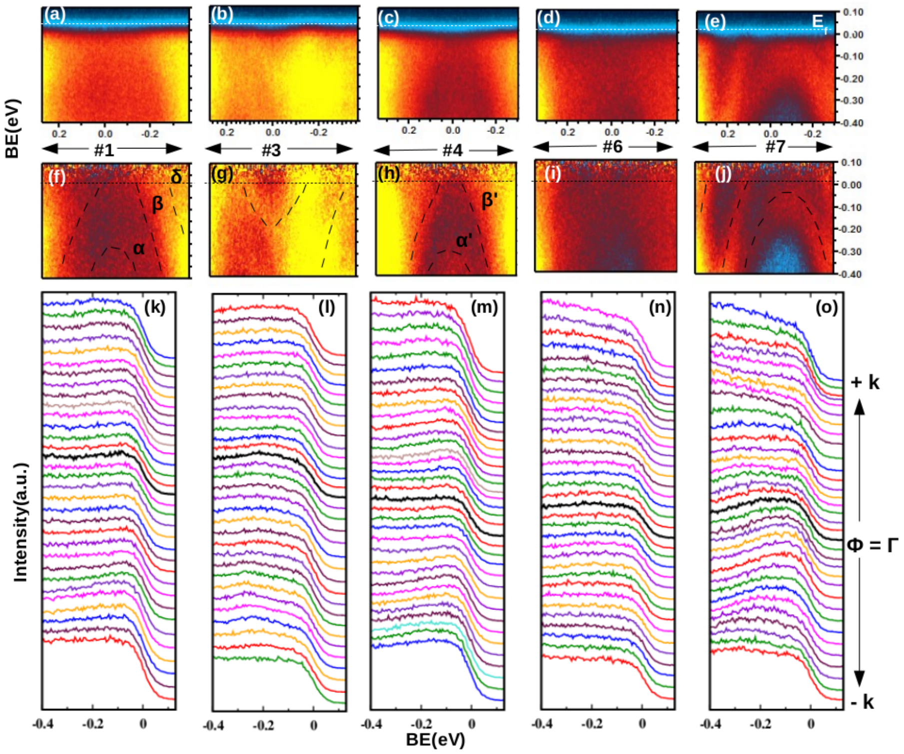

Figure 6.3: (a)-(e) show near E$_f$ region of ARPES intensity plot along cut#1, #3, #4, #6 and #7 and corresponding renormalized images(dividing by angular integrated spectrum) are shown in (f)-(j) respectively. (k)-(o) are plots of energy density curves(EDC) extracted from the images (a)-(e).

region and DOS of different 6p and 4d orbitals of individual Bi and Pd atoms are almost identical. So, in Fig.6.4(b) and (c) DOS of individual Bi-6p and Pd-4d orbitals integrating from all the Bi and Pd atoms are displayed. It can be clearly seen that Bi-p$_y$ contribution to the near E$_f$ states is quite large in comparison to Bi-p$_{x/z}$ as well as sufficient weight of Pd-d$_{zy/x^2-y^2}$(see the inset of Fig.6.4(c)) states are also present in this region. Comparing this plot to band picture, it is clear that the bands lying deeper in BE (E$_b$ $\sim$ -0.4 to -1.0 eV) red, blue and green (dashed line) and showing highly dispersive nature are mainly originated from different Bi-6p orbitals while bands E$_b$ $\sim$ -1.2 eV (dashed magenta and orange) are mainly formed by Pd-4d$_{x^2-y^2/zy}$ orbitals. These results of band characteristics are consistent with the changes seen in the experimental spectral features “a” and “b” as moving from He-I to He-II excitation energy Fig.6.2(j)). The electron pockets (red and blue) around the X point is dominated by Bi-6p$_x$ orbital while hole pockets (orange and cyan) around the Γ point are mainly composed of Bi-6p$_y$ orbital which is different from Bi-6p$_z$ character of hole pockets (indigo and brown) around the Z point. Similarly, the additional increment of Pd-4d$_{zy}$ and Pd-4d$_{zx}$ orbital character in the electron like bands around the T point is the possibly reason for modification of these bands in comparison to the same bands seen around the X point. These different nature of the near E$_f$ bands, which are predominant by different Bi-6p orbitals

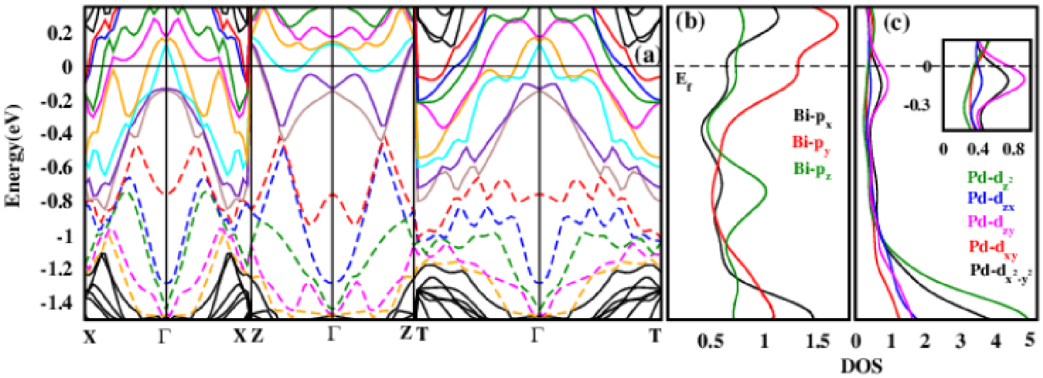

Figure 6.4: (a) Band structure plot of BiPd obtained from non relativistic calculation. In this plot different bands, which cross the E_f are coloured, while bands residing in deeper BE are shown by dashed coloured lines. (b) and (c) DOS of individual Bi-6p and Pd-4d orbitals respectively, obtained by integrating the DOS of these orbitals to all the Bi and Pd atoms in BiPd.

could be associated to the coordination geometry of Bi atom as shown in Fig.6.1(b). It is clear that one of the lobe of Bi-6p_y orbital is directed towards 4$d_{x^2-y^2}$ orbital of Pd atom (7) and the other side has proximity with 4d_{yx} orbital of Pd atoms (5 and 6). On the other hand, Pd atoms (1-4) form a geometry like a square planar coordination around the Bi atom which is tilted by 30° from the ZX plane. These arrangements and nearly equal inter-atomic distances of the Bi with these nn Pd atoms favor a strong intermixing between the different Bi-6p and Pd-4d orbitals and resulting bands span in the large energy range with varying contribution from the different orbitals.

To investigate the effects of SOC, band structure with inclusion of the SOC is calculated and illustrated in Fig.6.5(a). As clear from this plot that the various bands are splitted due to spin orbit interaction and the scale of splitting is varied at different k-points. Significant modification is observed in the bands which are placed in the vicinity of E_f. Several new electron and hole pockets with different sizes appear in comparison to the non SOC case (Fig.6.4(a)), like one hole pocket (orange band) between the Γ and X point, two electron pockets (green and brown band) between the Γ and Z point and electron pockets (maroon and yellow band) around the T point are the additional pockets. Moreover, the hole pocket shrinks remarkably around the Z point. These changes in the band structure signify that the SOC is quite pronounced and play an important role in constructing the FS topology in this system. There are many (18) spin-orbit split bands cross the E_f which give rise to a complex FS of BiPd as depicted in Fig.6.5(b). Shape of the FSs originating from different spin-orbit split bands is nearly identical. Mainly four types of distinct FS sheets can be identified which are shown in Fig.6.5(c), (d), (e), and (f) corresponding to the calculated band turquoise, indigo, blue and violet respectively. Two tiny electron pockets are visible at the center of zone faces in the FS made by turquoise band(6.5(c)) while two connected hole cones,

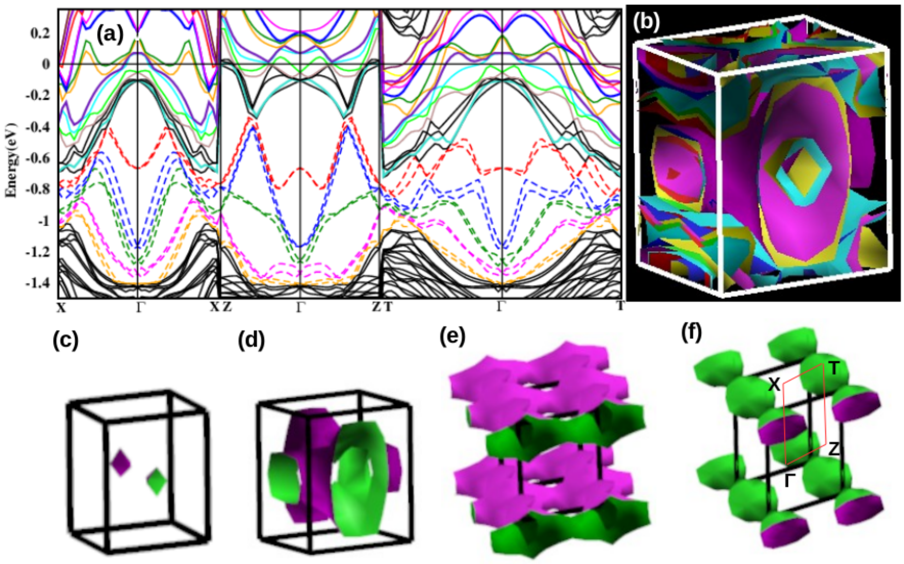

Figure 6.5: (a) Band structure plot of BiPd with including the SOC effects. Different bands crossing the E$_f$ are coloured while bands residing in deeper BE are shown by dashed coloured lines. (b) composite FS of BiPd. (c)-(f) Individual sheet of FS corresponding to calculated bands turquoise, indigo, blue and violet of the Fig. (a) respectively.

one along k$_z$ (larger in size) and second along k$_y$ (smaller in size), are observed in the second FS sheet(6.5(d)). On the other hand, hole like FS sheet originated from the Bi-6p$_y$ (blue) dominated band(6.5(e)) extends along the k$_y$ and k$_z$ directions in a cylindrical tubular form. Similarly, the fourth FS sheet (6.5 (f)) is composed of disconnected pieces of dumble shaped structure which are located at the edges of the BZ boundary. This type of FS, comprising of several sheets of multidimensional character, has also been witnessed in similar kind of SC BiPd$_2$ [33] as well as some other NCS SCs Ca(Pt/Ir)Si$_3$ [34], LaPdSi$_3$ [35] and Re$_{24}$(Nb;Ti)$_5$ [36].

Comparing these results to our ARPES findings, we find that the spectral weight distribution is higher around the Z(Fig.6.5(e)) and T(Fig.6.5(f)) points in comparison to the Γ point which is consistent with the experimental FS plots where high intensity distribution is found around the Z and T points compared to the Γ point(Fig.6.2(a) and (e)). Likewise, in band structure along the Γ-X direction(Fig.6.5(a)) the blue(dashed) bands meet the Γ point at E$_b$ = -1.17 eV and disperse strongly towards lower BE E$_b$ = -0.6 eV accompanied by the green bands. In the ARPES image Fig.6.2(b), intensity pattern shows the identical behaviour that is highly dispersive in the same BE range and crosses the Γ point $\sim$ E$_b$ = -1.15 eV. Further, the calculated red(dashed) band dispersion in the BE between E$_b$ = -0.7 eV to -0.48 eV is similar to the intensity variation observed in the same BE range in ARPES data. The calculated bands lying in deeper BE(dashed green, blue, magenta) along the Γ-T(Fig.6.5(a)) direction show resemblance with the corresponding ARPES results(Fig.6.2(f)), like the Γ-X direction. However, in this image Fig.6.2(f) the change in the calculated red(dashed) band along the Γ-T direction compared to the Γ-X direction is not properly identified. To consider the near E_f region, along the Γ-X direction the intensity pattern marked as an β band in (Fig.6.3(f)) appears to be the composite result of the calculated bands(violet, cyan), which form hole pockets around the Γ point, and green, brown(Fig.6.5(a)) bands. Similarly, the calculated dark green and orange electron like bands matches to the experimental δ band(Fig.6.3(f)) whereas the top of closely spaced cyan and black bands coincides with energy position of α band in ARPES data(Fig.6.3(f)) after renormalized by a factor of 2.5. This value of renormalization is consistent with the prediction of moderate electronic correlation in BiPd from the resistivity measurements estimating Kadowaki-Woods value [16]. Same scenario could also be seen along the Γ-T direction where composite structure of the calculated green, brown(Fig.6.5(a)) bands possibly leads to the β' band and renormalized cyan and black bands resulting the α' structure in ARPES image(Fig.6.3(h)) taken along the Γ-T direction. Though, the bands are not clearly discernible in the ARPES data but composite intensity behaviour show a qualitative agreement with some of the calculated bands, particularly in the higher BE region. These results are helpful for further detailed electronic structure study in order to have more quantitative matching between the DFT bands and ARPES results.

As it is clear from our band structure calculations and shown by our ARPES measurements (Fig.6.3(a)-(e)) various bands containing mainly Bi-6p with a little admixture of Pd-4d character are involved in the FS crossings. This highlights the possibility of multiband effects in this system, however, the strong 3D character of the different FS sheets weakens the possibility of nesting between them and consequently existence of any density wave instabilities, like charge density wave (CDW) and spin density wave (SDW) is also less probable in this compound [37]. The nature of Cooper pairing is expected to be more like spin-singlet assisted by phonons which has also been inferred previously from different experiments [17, 19]. Interestingly, there are few reports which explained their experimental observations in context of the coexisting spin-singlet and triplet pairing due to presence of ASOC in this compound [20–22]. Since, the ASOC split bands occur with different spin rotation because of interband SOC, the triplet pairing may be favored only at specific places in the resulting FS of such bands, like in other NC SC LaPtSi [38]. Hence its contribution could be quite less. Therefore, BiPd could be essentially a multiband s-wave SC.

6.4 Conclusion

In our ARPES study of BiPd, we found that various bands are involved in the crossings of E_f along both the Γ-X and Γ-T directions. The FS depicts a high intensity distribution at various parts of the surface BZ resulting from various electron and hole like bands which are present in the vicinity of the Fermi energy (E_f). These results are consistent with the high metallic nature of BiPd observed in resistivity measurements. One hole pocket around the Γ point and an electron pocket around the X point are also identified from the near E_f ARPES intensity plots. The ARPES results show a fairly good agreement with the calculated band structure, mainly in the higher BE region, though the bands are nor very discernible as predicted in the calculations. Our orbital resolved DOS calculation reveals that the near E_f states are primarily composed of Bi-6p orbitals with a little admixture of Pd-4$d_{x^2-y^2/zy}$ while the states at higher BE ($\sim E_b$ = -1.2 eV) are dominated by Pd-4d orbital character. This near E_f region is significantly modified with the inclusion of SOC effects and various new hole and electron pockets arising from the spin-orbit split bands appear in comparison to the non-relativistic case. FS manifested by these bands consists of multi sheets of different dimensions, mainly three dimensions which disfavor the nesting conditions and weakens the possibility for any density wave instabilities in this system. Since, spin split bands in ASOC driven systems have different spin rotation restricting the spin-triplet pairing at specific parts of the FS, like in NCS SC LaPtSi, the pairing should mainly be of singlet nature mediated via phonons.

Bibliography

[1] M. Z. Hasan and C. L. Kane, *Rev. Mod. Phys.*, **82**, (2010), 3045.

[2] Xiao-Liang Qi and Shou-Cheng Zhang, *Rev. Mod. Phys.*, **83**, (2011), 1057.

[3] L. P. Gorkov and E. I. Rashba, *Phys. Rev. Lett.*, **87**, (2001), 037004.

[4] P. A. Frigeri, D. F. Agterberg, A. Koga, and M. Sigrist, *Phys. Rev. Lett.*, **92**, (2004), 097001.

[5] R. Jha, B. Tiwari, P. Rani, H. Kishan and V. P. S. Awana, *J. Appl. Phys.*, **115**, (2014), 213903.

[6] Q. Zhang, G. Li, D. Rhodes, A. Kiswandhi, T. Besara, B. Zeng, J. Sun, Siegrist, M. D. Johannes and L. Balicas, *Scientific Reports*, **3**, (2013), 1446.

[7] Liang Fu and C. L. Kane, *Phy. Rev. Lett.*, **100**, (2008), 096407.

[8] David Hsieh, Y Xia, L Wray, Dong Qian, A Pal, JH Dil, J Osterwalder, F Meier, G Bihlmayer, CL Kane, YS Hor, RJ Cava, M Zahid Hasan, *Science*, **323**, (2009), 919.

[9] Su-Yang Xu, Ilya Belopolski, Nasser Alidoust, Madhab Neupane, Guang Bian, Chenglong Zhang, Raman Sankar, Guoqing Chang, Zhujun Yuan, Chi-Cheng Lee, Shin-Ming Huang, Hao Zheng, Jie Ma, Daniel S. Sanchez, BaoKai Wang, Arun Bansil, Fangcheng Chou, Pavel P. Shibayev, Hsin Lin, Shuang Jia, M. Zahid Hasan, *Science*, **349**, (2015), 613.

[10] T. Klimczuk, F. Ronning, V. Sidorov, R. J. Cava, and J. D. Thompson, *Phys. Rev. Lett.*, **99**, (2007), 257004.

[11] I. Bonalde, H. Kim, R. Prozorov, C. Rojas, P. Rogl, and E. Bauer, *Phys. Rev. B*, **84**, (2011), 134506.

[12] C. S. Lue, T. H. Su, H. F. Liu, and Ben-Li Young, *Phys. Rev. B* , **84**, (2011), 052509.

[13] Y. Huang, J. Yan, Y. Wang, L. Shan, Q. Luo, W. Wang and Hai-Hu Wen, *Supercond. Sci. Technol.*, **21**, (2008), 075011.

[14] R. Onuki, A. Sumiyama, Y. Oda, T. Yasuda, R. Settai and Y. Onuki, *J. Phys. Condens. Matter*, **21**, (2009), 075703.

[15] T. Akazawa, H. Hidaka, T. Fujiwara, T. C. Kobayashi, E. Yamamoto, Y. Haga, R. Settai, and Y. Onuki, *J. Phys. Condens. Matter*, **16**, (2004), L29.

[16] Rajveer Jha, Reena Goyal, P. Neha, V. Maurya, A. Srivastava, Anurag Gupta, S. Patnaik and V. P. S. Awana, *Sup. Sci. and Tech.*, **26**, (2016), 25008.

[17] Bhanu Joshi, A. Thamizhavel and S. Ramakrishnan, *Phys. Rev. B*, **84**, (2011), 064518.

[18] Y. C. Bhatt and K. Schubert, *J. of Less Comm. Metals*, **64**, (1979), 17.

[19] Zhixiang Sun, Mostafa Enayat, Ana Maldonado, Calum Lithgow, Ed Yelland, Darren C. Peets, Alexander Yaresko, Andreas P. Schnyder and Peter Wahl, *Nature Comm.* , **6**, (2015), 6633.

[20] Mintu Mondal, Bhanu Joshi, Sanjeev Kumar, Anand Kamlapure, Somesh Chandra Ganguli, Arumugam Thamizhavel, Sudhansu S Mandal, Srinivasan Ramakrishnan and Pratap Raychaudhuri, *Phys. Rev. B*, **86** , (2012), 094520.

[21] Kazuaki Matano, Satoki Maeda, Hiroki Sawaoka, Yuji Muro, Toshiro Takabatake, Bhanu Joshi, Srinivasan Ramakrishnan, Kenji Kawashima, Jun Akimitsu, Guo-qing Zheng, *J. Phys. Soc. Jpn.*, **82**, (2013), 084711.

[22] L. Jiao, J. L. Zhang, Y. Chen, Z. F. Weng,Y. M. Shao, J. Y. Feng, X. Lu, B. Joshi, A. Thamizhavel, S. Ramakrishnan, and H. Q. Yuan, *Phys. Rev. B* , **89**, (2014), 060507(R).

[23] Madhab Neupane, Nasser Alidoust, Su-Yang Xu, Ilya Belopolski, Daniel S. Sanchez, Tay-Rong Chang, Horng-Tay Jeng, Hsin Lin, Arun Bansil, Dariusz Kaczorowski, M. Zahid Hasan, and Tomasz Durakiewicz, *arXiv:1505.03466v1*.

[24] H. M. Benia, E. Rampi, C. Trainer, C. M. Yim, A. Maldonado, D. C. Peets, A. Sthr, U. Starke, K. Kern, A. Yaresko, G. Levy, A. Damascelli, C. R. Ast, A. P. Schnyder, and P. Wahl, *Phys. Rev. B* , **94**, (2016), 121407.

[25] S. Thirupathaiah, Soumi Ghosh, Rajveer Jha, E.D.L. Rienks, Kapildeb Dolui, V.V. Ravi Kishore, B. Bchner, Tanmoy Das, V.P.S. Awana, D.D. Sarma, and J. Fink, *Phys. Rev. Lett.*, **177**, (2016), 177001.

[26] Giannozzi P. et al. *http:/www.quantum-espresso.org*.

[27] Perdew J P,Burke K and Ernzerhof M, *Phys. Rev. Lett.*, **77**, (1996), 3865.

[28] Perdew J P and Wang Y, *Phys. Rev. B*, **45**, (1992), 13244.

[29] Perdew J P, Chevary J A, Vosko S H, Jackson K A, Pederson M R, Singh D J and Fiolhais C, *Phys. Rev. B*, **46**, (1992), 6671.

[30] Vanderbilt D Soft self-consistent pseudopotential in a generalized eigenvalue formalism, *Phys. Rev. B*, **41**, (1990), 7892.

[31] V. Brouet, W. L. Yang, X. J. Zhou, Z. Hussain, R. G. Moore, R. He, D. H. Lu, Z. X. Shen, J. Laverock, S. B. Dugdale, N. Ru and I. R. Fisher, *Phys. Rev. B* , **77**, (2008), 235104.

[32] J.J. Yeh and I.Lindau, *Atomic Data and Nuclear Data Tables*, **32**, (1985), 1-155.

[33] I. R. Shein and A. L. Ivanovskii, *J. Supercond. and Nov. Magn.* , **26**, (2013), 1.

[34] V. V. Bannikov, I. R. Shein and A. L. Ivanovskii, *ZhETF*, **92**, (2010), 381.

[35] M.J. Winiarski and M. Samsel-Czekala, *Intermetallics.*, **56**, (2015), 44.

[36] M.J. Winiarski, *J. Alloy and Comp.*, **616**, (2014), 1.

[37] A. M. Gabovich, A. I. Voitenko, J. F. Annett, M. Ausloos, *Sup. Sci. and Tech.*, **14**, (2001), R1.

[38] Kneidinger,F., Michor,H., Sidorenko,A., Bauer,E., Zeiringer,I., Rogl,P., Blaas-Schenner,C., Reith,D., Podloucky, R. , *Phys. Rev. B*, **88**, (2013), 104508.

Chapter 7

Valence Band Electronic Structure of Pd Based Ternary Chalcogenide Superconductors

This chapter comprises of the results of our electronic structure studies of Pd based ternary superconducting compounds; $Nb_2Pd_{0.95}S_5$, $Nb_2Pd_{1.2}Se_5$, $Ta_2Pd_{0.97}S_6$ and $Ta_2Pd_{0.97}Te_6$, which are recently discovered. We performed angle integrated photoemission measurements on these compounds and compared the results with our DOS calculations. This comprehensive study concludes that the valence band of these compounds are linked to their complex crystal structure.

7.1 Introduction

Recently discovered superconductors (SCs) like Fe-pnictides [1], Fe-chalcogenides [2], $SrRuO_4$ [3] and organic SC [4, 5], driven by unconventional pairing have given a new impetus to the research in the field of superconductivity. Discovery of Pd based ternary chalcogenides, like $Nb_2Pd_{0.95}S_5$ [6, 7], Nb_2PdSe_5 [8], Ta_2PdS_5 [9], $Ta_2Pd_{0.97}S_6$ [10], $Ta_2Pd_{0.97}Te_6$ [11] and $Ta_4Pd_3Te_{16}$ [12] is another advancement in this direction. These layered compounds provide a fertile ground for the existence of unconventional SC state owing to their Quasi-2-dimensional (Q2D) character [12, 13].

The interesting compounds in this low dimensional family, are $Nb_2Pd_{0.95}S_5$ and $Nb_2Pd_{1.2}Se_5$. They are isomorphic and have their superconducting critical temperature, T_c close to $\sim$ 6K [6, 8]. $Nb_2Pd_{0.95}S_5$ shows a Fermi liquid behavior at low temperatures. Sommerfiled coefficients estimated for $Nb_2Pd_{1.2}Se_5$ and $Nb_2Pd_{0.95}S_5$ i.e 15.7 and 32 mJ/mol-K^2 respectively, indicate moderately and strongly coupled electronic interactions respectively in them. Heat capacity measurements have shown signatures of multiband superconducting behavior in both the compounds which is well described by the two band-α model. Many unusual characters of these SCs have been analyzed from the point of view of spin-orbit scattering [8, 9, 14], multiband effects [15, 16] and unconventional pairing due to the presence of non centrosymmetric (NCS) structure [9,17,18] etc. On the other hand, ternary compounds such as $Ta_2Pd_{0.97}S_6$ and $Ta_2Pd_{0.97}Te_6$ belonging to the same monoclinic structure ($C_{2/m}$) like $Nb_2Pd_{0.95}S_5$, show different behavior. The telluride compound $Ta_2Pd_{0.97}Te_6$, which crystallizes in $Ta_4Pd_3Te_{16}$ phase, has a much lower residual resistivity than normal state resistivity in comparison to the $Nb_2Pd_{0.95}S_5$. These compounds share a common structure composed of chains of Pd and Nb/Ta centred polyhedra with S/Te atoms. Changes in the structural geometry is a key factor determining the different physical behavior of these ternary SCs.

Theoretical studies of the electronic structure of some of these materials, like Nb_2PdSe_5 [8], Nb_2PdS_5 [7], Ta_2PdS_5 [14], $Ta_4Pd_3Te_{16}$ [19] have been reported recently and established the multiband nature of these compounds. The Fermi surface (FS) of Nb_2PdS/Se_5, Ta_2PdS_5 compounds are composed of sheets of electron-hole character of different dimensions [7, 14, 19], which could favor the existence of various density wave instabilities, like charge density wave (CDW) and spin density wave (SDW) due to the nesting between the 1-D like sheets of FS in these systems [19]. So far, there have been no reports on the experimental studies of the electronic structure of these compounds. In this chapter we present a comprehensive photoemisson study on some of these ternary SCs $Nb_2Pd_{0.95}S_5$, $Nb_2Pd_{1.2}Se_5$, $Ta_2Pd_{0.97}S_6$ and $Ta_2Pd_{0.97}Te_6$ in conjugation with DFT based calculations. We observe that the VB spectra of $Nb_2Pd_{0.95}S_5$, $Nb_2Pd_{1.2}Se_5$ and $Ta_2Pd_{0.97}S_6$ are qualitatively similar except some slight differences in the energy position of various features. On the other hand, the VB spectra of $Ta_2Pd_{0.97}Te_6$ is remarkably different, particularly in the near E_f region where a clear metallic edge is observed, unlike the other compounds. Our study also shows the existence of a temperature dependent pseudogap in $Nb_2Pd_{0.95}S_5$ while the near E_f states remain unchanged with the lowering of temperature to 77 K in $Nb_2Pd_{1.2}Se_5$, $Ta_2Pd_{0.97}S_6$ and $Ta_2Pd_{0.97}Te_6$. In these compounds the different atomic packing could change the strength of inter-orbital hybridization among various atoms which leads to difference in their electronic structure as clearly seen in our DOS calculations. Our study highlights the role of structural geometry to the different VB spectra of these compounds.

7.2 Experimental and Calculation Details

Polycrystalline samples of $Nb_2Pd_{0.95}S_5$, $Nb_2Pd_{1.2}Se_5$, $Ta_2Pd_{0.97}S_6$ and $Ta_2Pd_{0.97}Te_6$ were synthesized via solid state reaction route. Stoichiometry was confirmed by XRD measurements. Structural and other physical properties were studied and reported earlier [6, 8, 10, 11]. Photoemission spectra were collected in angle integrated mode using a hemispherical SCIENTA-R3000 analyzer and a monochromatized He source (SCIENTA-VUV5040). The photon flux was of the order of 10^{16} photons/s/steradian with a beam spot of 2 mm in diameter. Fermi energy for all measurements were calibrated by using a freshly evaporated Ag film on to the sample holder. The total energy resolution, estimated from the width of the Fermi edge, was about 27 meV for the He I excitation. The measurements were performed at a base pressure better than $\sim 3.0 \times 10^{-10}$ mbar. Samples were scrapped in a preparation chamber with a diamond file at base pressure 5.0×10^{-10} mbar and the spectra were taken within an hour, so as to avoid any surface degradation. All the measurements were repeated 4-5 times and observed almost identical spectra at each measurement. For the temperature dependent measurements, the samples were cooled by pumping liquid nitrogen through the sample manipulator fitted with a cryostat. Sample temperatures were measured using a silicon diode sensor touching the bottom of the stainless steel sample plate. The low temperature photoemission measurements at 77 K were performed immediately after cleaning the sample surfaces followed by the room temperature measurements.

First-principles calculation were performed by using plain wave basis set inherent in Quantum Espresso (QE) [20]. Many electron exchange-correlation energy was approximated by Perdew-Burke-Ernzerhof (PBE) functional [21–23]. It was implemented in a scalar relativistic, ultrasoft pseudopotential [24]. Fine mesh of k-points with Gaussian smearing of the order 0.0001 Ry was used for sampling the Brillouin zone integration and kinetic energy and charge density cut-off were set to 180 Ry and 900 Ry respectively. Experimental lattice parameters and atomic coordinates of $Nb_2Pd_{0.95}S_5$ [6], $Nb_2Pd_{1.2}Se_5$ [8], Ta_2PdS_6 [25] and $Ta_4Pd_3S_{16}$ [26], after relaxed under damped (Beeman) dynamics with respect to both ionic coordinates and the lattice vector, were employed in the calculations. All parameters were optimized under several convergence tests.

7.3 Results and Discussion

Fig.7.1(a), (b) and (c) display the crystal structures of $Nb_2PdS(Se)_5$, Ta_2PdS_6 and $Ta_4Pd_3Te_{16}$ respectively. These layered compounds have a monoclinic structure, with space group symmetry $C_{2/m}$. The further details of crystal structures regarding lattice parameters, Wyckoff positions, site symmetry and fractional occupancies can be seen in Ref.[6], [8], [27] and [28] for $Nb_2Pd(S)_5$, Nb_2PdSe_5, Ta_2PdS_6 and $Ta_4Pd_3S_{16}$ respectively. These compounds exhibit complex structure consisting chains of Nb/Ta and Pd centered polyhedra of S/Te atoms. In Ta_2PdS_6, Pd centered octahedra bridges two Ta centered trigonal prismatic polyhedra [25]. Similarly, Pd atoms have edge sharing regular (Pd1) and edge sharing distorted (Pd2) octahedral coordination environment in $Ta_4Pd_3Te_{16}$ [26]. On the other hand, in $Nb_2PdS(Se)_5$, Pd atom has an octahedral coordination at Pd1 site and a distorted rhombohedral prismatic coordination at Pd2 site, which lies between the two adjacent layers [27]. The coordination environment of Pd (Nb/Ta) atoms and their bond lengths between the various near neighbor (nn) S(Se)/Te vary in the three crystal structures which leads to different strengths of inter-orbital hybridization. Consequences of these play important roles in the electronic structure of these compounds.

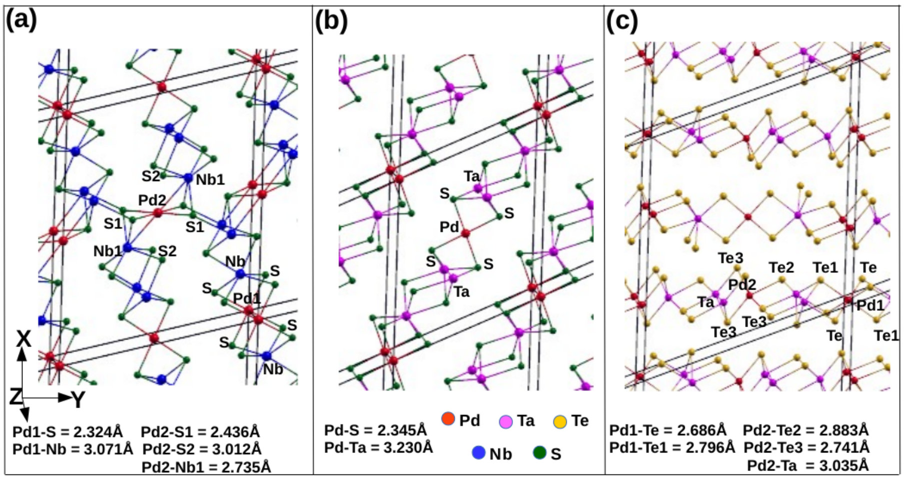

Figure 7.1: (a), (b) and (c) are crystal structure of $Nb_2PdS(Se)_5$, Ta_2PdS_6 and $Ta_4Pd_3Te_{16}$ respectively. Different nearest neighbours of Pd atom at inequivalent sites and bond lengths are marked in each structure.

Fig.7.2(a) shows valence band (VB) spectra of $Nb_2Pd_{1.2}Se_5$, $Nb_2Pd_{0.95}S_5$, $Ta_2Pd_{0.97}S_6$ and $Ta_2Pd_{0.97}Te_6$ obtained by using HeI and HeII excitation energies at 300 K respectively. In $Nb_2Pd_{1.2}Se_5$ spectra, seven features are observed at BE E_b = -0.27, -1.25, -1.99, -2.53, -3.27, -4.03 and -5.08 eV which are marked by A to G respectively. The features D, F and G are more intense compared to C and E while the near E_f feature A appears as a hump. The VB spectra of $Nb_2Pd_{0.95}S_5$ is similar to that of $Nb_2Pd_{1.2}Se_5$, except that all the features occur at slightly higher binding energy (BE) probably due to its higher resistivity. In $Ta_2Pd_{0.97}S_6$, the hump structure A occurs at E_b = -0.40 eV while feature C, D, F and G are observed at BE E_b = -2.39, -2.84, -4.56 and -5.40 eV respectively. The VB spectra of $Ta_2Pd_{0.97}Te_6$ is markedly different from those of the other two compounds. The hump structure A and features B, C are completely absent and a clear metallic edge is present at the Fermi Level (E_f). Furthermore, feature D, occurring at E_b = -2.49 eV BE, appears as an intense peak structure while features F and G are faint. By tuning the photon energy from HeI (21.2 eV) to HeII (40.8 eV), a significant increase is observed in the spectral weight of the feature D in all the compounds as can be seen in Fig.7.2 (b). While,

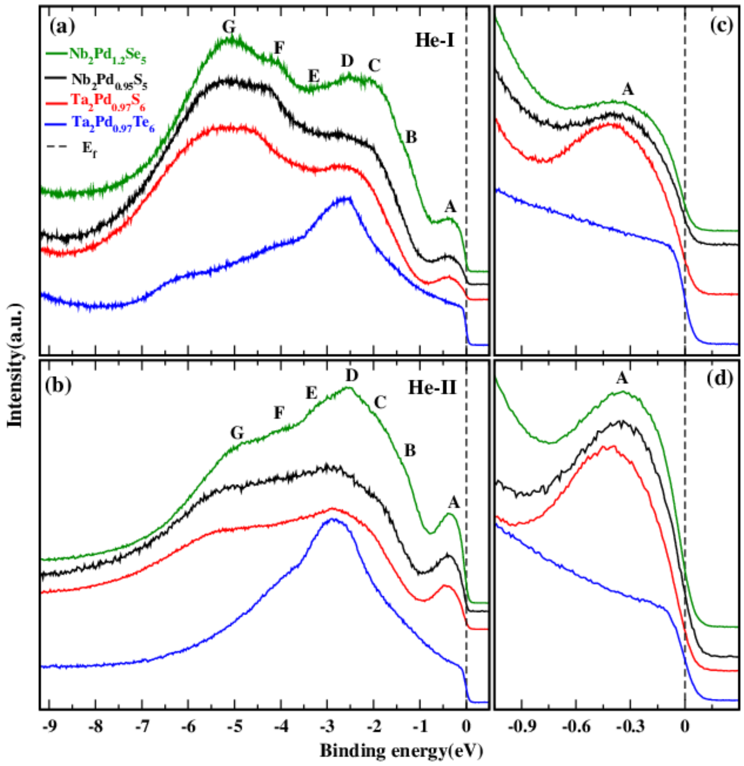

Figure 7.2: (a) and (b) valence band spectra of $Nb_2Pd_{1.2}Se_5$(Green) $Nb_2Pd_{0.95}S_5$(Black), $Ta_2Pd_{0.97}S_6$(Red) and $Ta_2Pd_{0.97}Te_6$(Blue) obtained by using HeI and HeII excitation energy respectively taken at 300 K. (c) and (d) are an enlarge view of near E_f region of the (a) and the (b) respectively.

the hump structure A becomes broader in $Nb_2Pd_{1.2}Se_5$, $Nb_2Pd_{0.95}S_5$ and $Ta_2Pd_{0.97}S_6$, the metallic edge at E_F in $Ta_2Pd_{0.97}Te_6$ appears smeared out slightly. These changes could be related to the different matrix elements involved in the photoemission process which depend on the ionization cross sections of atoms (σ). The σ multiplied by the number of valence electrons, for Pd_{4d} to $Se_{4p}(S_{3p})(\sigma_{Pd_{4d}}/\sigma_{Se_{4p}(S_{3p})})$ is $\sim$ 8(15) and 146(134) for HeI and HeII respectively [28]. The $\sigma_{Nb_{3d}}/\sigma_{S_{3p}}$, $\sigma_{Ta_{5d}}/\sigma_{S_{3p}}$ and $\sigma_{Ta_{5d}}/\sigma_{Te_{5p}}$ increase by a factor of ~ 2 for HeII with respect to HeI photon energy. These variations in the σ values for HeII indicate that the enhanced feature D and hump A are mainly composed of Pd_{4d} states. The relatively large intensification of feature D in $Ta_2Pd_{0.97}Te_6$ compared to the $Nb_2Pd_{0.95}S_5$ could be due to the additional increment in $\sigma_{Pd_{4d}}/\sigma_{Te_{5p}}$ value by 20% compared to $\sigma_{Pd_{4d}}/\sigma_{S_{3p}}$ for HeII. Similarly, composition of the metallic edge in $Ta_2Pd_{0.97}Te_6$ can be identified as mostly Te_{5p} states due to reduction in $\sigma_{Te_{5p}}$ for HeII. These changes are clearer in Fig.7.2(c) and (d) which displays an enlarged view of the near E_f region for HeI and HeII respectively. The DOS at E_f decreases in the order $Ta_2Pd_{0.97}Te_6$, $Nb_2Pd_{0.95}S_5$ and $Ta_2Pd_{0.97}S_6$ which agrees well with the trend in electrical resistivity shown by these compounds [6, 10, 11]. Interestingly, observation of the sharp metallic edge in $Ta_2Pd_{0.97}Te_6$, unlike $Nb_2Pd_{0.95}S_5$, could also be the reason for the drastic reduction (65%) in the ratio of normal state resistivity to the residual resistivity($\rho_{300K}/\rho(0)$) of $Ta_2Pd_{0.97}Te_6$ in comparison to $Nb_2Pd_{0.95}S_5$.

In order to understand the origin of the VB features, we have performed electronic band structure calculations for similar but stoichiometric compositions; Nb_2PdSe_5, Nb_2PdS_5 and Ta_2PdS_6. We use $Ta_4Pd_3Te_{16}$ crystal structure to identify the VB features of $Ta_2Pd_{0.97}Te_6$ because it crystallizes in $Ta_4Pd_3Te_{16}$ phase as observed in the XRD measurements [11]. Fig.7.3(a), (b), (c) and (d) show calculated DOS along with different atomic contributions of Nb_2PdSe_5, Nb_2PdS_5, Ta_2PdS_6 and $Ta_4Pd_3Te_{16}$ respectively. The strongly hybridized states of Pd_{4d} with their nn $Se(S)_p$ are dominant in the VB part, whereas conduction band (CB) region is mainly composed of hybridized states of Nb_{4d} and $Se(S)_p$ in Nb_2PdSe_5(Nb_2PdS_5). In Ta_2PdS_6 the CB is dominated by S_{3p}-Ta_{5d} hybridized states while the VB comprises mainly of S_{3p}-Pd_{4d} hybridized states. In this case, a dip can be seen in the DOS at the E_f contrary to the situation in Nb_2PdS_5 where sufficient states of S_{3p}-Nb_{4d} hybridization are observed in the near E_f region. This result is consistent with the experimentally observed metallic ($Nb_2Pd_{0.95}S_5$) and semiconducting ($Ta_2Pd_{0.97}S_6$) nature of these compounds [6, 10]. The gap like feature in Ta_2PdS_6 suggests that hybridization of Pd_{4d} and Ta_{5d} orbitals with their nn S_{3p} orbitals is stronger resulting in a clear separation between the bonding and antibonding states. Possibly this could be the reason for the occurrence of the features at higher BE in the experimental data of $Ta_2Pd_{0.97}S_6$ in comparison to the $Nb_2Pd_{0.95}S_5$. On the other hand, in $Ta_4Pd_3Te_{16}$ the presence of Te atoms modifies the electronic structure to a great extent. These atoms are more distant from Pd and Ta atoms which eventually reduces the strength of inter-orbital hybridization of Pd_{4d} and Ta_{5d} with their nn Te_{5p} orbitals. Therefore, Ta_{5d} and Pd_{4d} states are more localized than the same states in Nb_2PdS_5 and Ta_2PdS_6. Moreover, the large size of Te

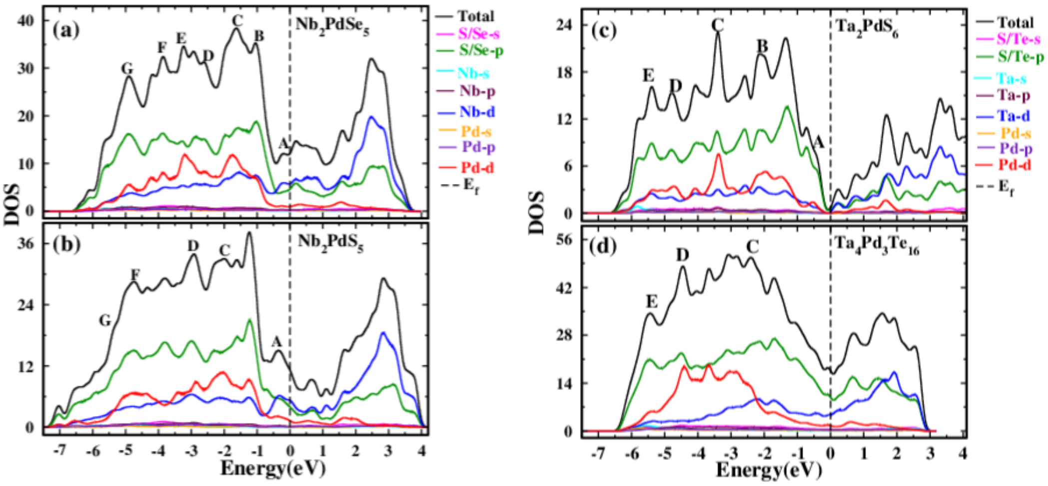

Figure 7.3: (a), (b), (c) and (d) show total calculated DOS with different atomic contributions of Nb_2PdSe_5, Nb_2PdS_5, Ta_2PdS_6 and $Ta_4Pd_3Te_{16}$ respectively.

atom distorts the chain of Pd and Ta centered polyhedra and results in several Te-Te bonds [19]. The hybridized states of these different Te-Te-5p orbitals diffuse within the VB and CB and the states crossing the E_f acquire mostly the Te_{5p} character. However, some small contribution from the Ta_{5d} states are also observed in the vicinity of E_f due to the weak Ta-Pd bond similar to the Nb-Pd bond at Pd2 site in Nb_2PdS_5(Fig.7.1(a)). The calculated DOS shows less intensity in the region between E_f and E_b = -2.0 eV in $Ta_4Pd_3Te_{16}$, unlike the other two compounds where many states (peak A and B) are observed in this region. This result qualitatively agrees with the absence of the hump A and feature B in the VB spectra of $Ta_2Pd_{0.97}Te_6$(Fig.7.2). Furthermore, various peaks are found in the calculated DOS which are not very clearly resolved in the VB spectra of all the compounds. However, the calculated peaks, which are closer to the experimentally observed VB features are labeled with same notation as used in the experimental VB spectra (Fig.7.2). These results indicate that the VB features (C, D and F) are mainly composed of S_{3p}-Pd_{4d} hybridized states in $Nb_2Pd_{0.95}S_5$, and $Ta_2Pd_{0.97}S_6$ while in the case of $Ta_2Pd_{0.97}Te_6$ Pd_{4d} states are dominant in the higher BE region (feature D, and F) and the near E_f states are dominated by Te_{5p} (Fig.7.2). The identification of Pd_{4d} character of the experimental feature D on the basis of the intensity enhancement of this feature in HeII spectra(Fig.7.2) is consistent with the calculated DOS. The variation in the calculated DOS of these compounds supported by our experimental findings highlights the role of the different structural geometry which leads to different strengths in the inter-orbital hybridization of Pd and Nb/Ta with their nn Se(S)/Te atoms and thereby the electronic structure.

It is clear from the above results of DOS that the Pd-4d, and Nb-4d states are strongly hybridized with Se/S states. The hybridization could be differ at two distinct coordination sites Pd1 and Pd2 due to different structural environment. In order to provide more insights into the effects of distinct coordination environment m-DOS of Pd is presented in Fig.7.4. Fig.7.4 (a) and (b) show Pd-4d states along with different d orbital contributions at Pd1 and Pd2 sites respectively in Nb_2PdSe_5. Fig.7.4 (c) and (d) show the same states in Nb_2PdS_5. The large band width of the Pd-4d seen in both the compounds indicates significant hybridization between the Pd-4d and the nn anion orbitals. In Nb_2PdSe_5, at the Pd1 site, the $4d_{x^2-y^2}$ and $4d_{xy}$ orbitals are directed towards the square planarly coordinated nn Se atoms and show largest separation between bonding (-4.81 eV and -4.28 eV) and antibonding (1.51 eV) states. The $4d_{3z^2-r^2}$ and $4d_{zx}$ orbitals are oriented towards the nn Pd and Nb atoms and show comparatively smaller separation between bonding (-3.81 eV) and antibonding (0.27 eV) states. This indicates a weak hybridization possibly due to the larger inter-atomic distances Pd1-Pd1 (3.406Å) and Pd1-Nb1 (3.102Å) in comparison to the Pd1-Se (2.392Å). On the other hand, at the Pd2 site, square planar coordination of the nn Se atoms are aligned in

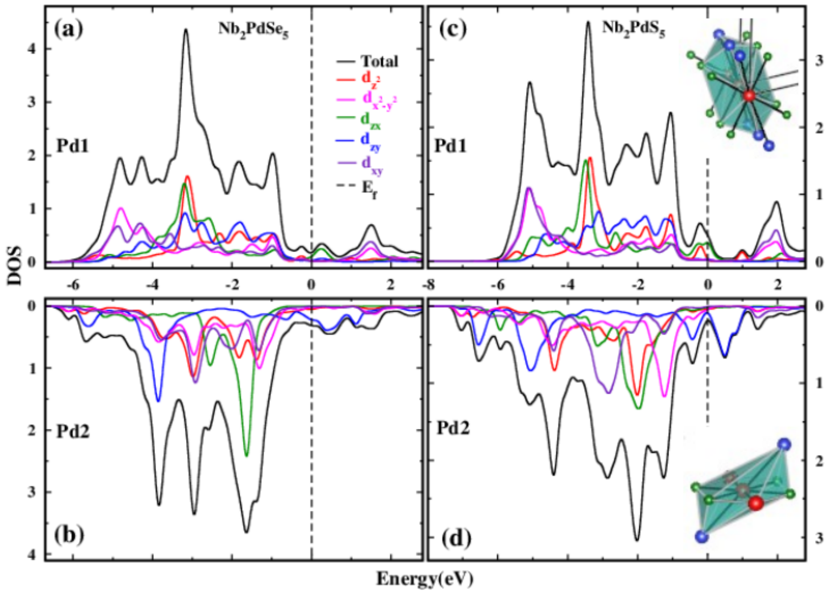

Figure 7.4: DOS originated from different orbitals of Pd-4d at sites Pd1 and Pd2 are shown in (a) and (b) respectively for Nb_2PdSe_5. (c) and (d) show the DOS at Pd1 and Pd2 site respectively for Nb_2PdS_5. Inset of each plot shows coordination environment of each Pd atom in respective compound where cartesian axis are set in same orientation as shown in crystal structure image(Fig.7.1). Red, blue and green colour balls represent Pd, Nb, and S(Se) atoms respectively.

the YZ plane (Fig.7.1). Therefore, the 4d_{yz} orbital is strongly hybridized with the nn Se and antibonding states of this orbital are predominant near the E_f. States originate from 4$d_{3z^2-r^2}$, 4d_{xy} and 4$d_{x^2-y^2}$ orbitals are moderately hybridized while the 4d_{zx} states show atomic like character. Apart from the differences in DOS of individual 4d orbitals originating from distinctly coordinated Pd atoms(Pd1, and Pd2), the largest peak of Pd1-4d DOS lies at higher BE relative to same peaks in Pd2-4d DOS. These differences could be related to different interorbital hybridization strengths due to the smaller distance of nn Se atoms at the Pd1 site (2.392 Å) as compared to the Pd2 site (2.598Å). In case of Nb_2PdS_5, the orbital character of different 4d orbitals of Pd at both the sites are similar to those of Nb_2PdSe_5. However, the DOS structure of various 4d orbitals for both Pd1 and Pd2 atoms are slightly different from Nb_2PdSe_5. This difference could be associated to change in the hybridization strength due to variation in the bond lengths between the two compounds. These results are compared with experimental findings which informs that the higher BE VB features G, and F(Fig.7.2) fall in bonding states of Pd1(4$d_{x^2-y^2}$ and 4d_{xy}) while the 4$d_{3z^2-r^2}$ (-1.65 eV) and 4$d_{x^2-y^2}$ (-1.35 eV) states of Pd2 are close to the experimentally observed features C and B respectively (Fig.7.2) in $Nb_2Pd_{1.2}Se_5$. Likewise, the energy position of differently coordinated Pd1 (4$d_{x^2-y^2}$ and 4d_{xy}) and Pd2 (4d_{zy}) states at BE -5.12 eV and -2.09 eV matches closely with the experimental features G and D respectively in the VB spectra of $Nb_2Pd_{0.95}S_5$ (Fig.7.2). The qualitative similarity of the experimental data with the calculated DOS establishes the presence of differently coordinated Pd atoms in both the compounds which has also been predicted theoretically in previous reports [7, 8, 14]. This behaviour of orbital specific changes in the DOS of the Pd$_{4d}$ with different coordination environment, is reminiscent of the electronic behavior of Fe-based superconductors like FeSe and FeTe [29].

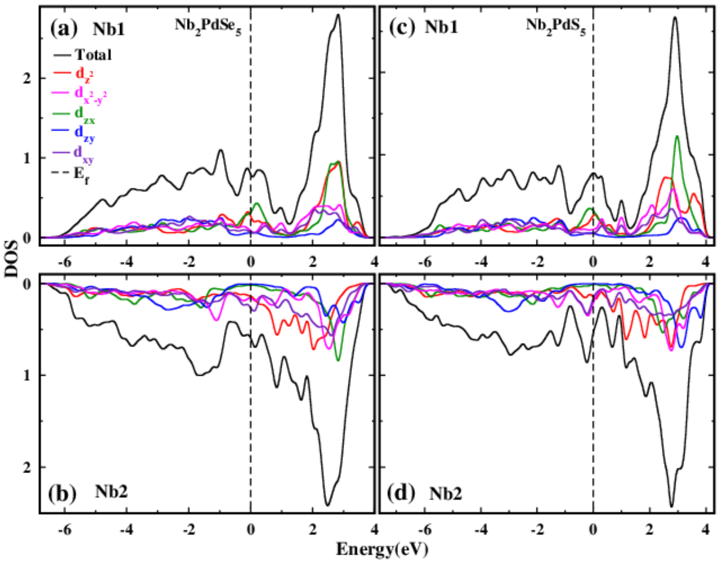

Figure 7.5: DOS originated from different orbitals of Nb-4d at site Nb1 and Nb2 are shown in (a) and (b) respectively for Nb$_2$PdSe$_5$. (c) and (d) show same DOS at Nb1 and Nb2 site respectively for Nb$_2$PdS$_5$.

In both the compounds Nb atoms also possess distinct coordination environment at two inequivalent sites Nb1 and Nb2, like the Pd atoms. We investigated the role of coordination geometry in the DOS of Nb atoms. Fig.7.5 depicts the Nb-4d DOS with different d orbital contributions at Nb1 and Nb2 sites for Nb$_2$PdSe$_5$(Fig.7.5(a) and (b)) and Nb$_2$PdS$_5$(Fig.7.5 (c) and (d)). In both cases, the DOS of Nb1 and Nb2 are not substantially different, unlike the case of Pd DOS. This could be due to the nearly same inter-atomic distances of the Nb atoms with their nn Se/S atoms at both the coordination sites (Nb1 and Nb2). However, a slight difference is visible between the DOS structure of Nb1 and Nb2 in the vicinity of the E$_f$ which is an important factor in the electronic structure of these compounds. Further, the orbital character of states which are predominantly involved in the E$_f$ crossing is 4d$_{3z^2-r^2}$, and 4d$_{zx}$ orbitals of Nb1 and 4d$_{xy}$ of Nb2. The presence of sufficient spectral weight of various Nb-4d orbitals at the E$_f$ and similar behavior of the E$_f$ crossing by orbital specific Pd-4d DOS(see Fig.7.4) are signatures of multiband nature of these compounds. These calculated results are also in good agreement with previous reports [7, 8, 14]. These signatures of the multiband effects are consistent with the multigap behavior observed in heat capacity measurements on these compounds [6, 8]. Furthermore, these compounds show a high anisotropy in upper critical field Hc$_2$ which is quite large in comparison to the Chandrasekhar-Clogston defined value of Pauli limiting field ($H_p{}^{BCS}$) along the most conducting direction in comparison to other crystallographic directions [6, 8]. Likewise, calculated value of the electron-phonon coupling in a similar kind of ternary SC Ta_2PdS_5 shows that the coupling is strong in this compound [14]. Such anomalous properties could be an indication for the existence of unconventional pairing in these ternary SCs which is possibly inherent to their layered (quasi 2D) structures.

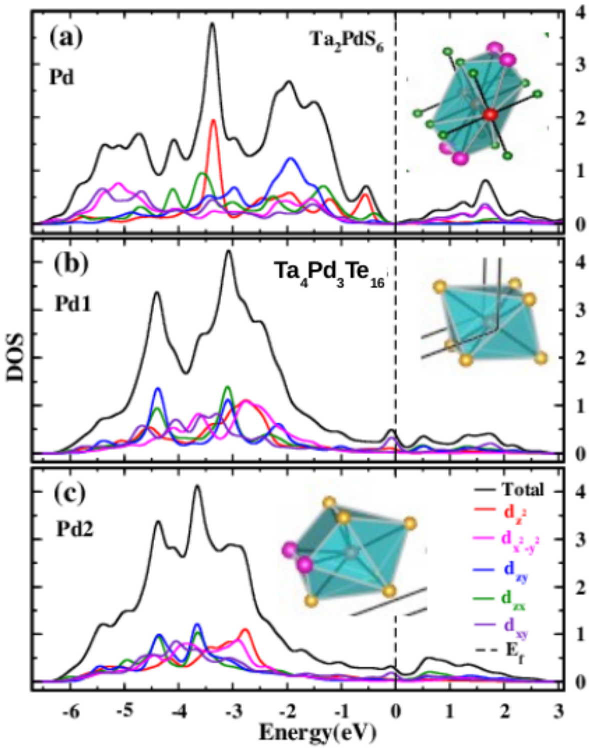

Figure 7.6: (a) Pd_{4d} DOS in Ta_2PdS_6. (b) and (c) Pd_{4d} DOS at site Pd1 and Pd2 in $Ta_4Pd_3Te_{16}$ respectively. Inset of each plot shows coordination environment of each Pd atom in respective compound where cartesian axis are set in same orientation as shown in crystal structure images(Fig.7.1). Red, green, magenta and yellow colour balls represent Pd, S, Ta and Te atoms respectively.

To address the role of Pd coordination in other ternary SCs, in Fig.7.6(a) DOS of Pd_{4d} in Ta_2PdS_6 is plotted and in Fig.7.6(b) and (c) DOS of Pd_{4d} at Pd1 and Pd2 sites in $Ta_4Pd_3Te_{16}$ are plotted respectively. In Ta_2PdS_6, square planar coordination of Pd aligns in a plane identical to the Pd1 in Nb_2PdS_5 with a different orientation. Hence, the nature of DOS originating from different orbitals of Pd_{4d} have similar character, like Pd1-4d DOS in Nb_2PdS_5. On the other hand, in $Ta_4Pd_3Te_{16}$, for both Pd atoms (Pd1 and Pd2), the $4d_{zy}$ and $4d_{zx}$ states are almost degenerate and the energy difference among different 4d states is negligible, unlike the Nb_2PdS_5. These calculations show that the antibonding states originated from Pd2 ($4d_{zy}$) and Pd1 ($4d_{x^2-y^2}$ and $4d_{xy}$) orbitals significantly contribute to the DOS at E_f in Nb_2PdS_5, unlike the scenario in Ta_2PdS_6 and $Ta_4Pd_3Te_{16}$ where the Pd_{4d} states are negligible at E_f. However, large number of Te-Te-5p hybridized states cross the E_f in $Ta_4Pd_3Te_{16}$(Fig.7.3). Hence, the considerable states derived Te_{5p} orbitals which are involved in crossing the E_f, is a signature for multiband effects in $Ta_4Pd_3Te_{16}$. This nature of multiband effects of different orbital character is consistent with previous report [19].

Fig.7.7(a) represents the near E_f VB spectra at 300 K (Black) and 77 K (Red) of $Nb_2Pd_{0.95}S_5$ and $Nb_2Pd_{1.2}Se_5$ while (b) and (c) correspond to the same spectra of $Ta_2Pd_{0.97}S_6$ and $Ta_2Pd_{0.97}Te_6$ respectively taken using the HeI source. Fig7.7(d), (e) and (f) depict the same spectra at 300 K and 77 K for the HeII excitation energy. Here, we have adopted the scheme of symmetrization [30] to the spectra with respect to the E_f in order to remove contribution arising from the Fermi-Dirac distribution function. In order to highlight the temperature dependent changes, difference between the normalized spectra collected at 300 K and 77 K is also plotted in each graph. In case of $Nb_2Pd_{0.95}S_5$, states in the vicinity of E_f are suppressed at 77 K in comparison to those at 300 K. This indicates the opening of a small(Δ = 95 meV) pseudogap which is more clear in the spectra taken with HeII. In this sample a crossover has been observed from electron to hole dominated transport carriers below 100 K in the Hall measurements [6]. This observation along with the presence of a pseudogap is again consistent with the pseudogap driven sign reversal in Hall coefficient predicted by Evtushinsky *et. al.* [31]. The coupling strength($2\Delta/k_BT$) estimated at this crossover temperature (100 K) from the gap value (Δ) is anomalously large ($\sim$ 20) which indicates little possibility for any density wave instabilities, like charge density wave (CDW) and

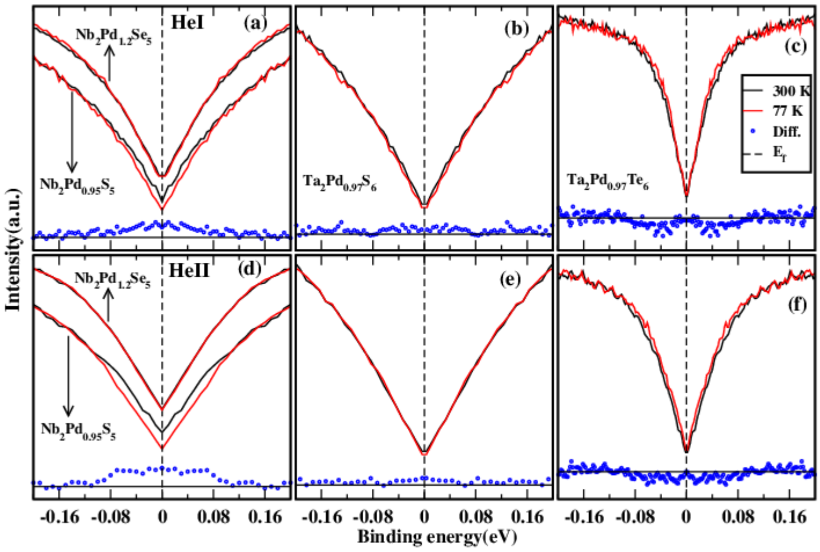

Figure 7.7: Near E_f VB spectra of $Nb_2Pd_{1.2}Se_5$ and $Nb_2Pd_{0.95}S_5$ (a), $Ta_2Pd_{0.97}S_6$ (b) and $Ta_2Pd_{0.97}Te_6$ (c) collected at 300 K(Black) and 77 K(Red) with HeI energy. Same spectra collected at HeII energy are shown in (d), (e) and (f) respectively. Blue dots represent difference between the normalized spectra taken at 300 K and 77 K. Here, we have adopted the scheme of symmetrization to the spectra with respect to E_F in order to remove contribution arising from Fermi-Dirac distribution function.

spin density wave (SDW) in this system to form the pseudogap. In addition, importance of electronic correlations have also not been found in earlier studies on this compound [6–8]. Whereas, in $Nb_2Pd_{1.2}Se_5$, the near E_f states remain unchanged with the lowering of temperature. In this compound the energy scale T $\sim$ 50 K, below which a crossover in the electronic ground state has been realized in the transport measurements [8] is lower than our measurement temperature 77 K. This could possibly be the reason for the unseen pseudogap feature at 77 K in this compound. Similarly, the near E_f states also remain unaffected with lowering of temperature to 77 K in other two compounds, $Ta_2Pd_{0.97}S_6$ and $Ta_2Pd_{0.97}Te_6$. Therefore, the origin of the observed pseudogap in $Nb_2Pd_{0.95}S_5$ could be associated to its complex structural geometry.

7.4 Conclusion

We have investigated the valence band electronic structure of Pd based ternary chalcogenide superconductors $Nb_2Pd_{0.95}S_5$, $Nb_2Pd_{1.2}Se_5$, $Ta_2Pd_{0.97}S_6$ and $Ta_2Pd_{0.97}Te_6$ using experimental valence band photoemission and theoretical band structure calculations. We observe that the VB spectra of $Nb_2Pd_{0.95}S_5$, $Nb_2Pd_{1.2}Se_5$ and $Ta_2Pd_{0.97}S_6$ are qualitatively similar except some slight differences in the energy position of various features. On the other hand, the VB spectra of $Ta_2Pd_{0.97}Te_6$ is remarkably different, particularly in the near E_f region where a clear metallic edge is observed, unlike the other compounds. Our study also shows the existence of a temperature dependent pseudogap in $Nb_2Pd_{0.95}S_5$ while the near E_f states remain unchanged with the lowering of temperature to 77 K in the other compounds. These changes seen the VB spectra could be due to their different structural geometry which provides different strengths to the inter-orbital hybridization of Pd and Nb/Ta with their nn S/Te atoms. This modifies the electronic structure significantly as clear from the plots of the calculated DOS of these compounds. Furthermore, in the calculated DOS, states crossing the E_f are dominated by different Pd-4d and Nb-4d orbitals ensuring the significant role for multiband effects in $Nb_2Pd_{1.2}Se_5$ and $Nb_2Pd_{0.95}S_5$ compounds. Our comprehensive study provides a deeper insight into the VB states of these Pd based ternary compounds in correlation with their different structural geometry.

Bibliography

[1] G. R. Stewart, *Rev. Mod. Phys.*, **83**, (2011), 1589.

[2] Y. Mizuguchi and Y. Takano, *J. Phys. Soc. Jpn.*, **79**, (2010), 102001.

[3] A. P. Mackenzie, Y. Maeno, *Rev. Mod. Phys.*, **75**, (2000), 657.

[4] M. R. Norman, *Science*, **332**, (2011), 196.

[5] K. Bechgaard, K. Carneiro, M. Olsen, F. B. Rasmussen, C. S. Jacobsen, *Phys. Rev. Lett.*, **46**, (1981), 852.

[6] R. Jha, B. Tiwari, P. Rani, H. Kishan and V. P. S. Awana, *J. Appl. Phys.*, **115**, (2014), 213903.

[7] Q. Zhang, G. Li, D. Rhodes, A. Kiswandhi, T. Besara, B. Zeng, J. Sun, Siegrist, M. D. Johannes and L. Balicas, *Scientific Reports*, **3**, (2013), 1446.

[8] Seunghyun Khim, Bumsung Lee, Ki-Young Choi1, Byung-Gu Jeon, Dong Hyun Jang, Deepak Patil, Seema Patil, Rokyeon Kim, Eun Sang Choi, Seongsu Lee, Jaejun Yu and Kee Hoon Kim, *New J. Phys.*, **15**, (2013), 123031.

[9] Y. F. Lu, T. Takayama, A. F. Bangura, Y. katsura, D. Hashizume and H. Takag, *J. Phys. Soc. Japan*, **83**, (2014), 023702.

[10] B. Tiwari, B. B. Prasad, R. Jha, D. K. Singh and V. P.S. Awana, *J. of Super. Nov. Magn.*, **27**, (2014), 2181.

[11] R. Goyal, B. Tiwari, R. Jha, and V. P.S. Awana, *J. of Super. Novel. Magn.*, **28**, (2015), 119.

[12] Wen-Hu Jiao, Zhang-T Tang, Yun-Lei Sun, Y. Liu, Q. Tao, Chun-Mu Feng, Yue-Wu Zeng, Zhu-An Xu and Guang-Han Cao, *J. of Am. Chem. Soc.*, **136**, (2014), 1284.

[13] J. Pan, W. H. Jiao, X. C. Hong, Z. Zhnag, L. P. He, P. L. Cai, G. H. Cao and S. Y. Li, *Phys. Rev. B*, **13**, (1976), 3284.

[14] David J. Singh, *Phys. Rev. B*, **88**, (2013), 174508.

[15] Masahiro Takahashi, Takeshi Mizushima and Kazushige Machida, *Phys. Rev. B*, **89**, (2014), 064505.

[16] D.A. Zocco, K. Grube, F. Eilers, T. Wolf and H.v. Lohneysen, *Phys. Rev. Lett.*, **111**, (2013), 057007.

[17] Suk Joo Youn, Mark H. Fischer, S. H. Rhim, Manfred Sigrist, and Daniel F. Agterberg, *Phys. Rev. B*, **85**, (2012), 220505(R)

[18] Jun Goryo, Mark H. Fischer and Manfred Sigrist, *Phys. Rev. B*, **86**, (2012), 100507(R)

[19] David J. Singh, *Phys. Rev. B*, **90**, (2014), 144501.

[20] Giannozzi P. *et. al.*, *http:/www.quantum-espresso.org*.

[21] Perdew J P,Burke K and Ernzerhof M, *Phys. Rev. Lett.*, **77**, (1996), 3865.

[22] Perdew J P and Wang Y, *Phys. Rev. B*, **45**, (1992), 13244.

[23] Perdew J P, Chevary J A, Vosko S H, Jackson K A, Pederson M R, Singh D J and Fiolhais C, *Phys. Rev. B*, **46**, (1992), 6671.

[24] Vanderbilt D Soft self-consistent pseudopotential in a generalized eigenvalue formalism, *Phys. Rev. B*, **41**, (1990), 7892.

[25] D. A. Keszler, P. J. Squattrito, N. E. Brese, J. A. Ibers, S. Maoyu and L. Jiaxi, *Inorg. Chem.*, **24**, (1985), 3063.

[26] A. Mar and J. A. Ibers, *J. Chem. Soc. Dalton Trans.*, **1**, (1991), 639.

[27] D. A. Keszler, J. A. Ibers, S. Maoyu and L. Jiaxi, *J. of Solid State Chem.*, **57**, (1985), 68.

[28] J.J. Yeh and I.Lindau, *Atomic Data and Nuclear Data Tables*, **32**, (1985), 1-155.

[29] H. Lohani, P. Mishra and B. R. Sekhar, *Physica C*, **512**, (2015), 54.

[30] S. V. Borisenko, A. A. Kordyuk, A. N. Yaresko, V. B. Zabolotnyy, D. S. Inososv, R. Schuster, B. Buchner, R. Weber, R. Follath, L. Patthey and H. Berger, *Phys. Rev. Lett.*, **100**, (2008), 196402.

[31] D. V. Evtushinsky, A. A. Kordyuk, V. B. Zabolotnyy, D. S. Inosov, B. Buchner, H. Berger, L. Patthey, R. Follath and V. Borisenko, *Phys. Rev. Lett.*, **100**, (2008), 236402.

Chapter 8

Investigation of correlation effects in FeSe and FeTe by LDA+U method

The chalcogenide family of FeSCs has attracted much attention due to its strongly correlated nature, unlike other SCs. We investigated the effect of correlation in FeSe and FeTe in detail. A comparative report of the results is presented in this chapter which discloses an orbital selective nature of the correlation effects in both the compounds.

8.1 Introduction

Iron based superconductors, particularly members of $FeSe_{1-x}Te_x$ family attract much attention due to their nature of strong electron correlation unlike other superconductors. A recent advancement in this field is the synthesis of single-layer films of FeSe on $SrTiO_3$ substrates exhibiting superconductivity (T_c = 80 K) which turns insulating with the addition of one more layer [1]. This unusual behavioral difference between single and double layer films of FeSe is a signature of strong electron correlation which has been experimentally observed [2, 3]. Superconductivity in the $FeSe_{1-x}Te_x$ compounds was first reported by Hsu *et al.* [4] in the FeSe (x = 0) compound exhibiting a T_c around 8 K which rises up to 37 K under pressure (7 GPa) [5]. On the other hand, the other extreme composition of this family, $Fe_{1.068}Te$, though not a superconductor show a spin density wave (SDW) ordering at 67 K [6] with an accompanying structural transition from tetragonal to monoclinic. With Se doping superconductivity emerges in FeTe with a simultaneous decrease in the SDW and the value of T_c reaches maximum 15 K for x = 0.5 doped case [7,8]. The Fe content is also detrimental for superconductivity; with excess Fe favors the spin localization destroying the superconductivity [9, 10]. Both FeSe and FeTe have tetragonal crystal structure belonging to space group symmetry P_4/nmm. It consists of a square planar sheet of Fe atoms, which is tetrahedrally coordinated with anion (Se/Te) atoms. However, the height of anion atom from the

Fe square plane is different in these two compounds and this plays a pivotal role in determining the electronic properties of these systems [11–13].

A recent ARPES study on FeSe$_{1-x}$Te$_x$ compositions by Ieki *et al.* [14] has shown clearly the strong electronic correlation in these compounds, where a small quasi particle weight in FeTe transforms into a sharp one with increase in Se content. Other ARPES results [15, 16] on these compounds have shown significant band renormalization which was supported by the calculations based on local density approximation (LDA). Tamai *et al.* [17] has found the mass renormalization factor (*m*/m*) to be =20 from their ARPES study on FeSe$_{0.42}$Te$_{0.58}$. It is close to the value observed in highly correlated systems like transition metal oxides. Also, our angle integrated valence band photoemission study on FeSe$_{1-x}$Te$_x$ [18] revealed significant spectral weight shifts in the near E$_f$ region with Se doping leading to the formation of a pseudogap. Further, a temperature dependent orbital selective spectral weight transfer was also reported by us [18]. Although, such manifestations of the strong coulomb correlation were also shown in many other photoemission studies [19, 20], these experimental observations are not well addressed by LDA based electronic structure calculations. Nevertheless, results of some recent calculations [21–23], where Coulomb correlations were included by using LDA + DMFT frame work, are very close to the experimental findings. In this paper we are presenting our calculations showing the variations in the electronic structure of FeSe and FeTe as a function of the strength of the Coulomb interaction *U* and intra-atomic exchange *J* based on LDA + *U* scheme. We observed multi orbital correlation effect in Fe-3d states which is more prominent in FeSe in comparison to FeTe. We have discussed our results referring to the difference in the geometry of the anion tetrahedra in both the compounds. The correlation effects which dependent on the anion height lead to many interesting electronic properties in the Fe(Se,Te) systems. Changes in the occupancy of electrons in the d$_{yz/xz}$ and d$_{x^2-y^2}$ orbitals of Fe-3d with *U* and *J*, are opposite in case of FeTe and FeSe. Our results further point out that, the electron pocket at the M point of the Brillouin zone and nature of the pseudogap at E$_f$ are also linked to the anion height dependent correlation effects in the family of Fe superconductors.

8.2 Details of Calculation

The band structure calculations we performed were based on first principles Langreth-Meh-Hu gradient corrected von Barth Hedin parametrized LDA [24] energy and potential using TB-LMTO-ASA code [25–27]. Lattice parameters used in the calculations are taken from the experimental data [28, 29] published earlier by others. Correlation effects in the Fe-3d orbitals have been examined by employing different values of Coulomb interaction parameter U and Hund's coupling J [30]. Empty spheres were introduced to make the volume of the unit cell equal to the total volume of the spheres within the permissible limit of atomic sphere approximation (ASA). Fe-4s, 4p, 3d; Se-4s, 4p, 4d and Te-5s, 5p, 5d orbitals are used as the basis set for the valence energy region. A mesh of $12 \times 12 \times 8$ is used for sampling the irreducible part of the Brillouin zone integration. Height of the anion atom from the Fe square plane was relaxed by minimizing the total self consistent energy using Quantum Espresso code [31]. We checked our calculation parameters by comparing them with the LDA results reported earlier [32, 33].

8.3 Results and Discussion

Fig. 8.1(a) and (b) shows the plots of density of states (DOS) for FeSe and FeTe respectively for the energy range of 4.0 to - 7.0 eV. The valence band (VB) DOS comprises of the region from E_f to - 6.0 eV binding energy (BE) while the unoccupied DOS extends from E_f to 3.0 eV. The near E_f states from 2.8 to - 2.4 eV are predominantly Fe-3d derived for both FeSe and FeTe. These Fe-3d states, separated in lower and upper bands exhibit a clear pseudogap feature just above the E_f (0.24 eV) in the case of FeSe. The pseudogap is less prominent in the case of FeTe. The states around - 2.2 to - 6.0 eV originate from the Fe-3d and anion (Se/Te)-p hybridized states. Interestingly, for the case of FeSe, there exists a sharp gap at - 2.3 eV which is not present in case of FeTe. Due to the smaller electronegativity of Te compared to Se, the hybridized states between Fe-3d and anion-p orbitals are placed at a lower BE in FeTe in comparison to those of FeSe. DOS have also been calculated after downfolding the valence orbital of the anion atom (Fig. 8.1(c) and (d)) in order to get a deeper insight into the role of anion orbitals. The gap at - 2.3 eV present in Fig. 8.1(a) is due to the splitting of bonding and antibonding bands between Fe-3d and Se-p hybridized states which becomes less prominent when the valence orbitals of Se atom are downfolded as shown in Fig. 8.1(d). Similarly the pseudogap feature across the E_f is also associated with the hybridization between Fe-3d and Se-p orbitals. Unlike FeSe, the anion orbitals do not play any major role in modifying the DOS in FeTe as is clear from Fig. 8.1(b) and (d). It indicates a weak hybridization between Fe-3d and Te-p orbitals in FeTe. The role of the anion orbitals is linked to the structural geometry of FeSe and FeTe. The insets of Fig. 8.1(c) and (d) show the geometry of anion tetrahedra in FeSe and FeTe respectively. This tetrahedral geometry depends on two important parameters; firstly, the height of anion from the Fe square plane (z) which is 1.64 Å and 1.46 Å in case of FeTe and FeSe respectively and secondly, the anion-Fe-anion angle (α). The enhanced z height in case of FeTe reduces the interorbital hoping among the Fe-3d orbitals, mediated via anion p orbitals. Similarly, the value of α is 99.9° in case

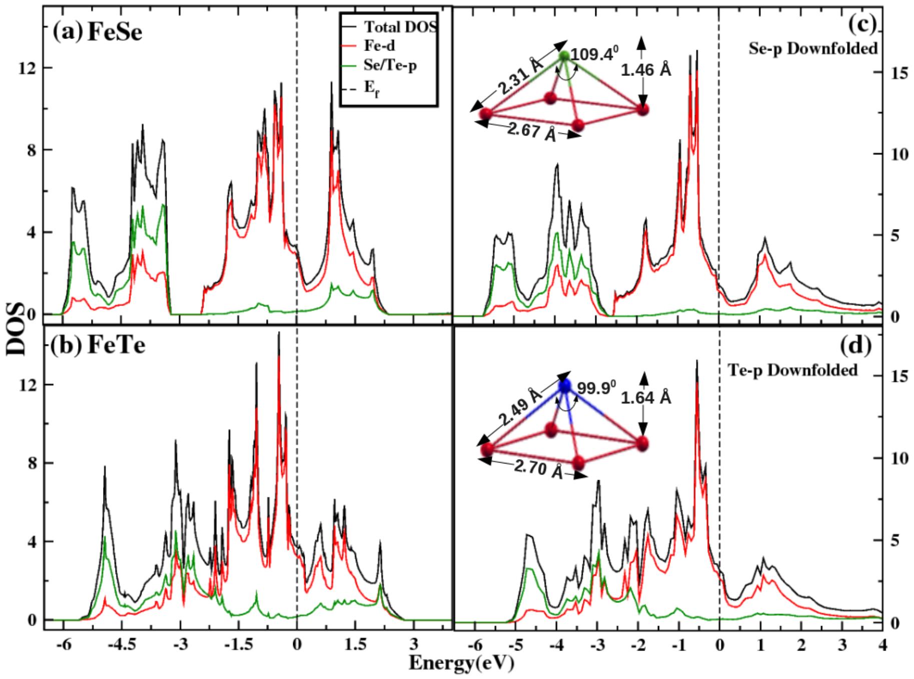

Figure 8.1: Total and partial DOS plotted for FeSe in (a) and for FeTe in (b). In (c) and (d) total and partial DOS calculated with Se-p and Te-p valence orbitals downfolded in FeSe and FeTe respectively. Inset of (c) and (d) shows the anion tetrahedra in FeSe and FeTe. Fe, Se and Te atoms are denoted by red, green and blue colours respectively.

of FeTe which increases to the perfect tetrahedron value 109.4° in case of FeSe. The large value of α and small value of anion height (z) makes a stronger hybridization between the Fe-3d and anion-p orbitals in case of FeSe in comparison to FeTe. This difference in hybridization strength is reflected in Fig. 8.1(a) and (c).

Coulomb correlation effects are important in bands of narrow width, especially in Fe-3d states. So the changes in Fe-3d states under the influence of different values of U have been calculated and shown for FeSe and FeTe in Panel (a) and (b) respectively of Fig. 8.2. In FeSe, Fe-3d states start localizing with the application of U and noticeable changes occur at higher values of U. For $U = 4.0$ eV case, the pseudogap feature disappears around E$_f$ and only two peaks are observed in the VB compared to the case of $U = 0.0$ eV. These two peaks merge and shift towards higher BE at $U = 5.0$ eV. In case of FeTe, the Fe-3d states also become localized under the application of U. However the amount of shift towards higher BE at large values of U (3.5 and 5.0 eV) is less and states are more at the vicinity of E$_f$ at smaller values of U (1.0 and 2.0 eV). In addition to this, narrowing of the lower and upper bands of Fe-3d states with increase of U is less. It indicates that the effect of Coulomb correlation is weak in FeTe. Possible reason for this, is the presence of Te-p states at lower BE which screen the U strongly [34]. On the basis of previous reports [21, 23, 34] the value of $U = 4.0$ and 3.5 eV are chosen to see the evolution of Fe-3d states under the influence

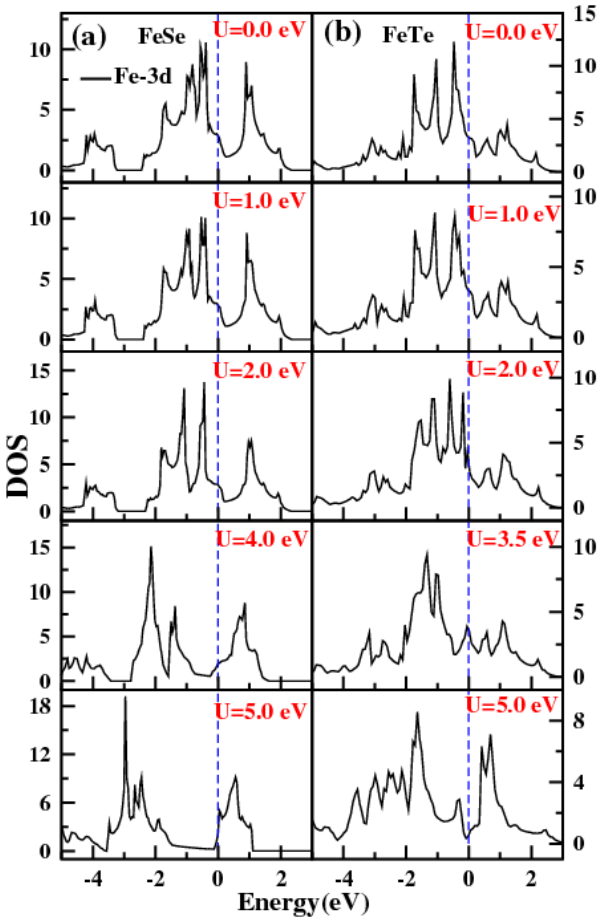

Figure 8.2: Changes in the Fe-3d states for different values of *U* are shown for FeSe (a) and FeTe (b). Values of *U* is shown in red colour in each plot.

of *J* in FeSe and FeTe as shown in Fig. 8.3(a) and (b) respectively. These results show that Hund's coupling *J* is a key factor in the formation of Fe-3d DOS. It is observed that the Fe-3d states are modified significantly even by introduction of a small value of J = 0.1 eV in case of FeSe. The Hund's coupling, shifts all the Fe-3d states towards lower BE, with a simultaneous appearance of pseudogap slightly above E_f. With increase in the value of *J* further, there is no substantial changes in the DOS. In the case of FeTe, the Fe-3d states are also shifted towards lower BE, particularly the states near E_f increase gradually, with the incorporation of *J* though the changes are less as compared to FeSe.

In order to highlight the correlation effects, DOS of different Fe-3d orbitals are plotted at different values of *U* and *J* in FeSe and FeTe as shown in Panel (a) and (b) respectively of Fig. 8.4. In FeSe, in the absence of *U* and *J*, near E_f states and the pseudogap feature arise from the $d_{yz/xz}$ and $d_{x^2-y^2}$ orbitals. The states originating from the d_{xy} orbital have largest splitting with two peaks at - 1.7 and 1.6 eV in the DOS. Additionally, a clear gap is observed in the $d_{3z^2-r^2}$ states around E_f which are quite localized at -0.8 eV. Application of Coulomb interaction (U = 4.0 eV), results in

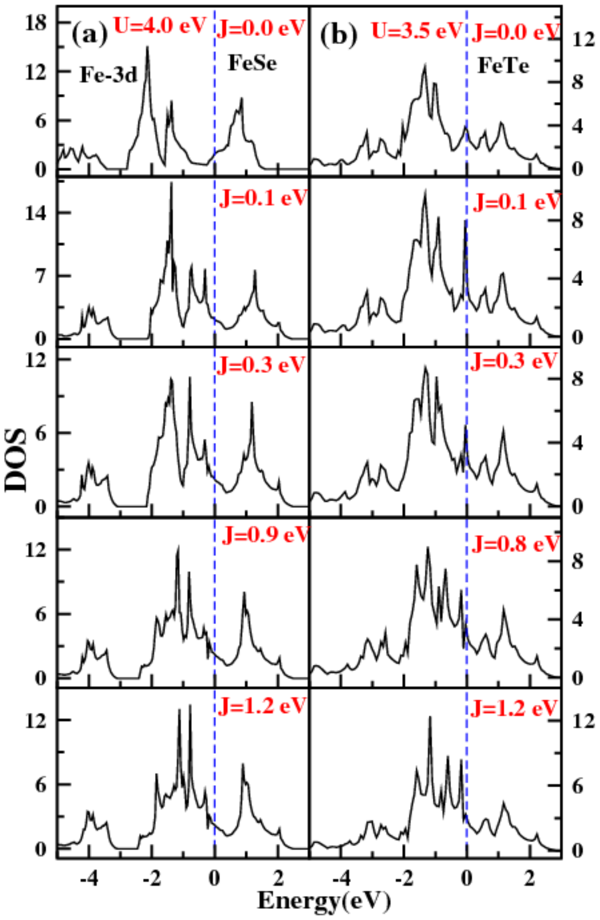

Figure 8.3: Changes in the Fe-3d states for different values of *J* are shown for FeSe (a) and FeTe (b). Values of *J* is shown in red colour in each plot. *U* is fixed at 4.0 and 3.5 eV for FeSe and FeTe respectively.

localization of the states derived from all four orbitals and the states shift towards higher BE. This shift is largest in the states of $d_{x^2-y^2}$ orbital. Major effect of *U* is observed in the $d_{yz/xz}$ states, where broad states near E_f transforms into two clear peaks at higher BE. Hence the pseudogap feature vanishes across E_f. Application of a small value of Hund's coupling $J = 0.1$ eV, restore the $d_{yz/xz}$ states near E_f and no significant changes are seen by further increasing the *J* value from 0.1 to 1.2 eV. This nature of pseudogap, which occurs in full range of Hund's coupling but absent when $J = 0.0$ at $U = 4.0$ eV, is consistent with the previous work of Ansgar *et al.* [22] where the pseudogap is attributed to a resonance in self energy caused by spin fluctuations. In case of FeTe, in the absence of *U* and *J* values, near E_f states and pseudogap are also formed by the $d_{yz/xz}$ and $d_{x^2-y^2}$ states like in FeSe. Moreover in FeTe, a gap is present at - 0.7 eV in the $d_{yz/xz}$ states and the number of these states are high across the E_f. The $d_{3z^2-r^2}$ and $d_{x^2-y^2}$ states shift towards higher BE by switching on the $U = 3.5$ eV and the amount of shift is quite small in comparison to FeSe. These states show an incremental shift towards E_f with an increase in the *J* value. These changes in DOS are presented in Table 8.1, where the occupancy of electrons in different orbitals

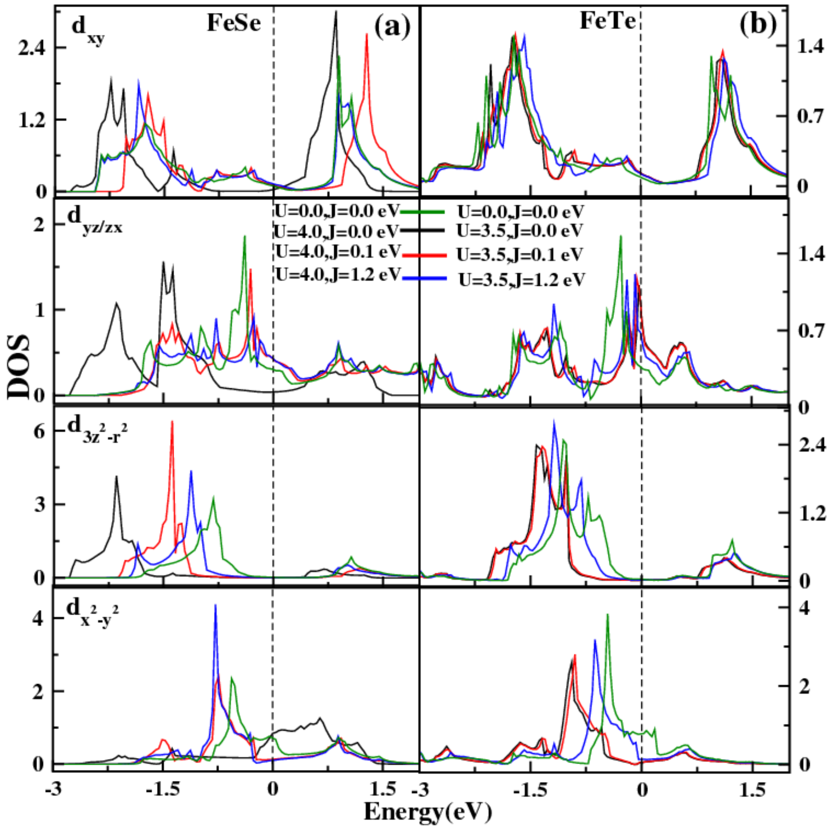

Figure 8.4: Changes in the DOS of different d orbitals of Fe atom at different values of *U* and *J* are plotted for FeSe (a) and FeTe (b). Values of *U* and *J* are marked by green, black, red and blue colours in the Figure.

of Fe-3d are tabulated. The occupancy of d$_{yz/xz}$ and d$_{x^2-y^2}$ orbitals show opposite behaviors for FeSe and FeTe under the influence of Coulomb correlation energy. On the other hand, in FeSe a remarkable enhancement is observed in the occupancy of the d$_{x^2-y^2}$ orbital after introducing *J* = 0.1 eV. It is almost twice in comparison to the *J* = 0.0 eV case. The change in the occupancy of Fe-3d orbitals due to the *U* and *J* presented here summaries the orbital selective effect in Fe-3d orbitals in FeSe and FeTe. The individual occupancy of four orbitals are different which are further enhanced by the Coulomb interaction and Hund's coupling. This orbital selective nature of the correlation effect depends crucially the on individual band filling factor [35, 36].

Fig. 8.5 shows the near E$_f$ band structure of FeSe with *U* = 0.0 (a), *U* = 4.0 eV (b) and FeTe with *U* = 0.0 (c) and *U* = 3.5 eV (d). Initially when *U* and *J* = 0.0 eV, three hole like and two electron like bands are observed at the Γ and M points respectively in both FeSe and FeTe. However, the outer hole like bands are quasidegenerate in case of FeSe. In order to show the contribution of different Fe-3d orbitals, fatness of the bands are calculated for both FeSe and FeTe. These bands are plotted in Fig. 8.5 (e-h) for the FeSe case with the *U* and *J* = 0.0 eV. Fatness indicate that the innermost hole like band has a d$_{yz/xz}$ and the outer two have d$_{xy}$ and d$_{x^2-y^2}$ orbital characters in

Table 8.1: Changes in the occupancy of electrons in different d orbitals of Iron under the application of different values of *U* and *J* in FeSe and FeTe.

			FeSe		
U(eV)	*J*(eV)	d_{xy}	$d_{xz/yz}$	$d_{3z^2-r^2}$	$d_{x^2-y^2}$
0.0	0.0	1.239	1.300	1.461	1.363
4.0	0.0	0.954	1.581	1.655	0.792
4.0	0.1	1.073	1.257	1.765	1.436
4.0	1.2	1.189	1.203	1.593	1.526
			FeTe		
0.0	0.0	1.242	1.308	1.462	1.363
3.5	0.0	1.182	1.109	1.569	1.637
3.5	0.1	1.174	1.138	1.558	1.634
3.5	1.2	1.189	1.209	1.514	1.572

both the compounds. Similarly the electron like bands are composed mainly of $d_{x^2-y^2}$ with a little contribution from the $d_{yz/xz}$ orbital in FeSe. In case of FeTe, the inner electron like band (- 0.23 eV) has $d_{yz/xz}$ and the outer one (- 0.47 eV) has $d_{x^2-y^2}$ orbital character in FeTe. Another major

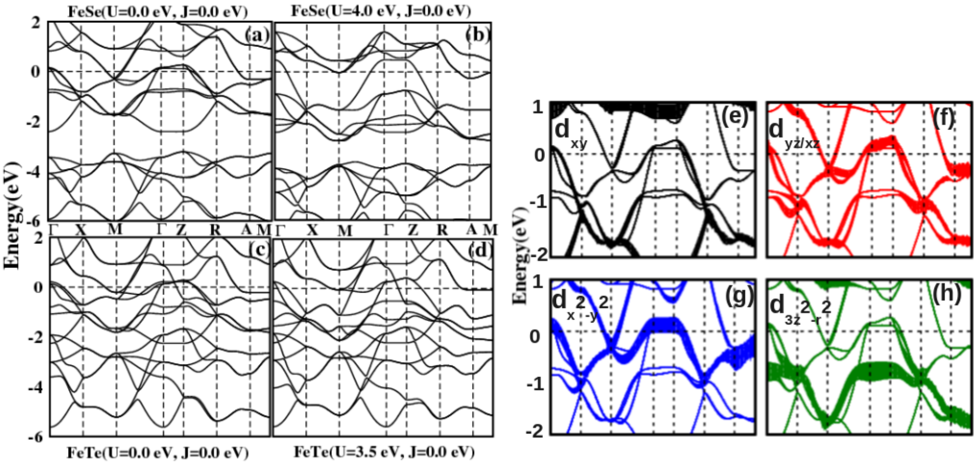

Figure 8.5: (a) and (b) show band structure plot of FeSe at *U* = 0.0 and *U* = 4.0 eV respectively. (c) and (d) show band structure plot of FeTe at *U* = 0.0 and *U* = 3.5 eV respectively. (e), (f), (g) and (h) show fatness of bands which originate from d_{xy}, $d_{yz/xz}$, $d_{x^2-y^2}$ and $d_{3z^2-r^2}$ orbitals respectively for FeSe at *U* and *J* = 0.0 eV.

difference between FeTe and FeSe is that the Te-p bands are intermixed with Fe-d bands unlike the FeSe, where Fe-d bands are well separated from the Se-p bands. These Te-p bands screen the effect of the Coulomb interaction *U* in FeTe, hence the value of *U* is smaller in FeTe in comparison to FeSe. After applying Coulomb interaction the degeneracy of the d_{xy} and $d_{x^2-y^2}$ hole like bands at the Γ point has been lifted as shown in Fig. 8.5(b). The $d_{x^2-y^2}$ band moves towards the lower BE and the other two, d_{xy} and $d_{yz/xz}$ bands move towards the higher BE at the Γ point. The same band moves in opposite direction in case of FeTe by the application of U = 3.5 eV. On the other hand, the separation between the two electron like bands at the M point is enhanced in FeTe unlike the FeSe case where both the electron like bands are quasidegenerate and shift towards the lower BE under the influence of U = 4.0 eV.

Evolution of the near Fermi bands in FeSe and FeTe, with the tuning of J, are shown in panel (a) and (b) respectively of Fig. 8.6. In FeSe, at the Γ point, the $d_{x^2-y^2}$ band which was crossing the E_f comes down below the E_f and the $d_{yz/xz}$ band which was not crossing E_f, crosses E_f after applying J = 0.1 eV. Similarly, the degeneracy of the two electron like bands at M point is also lifted. In FeTe, a gradual shifting is observed in the hole like $d_{x^2-y^2}$ band at the Γ point towards the E_f and a gradual decrease in the separation between the two electron like bands at the M point under the influence of Hund's coupling.

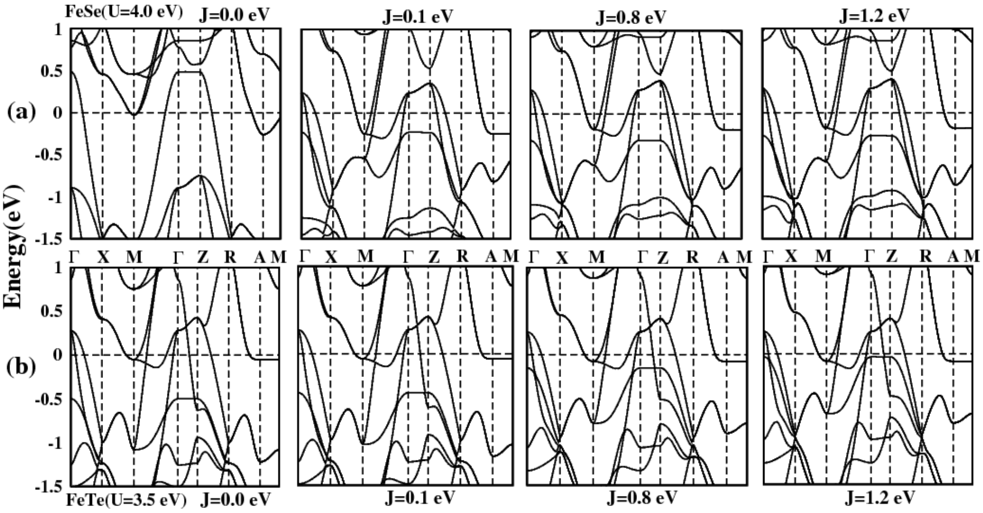

Figure 8.6: Panel (a) and (b) shows band structure plot for FeSe and FeTe at different values of J = 0.0, 0.1, 0.8 and 1.2 eV from left to right. The value of U is set to 4.0 and 3.5 eV respectively in all FeSe and FeTe plots.

In a recent ARPES report on FeSe the two hole like bands have been observed around the Γ point and the two bands, one electron like and the other hole like, at the M point from 40 meV below E_f [37]. Another ARPES study on $FeTe_{1-x}Se_x$ for x = 0, 0.2, 0.3, 0.4 and 0.45 compounds by Ieki*et al.* [14] reported three clear hole like bands at the Γ point (α, $\alpha^{'}$ and β) which evolve with Se doping and a shallow electron pocket at the M point for x = 0.45. The $\alpha^{'}$ and β crosses the E_f whereas the α is around 20 meV below E_f. Similar results have also been experimentally observed in $Fe_{1.04}Te_{0.66}Se_{0.34}$ [16], $FeSe_{0.42}Te_{0.58}$ [17], $Fe_{1.03}Te_{0.7}Se_{0.3}$ [38] and $FeTe_{0.55}Se_{0.45}$ [39]. However, in $Fe_{1.02}Te$ [40] and $Fe_{1-x}Te/Se$ [15] only two hole like bands are observed at the Γ point. The band renormalization factor also varies highly at different points of the Brillouin zone.

For example, in case of $FeSe_{0.42}Te_{0.58}$ Tamai *et al.* [17] observed *m*/m* = 20 for electron like band at the M point whereas it is just 6 for one of the hole like band at the Γ point. It is clear from Fig. 8.5(a) and (c) that initially when *U* and *J* are not incorporated all the three hole like bands cross the E_f in both the compounds and the electron like band is placed at higher BE (- 0.29 eV) in FeSe and (- 0.23 and - 0.47 eV) in FeTe at the M point. Only when correlation effect is included, one of the hole like band comes down below the E_f and other two cross the E_f. Further, the electron like band approaches towards E_f as is clear from Fig. 8.6 where in case of FeTe at *U* = 3.5 and *J* = 0.8 eV, the innermost hole like band appear at 0.18 eV below the E_f at the Γ point and the electron like band moves closer to E_f by 0.1 eV. This trend qualitatively matches with the above mentioned experimental findings, although the magnitudes of shifts are different. The orbital character of these near E_f bands, revealed by photoemission studies using polarized light [16, 39], also agree with our results. These results signify the importance of electronic correlation in these compounds.

From the transfer integral values, calculated by Miyake *et al.* for FeSe and FeTe [34], it is clear that this value is large between d_{xy} and its nearest neighbour (nn) $d_{3z^2-r^2}$ orbital. It builds a strong interorbital hybridization between d_{xy} and $d_{3z^2-r^2}$ orbitals which leads to a localization of the $d_{3z^2-r^2}$ states at higher BE with a clear gap from E_f. The d_{xy} orbitals, which point towards the nn Fe site has the largest band width and show two well separated peaks, one in the valence band and the other in the conduction band. On the other hand, transfer integrals between d_{xy} and nn $d_{x^2-y^2}$ orbitals are small but for the second nn they depend on the height of anion. They are large in case of FeSe in comparison to FeTe. Thus the chalcogen-p enhance the interorbital hybridization between the d_{xy} and its second nn $d_{x^2-y^2}$ orbitals which is reflected as a prominent pseudogap structure in the $d_{x^2-y^2}$ states in FeSe. Moreover, the interorbital hybridization between d_{xy} and second nn $d_{yz/xz}$ orbital is also mediated via the anion-p orbital. Hence it is also large in case of FeSe and contribute to the pseudogap feature. On the contrary, larger height of Te anion allows a finite value of transfer integrals between the $d_{yz/xz}$ with the nn $d_{3z^2-r^2}$ and $d_{x^2-y^2}$ orbitals by breaking the mirror plane symmetry in case of FeTe. These inter orbital hybridizations are responsible for the gap in the $d_{yz/xz}$ states at - 0.8 eV, which is absent in FeSe (Fig. 8.4). When the Coulomb interaction is introduced, it reduces the interorbital hopping and mainly the $d_{yz/xz}$ and $d_{x^2-y^2}$ states are affected which have large number of states near the E_f. As a consequence of this, electrons are transferred from the in-plane $d_{x^2-y^2}$ and d_{xy} to the out of plane $d_{yz/xz}$ and $d_{3z^2-r^2}$ orbitals and get localized at higher BE in case of FeSe. In FeTe, the transfer occurs from d_{xy} and $d_{yz/xz}$ to $d_{x^2-y^2}$ orbitals as is clear from Figs. 8.2 and 8.4. On the other hand, the application of *J* blocks the fluctuations in the occupancy of different Fe-3d orbitals which is clearly seen from the occupation table where a small value of *J* = 0.1 eV redistribute the electrons among different d-orbitals. Such orbital selective effects (increase in the occupation of d$_{xy}$ and d$_{x^2-y^2}$) are clearly seen under the influence of Hund's coupling. Since the value of α deviates substantially from the ideal tetrahedron value, unlike in the FeSe, the crystal field splitting is large in FeTe [41]. It increases the energy difference between the d$_{x^2-y^2}$ with the d$_{yz/xz}$ and d$_{xy}$ orbitals. So Hund's coupling promotes a gradual transfer of electrons from the highly occupied d$_{x^2-y^2}$ (at J = 0.0 eV) to the d$_{xz/yz}$ and d$_{xy}$ orbitals with an increase of J contrary to FeSe, where a small value of J is sufficient to transfer the electrons among these orbitals in order to reduce their Coulomb repulsion energy. Thus the different strengths of interorbital hybridization and the crystal field splitting, which are mainly governed by the anion height, change the occupancy of electrons and band structure of individual Fe-3d orbital. Hund's coupling promotes this differentiation and act like a band decoupler which was previously studied by Medici *et al.* [42, 43]. This could be the origin of the orbital selective correlation effects seen in iron chalcogenide compounds.

8.4 Conclusion

We presented a comprehensive investigation of the effect of Coulomb interaction and Hund's coupling in the Fe-3d states in FeSe and FeTe. In both the compounds states around E$_f$ originate predominantly from Fe-3d orbitals having a pseudogap feature just above the E$_f$. The hybridized states between Fe-3d and chalcogen-p orbitals which lie at higher BE, depend heavily on the chalcogen height from the Fe plane and are weak in case of FeTe where the height of Te anion is higher in comparison to Se in FeSe. The Coulomb interaction localizes and shifts the Fe-3d states towards higher BE energy in both the compounds, however this interaction is strongly screened by the Te-p bands in FeTe. It is observed that this effect is significant in d$_{yz/xz}$ and d$_{x^2-y^2}$ states in case of FeSe. Electrons in these localized states again become itinerant under the influence of J and distinct orbital selective changes are seen in the electronic structure. Similar to U, Hund's coupling effect is also prominent in FeSe in comparison to FeTe. The orbital selective nature of the correlation effect is linked to the different values of the interorbital hybridization among different Fe-3d orbitals which are mediated via the chalcogen-p orbitals. The strength of these interorbital hybridization is governed mainly by the geometry of anion tetrahedra, the height of anion from the Fe plane (z) and the anion-Fe-anion angle α. The difference in the anion tetrahedra geometry results in different orbital selective behaviors of the correlation effect in both the compounds. Our results also show that, the electron pocket at the M point of the Brillouin zone and nature of the pseudogap at E$_f$ are also linked to the anion height dependent correlation effects in the family of Fe superconductors.

Bibliography

[1] Wang, Q. Y. , *Chin. Phys. Lett.*, **29**, (2012), 037402.

[2] J. J. Lee, F. T. Schmitt, R. G. Moore, S. Johnston, Y.-T. Chi, W Li, M. Yi, Z. K. Liu, M. Hashimoto, Y. Zhang, D. H. Lu, T. P. Devereaux, D. -H. Lee and Z.-X Shen, *arXiv:1312.2633V5*

[3] Xu Liu, Def Liu, W. Zhang, J. He, L. Zhao, S. He, D. Mou, F. Li *et al.*, *arXiv:1402.1400v1*

[4] F.C.Hsu, J.-Y.Luo,K. W.Yeh, T. K. Chen, T. W. Hung, P. M. Wu, Y. C. Lee, Y. L. Huang, Y. Y. Chu, D. C. Yan and M. K. Wu, *Natl. Acad. Sci. U.S.A.*, **105**, (2008), 14262.

[5] S. Margadonna, Y. Takabayashi, Y. Ohishi, Y. Mizuguchi, Y. Takano, T. Kagayama, T. Nakagawa, M. Takata, and K. Prassides, *Phys. Rev. B*, **80**, (2009), 064506.

[6] S. Li, C. De la Cruz, Q. Huang, Y. Chen, J. W. Lynn, J. Hu, Yi-Lin Huang, Fong-Chi Hsu, Kuo-Wei Yeh, Maw-Kuen Wu and P. Dai, *Phys. Rev. B* , **79**, (2009), 054503.

[7] Yeh K -W, Huang T -W, Huang Y L, Chen T -K, Hsu F -C, Wu P M, Lee Y - Y, Chu Y -Y, Chen C -L, Luo J -Y, Yan D -C and Wu M -K, *Europhys. Lett.*, **84**, (2008), 37002.

[8] Z. Xu, J. Wen, G. Xu, Q. Jie, Z. Lin, Q. Li, S. Chi, D. K. Singh, G. Gu, and J. M. Tranquada, *Phys. Rev. B* , **82**, (2010), 104525.

[9] M. Bendele, P. Babkevich, S. Katrych, S. N. Gavasaliya, E. Pomjakushina, K. Conder, B. Roessli, A. T. Boothroyd, R. Khasanov and H. Keller, *Phys. Rev. B* , **82**, (2010), 212504.

[10] R. Viennois, E. Giannini, D. van der Marel, R. cerny, *J. Solid State Chemistry*, **183**, (2010), 769.

[11] E. Z. Kuchinskii, I. A. Nekrasov, M. V. Sadovskii, *arXiv:1004.0801v1*, (2010)

[12] Y. Mizugucgi, Y. Hara, K. Deguchi, S. Tsuda, T. Yamaguchi, K. Takeda, H. Kotegawa, H. Tou and Y Takano, *Supercond. Sci. Technol.*,**23**, (2010), 054013.

[13] C.Y. Moon, H. J. Choi, *Phys. Rev. Lett.* , **104**, (2010), 057003.

[14] E. Ieki, K. Nakayama, Y. Miyata, T. Sato, H. Miao, N. Xu, X. -P. Wang, P. Zhang, T. Qian, P. Richard, Z. -J. Xu, J. S. Wen, G. D. Gu, H. Q. Luo, H. -H. Wen, H. Ding and T. Takahashi, *Phys. Rev. B* , **89**, (2014), 140506(R).

[15] Y. Xia, D. Qian, L. Wray, D. Hsieh, G.F. Chen, J.L. Luo, N.L. Wang and M.Z. Hasan, *Phys. Rev. Lett.*, **103**, (2009), 037002.

[16] Fei Chen, Bo Zhou, Yan Zhang, Jia Wei Ou, Jia-Feng Zhao, Cheng He, Qing-Qin Ge, Masashi Arita, Kenya Shimada, Hirofumi Namatame, Masaki Taniguchi, Zhong-Yi Lu, Jiangping Hu, Xiao-Yu Cui and D.L. Feng, *Phys. Rev. B* , **81**, (2010), 014526.

[17] A. Tamai, A.Y. Ganin, E. Rozbicki, J. Bacsa, W. Meevasana, P.D.C. King, M. Caffio, R. Schaub, S. Margadonna, K. Prassides, M.J. Rosseinsky and F. Baumberger, *Phys. Rev. Lett.* , **104**, (2010), 097002.

[18] P. Mishra, H. Lohani, R. A. Zargar, V. P. S. Awana and B. R. Sekhar, *J. Phys. Condens Matter*, **26**, (2014), 425501.

[19] R. Yoshida, T. Wakita, H. Okazaki, Y. Mizuguchi, S. Tsuda, Y. Takano, H. Takeya, K. Hirata, T. Muro, M. Okawa, K. Ishizaka, S. Shin, H. Harima, M. Hirai, Y. Muraoka, and T. Yokoya, *J. Phys. Soc. Jpn.*, **78**, (2009), 034708.

[20] A. Yamaasaki, Y. Matsui, S.Imada, K. Takase, H. Azuma, T. Muro, Y.Kato, A.Higashiya, A.Sekiyama, S. Suga, M. Yabashi, K.Tamasaku, T. Ishikawa, K. Terashima, H. Kobori, A. Sugimura, N. Umeyama, H. Sato, Y. Hara, N. Miyagawa and S.I. Ikeda, *Phys. Rev. B* , **82**, (2010), 184511.

[21] Markus Aichhorn, Silke Biermann, Takashi Miyake, Antoine Georges and Masatoshi Imada, *Phys. Rev. B*, **82**, (2010), 064504.

[22] Ansgar Liebsch, *Phys. Rev. B* , **84**, (2011), 180505(R).

[23] L. Craco and S. Leoni, *Eur. Phy. Lett.* , **92**, (2010), 67003.

[24] U. von Barth and L. Hedin, J. Phys. C, **4**, (1971), 2064.

[25] O.K.Andersen, *Phys. Rev. B*, **12**, (1975), 3060.

[26] O.K.Andersen and O.Jepsen, *Phys. Rev. Lett.*, **53**, (1984), 2571.

[27] R. W. Tank, O. Jepsen, A. Burkhardt and O. K. Andersen, *The Stuttgart TB-LMTO-ASA programe*, **Version 47**.

[28] Kazumasa Horigane, Haruhiro Hiraka and Kenji Ohoyama, *J. Phys. Soc. Jpn.*, **78**, (2009), 074718.

[29] Zargar R A, Pal A, Haz A K, Awana V P S, *J. Supercond. Nov. Magn.*, **27**, (2014), 897.

[30] Vladimir Anisimov, F. Aryasetiwan and A. I. Lichtenstein, *J. Phys. Condens Matter* , **9**, (1997), 767.

[31] Giannozzi P *et. al.* , http://www.quantum-espresso.org.

[32] Alaska Subedi, Lijun Zhang, D.J. Singh and M.H. Du, *Phys. Rev. B*, **78**, (2008), 134514.

[33] G. R. Grechnev, A. S. Panfilov, A. V. Fedorchenko, V.A. Desnenko, I.P. Zhuravleva, S.L. Gnatchenko, D.A. Chareev, O.S. Volkov, A.N. Vasiliev, *Ukr. J. Phys.*, **57**, (2012), 171.

[34] Takashi Miyake, Kazuma Nakamura, Ryotaro Arita and Masatoshi Imada, *J. Phys. Soc. Jpn.*, **79**, (2010), 044705.

[35] Antoine Georges, Luca De' Medici and Jernej Mravlje, *arXiv:1207.3033v2*, (2012).

[36] K Haule and G Kotliar, *New Journal of Physics* , **11**, (2009), 025021.

[37] K. Nakayama, Y. Miyata, G. N. Phan, T Sato, Y. Tanabe, T. Urata, K. Tanigaki and T. Takahashi, *arXiv:1004.0857v1*, (2014).

[38] K. Nakayama, T. Sato, P. Richard, T. Kawahara, Y. Sekiba, T. Qian, G. F. Chen, J. L. Luo, N. L. Wang, H.Ding, and T. Takahashi, *Phys. Rev. Lett.* , **105**, (2010), 197001.

[39] H. Miao, P. Richard, Y. Tanaka, K. Nakayama, T. Qian, K. Umezawa, T. Sato, Y.-M. Xu, Y. B. Shi, N. Xu, X.-P. Wang, P. Zhang, H.-B. Yang, Z.-J. Xu, J. S. Wen, G.-D. Gu, X. Dai, J.-P. Hu, T. Takahashi and H. Ding, *Phys. Rev. B* , **85**, (2012), 094506.

[40] Z. K. Liu, R.-H He, D.H. Lu, M. Yi, Y. L. Chen, M. Hashimoto, R. G. Moore, S.-K. Mo, E. A. Nowadnick, J. Hu, T. J. Liu, Z. Q. Mao, T. P. Devereaux, Z. Hussain and Z.-X. Shen, *Phys. Rev. Lett.* , **110**, (2013), 037003.

[41] Z. P. Yin, K. Haule and G. Kotliar, *Nature Materials Letters*, **10**, (2011), 932.

[42] Luca de' Medici, *Phys. Rev. B* , **83**, (2011), 205112.

[43] Nicola Lanata, Hugo U. R. Strand, Gianluca Giovannetti, Bo Hellsing, Luca de' Medici and Massimo Capone, *Phys. Rev. B* , **87**, (2013), 045122.

Chapter 9

Summary

In the present thesis, we have studied the electronic structure of some of the Bi based topological insulators (TIs) and Pd, Fe based new superconductors (SCs) in detail using photoemission spectroscopy in conjugation with first principles calculations. The summary of each chapter is as follows

Chapter-1 provides an overview of the field of TIs and SCs. It also describes some of the essential properties of Bi based family of TIs and superconducting compounds, BiPd, Pd ternary chalcogenides and FeSe(Te).

Chapter-2 presents a brief introduction to the fundamentals of photoelectron spectroscopy. A detailed account of the working principles and instrumentation of the photoemission setup, which I utilized to accomplish this thesis work, have also been given in this chapter.

Chapter-3 gives an introduction to the density functional theory (DFT). The first principles methods of electronic band structure calculations under the framework of DFT formulation using TBLMTO and plain wave basis schemes have also been discussed in this chapter.

Chapter-4 covers our comparative ARPES study on topological insulators Bi_2Se_3 and BiSe. We observed Dirac like linearly dispersive surface state bands (SSBs) in the energy gap region of Bi_2Se_3. Band bending (BB) makes these bands drift towards the higher binding energy (BE) as a function of time after the cleaving. On the other hand, the SSBs in BiSe resemble Rashba split states which could be originating from the coupling between terminated Bi bilayer and adjacent quintuple layer. This difference in the observed SSB in BiSe and Bi_2Se_3, despite the fact that both the compounds have same elemental composition highlights the importance of structural geometry in deciding the topological properties in Bi based binary compounds.

Our comprehensive ARPES and DFT study on quaternary alloy topological insulator $BiSbTe_{1.25}Se_{1.75}$ is presented in **Chapter-5**. Signals of non-trivial topology of the SSBs and a strong warping of the Fermi surface (FS) are clearly observed in the ARPES data. We also found pronounced effects of aging due to BB and it is relatively stronger in this compound compared to the TI Bi_2Se_3. This difference could be originating from the distinct screening of the surface charges arising from the change in composition of the quintuple layers of the two compounds. Further experiments reveal that the nature of BB effects is highly sensitive to the exposure to various gas species. Our study demonstrates that the presence of different pnictogen (Bi,Sb) and chalcogen (Se,Te) atoms modifies the topological properties of the quaternary TI $BiSbTe_{1.25}Se_{1.75}$ in comparison to the binary TI Bi_2Se_3.

Chapter-6 deals with the electronic structure study of BiPd which is considered to be a TI as well as non-centrosymmetric SC. In our ARPES measurements we observe a high electronic distribution on the FS of this compound resulting from various electron and hole like bands which are present in the vicinity of the Fermi energy (E_f). Our first principles calculations show that the near E_f states are primarily composed of Bi-6p with a little admixture of Pd-$4d_{x^2-y^2/zy}$ orbitals. There are various spin-orbit split bands involved in the crossing of E_f making a complex FS. The FS mainly consists of multi sheets of three dimensions which disfavor the nesting between different sheets of the FS and thereby inhibit various density wave instabilities in this system. Our study elucidates that BiPd could be a s-wave multiband superconductor.

Chapter-7 extends the study of electronic structure of SCs by presenting our angle integrated photoemisson spectroscopy investigations on the recently discovered Pd ternary chalcogenides in conjugation with DFT based calculations. We observe that the valence band (VB) spectra of $Nb_2Pd_{0.95}S_5$, $Nb_2Pd_{1.2}Se_5$, and $Ta_2Pd_{0.97}S_6$ are qualitatively similar except for some slight differences in the energy position of various features. On the other hand, the VB spectra of $Ta_2Pd_{0.97}Te_6$ is remarkably different, particularly in the near E_f region where a clear metallic edge is observed, unlike the other compounds. Our study also shows the existence of a temperature dependent pseudogap in $Nb_2Pd_{0.95}S_5$ while the near E_f states remain unchanged with the lowering of temperature to 77K in the other compounds. In our calculated DOS, states crossing the E_f are dominated by different Pd-4d and Nb-4d orbitals ensuring significant role of multiband effects in $Nb_2Pd_{1.2}Se_5$ and $Nb_2Pd_{0.95}S_5$ compounds. Our study provides a deeper insight into the VB states of these Pd based ternary compounds and their correlation with their different structural geometry.

Chapter-8 further deals with the SCs where we present a comparative study of the influence of Coulomb interaction and Hund's coupling on the electronic structure of FeSe and FeTe using LDA + U method. We found the correlation effects are orbital selective due to the strength of interorbital hybridization among the different Fe-3d orbitals mediated via the chalcogen (Se/Te-p) orbitals and are different in both the compounds. The Coulomb interaction is screened significantly by Te-p bands in FeTe. Similarly the orbital selection is different in both the compounds because of the difference in the chalcogen height.